

Dynamics of Matter-Wave Quantum Emitters in Engineered Reservoirs

A Dissertation Presented

by

Michael Stewart

to

The Graduate School

in Partial Fulfillment of the Requirements

for the Degree of

Doctor of Philosophy

in

Physics

Stony Brook University

August 2020

Stony Brook University

The Graduate School

Michael Stewart

We, the dissertation committee for the above candidate for the Doctor of Philosophy degree, hereby recommend acceptance of this dissertation.

Dominik A. Schneble – Dissertation Advisor
Professor, Department of Physics and Astronomy

Thomas Weinacht – Chairperson of Defense
Professor, Department of Physics and Astronomy

Tzu-Chieh Wei
Associate Professor, Department of Physics and Astronomy

Ana Asenjo-Garcia
Assistant Professor, Department of Physics
Columbia University

This dissertation is accepted by the Graduate School.

Eric Wertheimer
Dean of the Graduate School

Abstract of the Dissertation

**Dynamics of Matter-Wave Quantum Emitters
in Engineered Reservoirs**

by

Michael Stewart

Doctor of Philosophy

in

Physics

Stony Brook University

2020

Bose-Einstein Condensates (BECs) confined in optical lattices provide a rich playground for studying the physics of complicated quantum systems in an exquisitely well controlled manner. In this dissertation, we experimentally study an array of matter-wave emitters realized with ultracold ^{87}Rb atoms confined in an array of one-dimensional tubes, and we report for the first time on emission experiments into a band structure. By varying the bandwidth, we are able to demonstrate a transition from (mostly) Markovian behavior to the limit of a pure Rabi-oscillation, as in cavity quantum-electrodynamics, and we also characterize the structure of *two* bound states, above and below the band, whose spatial shape is strongly modified by the underlying lattice band structure.

We develop a theoretical model for the quantitative understanding of these and earlier results on emission from an isolated emitter into free space. The modeling treats the emitter as a simple open-quantum-system in which the harmonic oscillator ground state of a deep well of a state-selective optical lattice potential is coupled to

a gapped continuum of momentum states. We solve this model by directly integrating the Schrödinger equation using Laplace transforms and the tools of complex analysis, and we make predictions for deviations from Weisskopf-Wigner type Markovian decay for experimentally realistic parameter regimes, most notably, for the case where the emitter energy is small or else negative. We connect these decay behaviors to the existence of bound states, in which the emitted matter-waves are unable to fully escape the originating emitter. The number and character of these bound states, as well as their effect on the observable dynamics is explored for the case of a free-particle dispersion with a single energetic edge, as well as for a sinusoidal dispersion with two energetic edges.

Our results show that a matter-wave emission platform can provide insight into the physics of photonic band-gap materials, currently a burgeoning research topic in quantum information science. We also propose experiments leveraging our emitter system to study effective Hamiltonian engineering within a dissipative quantum system.

Contents

List of Figures	vii
Acknowledgements	viii
1 Introduction	1
2 Overview of the experimental platform	5
2.1 Implementing a quantum emitter for matter-waves	5
2.2 Implementing reservoirs for emitted matter waves	6
2.3 Coupling quantum emitters to the reservoir	7
2.4 Outline of the remainder of this thesis	8
3 Introduction to the theory of Open Quantum Systems	10
3.1 Time reversibility and unitarity: an invitation	10
3.2 System plus reservoir models	12
3.3 The Weisskopf-Wigner model	14
4 Atomic spontaneous emission into structured reservoirs	19
4.1 Emission near a band gap	19
4.2 Matter-wave emission: overview	20
4.3 Emission near a single energetic edge	21
4.3.1 Introduction to the 1D model	21
4.3.2 Population dynamics	24
4.3.3 Markovian limit	29
4.3.4 Momentum distribution of the emitted matter-waves .	32
4.3.5 Matter-wave bound states	34
4.4 Emission near a band with two edges	40
4.4.1 Solution for emission into a 1D band	41
4.4.2 Bound state oscillations	46
4.4.3 Deep lattice limit	48
4.4.4 Weak-lattice limit	51

4.4.5	Bound states above and below the band	52
4.5	Concluding remarks	55
5	Experiments on spontaneous emission of matter waves into a tunable band structure	56
5.1	Experimental tools and techniques	56
5.1.1	Condensate production in brief	56
5.1.2	Atom Imaging Scheme	58
5.1.3	State-selective Optical Potentials	59
5.1.4	Microwave hyperfine transitions	61
5.1.5	Sample preparation	62
5.1.6	Determining the resonance condition	63
5.2	Experiments on free-particle emission	63
5.2.1	Spontaneous Emission near a Single Edge	63
5.2.2	Matter-Wave Emitter Bound State	66
5.3	Experiments on emission into a band structure	68
5.3.1	Band Spectroscopy	68
5.3.2	Time Dynamics for Emission into a Band	72
5.3.3	Bound States Above and Below the Band	74
6	Theoretical considerations for bound-state induced many-body physics in optical lattices	76
6.1	Master equations	77
6.2	Modified superfluid to Mott-insulator transition	80
6.2.1	Standard superfluid Mott-insulator transition	80
6.2.2	The SF-MI transition with long-range tunneling	84
7	Conclusion	92
	Bibliography	94

List of Figures

2.1	Schematic of quantum emitter platform	7
2.2	Experimental coupling scheme	8
4.1	Atomic spontaneous emission model schematic	22
4.2	Single edge excited state population	28
4.3	Emitted momentum spetral properties	33
4.4	Bound state properties near a single edge	39
4.5	Emission into a band structure	42
4.6	Characteristic Band Emission Behaviors	47
4.7	Markovian Decay to Oscillation Transition	48
4.8	Bound state oscillation amplitude and frequency vs. J	49
4.9	Computed band bound state profiles	54
5.1	Science cell with lattice and imaging optics	57
5.2	Absorption imaging of a BEC	59
5.3	State selective optical potentials for ^{87}Rb	60
5.4	Free-emission parabola comparison	65
5.5	Excited state population dynamics in three regimes	66
5.6	Single-edge bound states	67
5.7	Band structure and emission spectrum for $s_b > 0$	69
5.8	Emission spectrum for $s_b < 0$	70
5.9	Ground band emission spectrum detail	72
5.10	Emission dynamics into a single band	73
5.11	Bound states above and below the band	75
6.1	Bose-Hubbard model schematic	81
6.2	Phase diagram of the Mott-Insulator to Superfluid transition .	85
6.3	Effective Hamiltonian phase diagram	89
6.4	Purifying a Mott Insulator by emission	90

Acknowledgements

What may in hindsight surprise nobody is that I'm finding this section to be the hardest to write in my whole thesis, and that's because I have so many people to whom I'd like to dedicate this work. It is unlikely for me to be sparing with my word count in any endeavor, let alone thanking everyone who helped to make this thesis possible, but I will do my best.

I wish to first thank my advisor, Dominik Schneble, whose mentorship and guidance have proven invaluable in my development as a researcher. From the outset, Dominik has afforded me the freedom to explore and grow as an experimental atomic physicist in ways that made sense to me and at the same time never made me feel like my theoretical penchant needed to be set aside. In addition to providing incredible clarity on a vast range of atomic physics and ultracold atom concepts and techniques (not to mention a style of performing pen-and-paper calculations which I use to this day), I can always count on Dominik to be present in the lab, keeping me on track, and eager to discuss results, even before they've been fully acquired. As much as I joke about being a lapsed theorist, I couldn't be happier that Dominik chose to take a chance on this would-be theorist and helped me to grow into a talented experimentalist with a theoretical heart.

Throughout my many years at Stony Brook, I've had the pleasure of working with and befriending some incredible individuals in the lab. I truly could not have gotten to the point of writing this thesis without Ludwig Krinner. The wealth of knowledge he has about all things optics, technology, and physics more than once saved me when learning to run experiments on my own, and that's not to mention the Sachertortes and Schwarzwälder Kirschtortes we got up to baking outside of the lab. Jeremy Reeves took me under his wing and helped me to find stable footing when I started, and his incredible, deadpan humor was a pleasure to work with. I am indebted to Arturo Pazmiño for technical support. There's nobody I can think of more skilled at electronics, and my experiments wouldn't have been possible without his tireless efforts. Joonhyuk Kwon has been a steadfast companion and an indispensable source of optimism, through broken lasers and triumphant data acquisitions alike.

I'm very excited to see how his work builds on my experiments and expands the playbook of what is possible with matter-wave quantum emitters. I would be remiss not to thank Alfonso Lanuza for his incredible ability to both carry out detailed theoretical calculations and to distill their essence into understandable intuition, and Youngshin Kim, though he recently joined the group, because he has already revolutionized our data analysis procedures. I am going to miss attending conferences with you all, and I hope you'll pour one out for me after you give incredible talks highlighting your awesome work!

I want to thank my Ph.D. defense committee for working with me to complete my degree in a historical fashion, being the first fully remote defense in the Department of Physics and Astronomy at Stony Brook due to Covid-19. Each of Thomas Weinacht, Tzu-Chieh Wei, and Ana Asenjo-Garcia have my thanks for attending my defense and for their careful reading and thoughtful comments on the text of my thesis. I have had the pleasure of working closely with Tom on the Quality of Life Committee for about as long as I've been at Stony Brook, and it pains me to say that there's not a chance anymore that I emcee for the holiday party. I hope that this thesis helps settle the long-standing debate between Tom and Dominik about how to understand atomic spontaneous emission. In addition to my committee, I must thank Martin Cohen and Hal Metcalf for all of the informal mentorship I've been privileged to receive over the years. Marty especially has been a gracious and patient reader of many a paper draft, and his knowledge of all things optics has been essential to my experimental success.

Outside of my own research group, I have to express my profound love and appreciation to the atomic physics community, especially Brian, Ian, Bertus, Mehdi, Yusong, Chuan, YiFan, XiaoYang, Samet, Guodong, and Sam. I could share anecdotes about what you each mean to me, but I only have limited space, so suffice it to say that each of you in your own way has made living and working in the basement a bit happier despite the chronic lack of sunlight. I wish you all success in your own futures.

Beyond the atomic physics crowd, I want to thank Lucie and Nick, some of my earliest friends at Stony Brook and long term roommates. There's a dinner party brewing, I just know it, and too many inside-jokes to count. I also would like to thank Fernando, Ben, Ashley, Melissa, Sheridan, Lupe, Batu, Mark, Adith, Emily, Jxhn, Michael, Alyssa, Melissa and Haylee, and Matt. We've made some good memories, and I'm eternally grateful to have met you.

My family has supported me throughout the years and shared in both the highs and lows of Ph.D. life. My parents, Lydia and John, have always been there to offer support when I needed a shoulder to cry on, as well as to join in my celebration when I achieved something I thought would be impossible.

Additionally John and Cara have helped me to succeed, with advice on job-hunting and motivational pictures of the family dog, Emmie. I couldn't be more grateful or proud of you as you start a new job and get your own doctorate in physical therapy. We made it.

Finally, I'd like to thank Himanshu from the bottom of my heart. You've been a rock, anchoring me in reality when I was liable to lose my head in the clouds, and you've made me laugh when I thought everything was hopeless. I'm truly a better person for knowing you, and I can't wait to see what the next chapter holds in New York City.

Chapter 1

Introduction

The seminal insight of Einstein in the field of statistical mechanics [1] is, arguably, that classical understanding of an ideal gas of particles breaks down when it is cooled below a certain temperature. Specifically, he showed, based upon the fully quantum calculation of Bose for the case of photons [2], that matter, in addition to light, has to be understood as having modified statistical properties at low temperature, and that for particles that we now call bosons (having integer spin), it is possible at sufficiently low temperatures to have a macroscopic occupation of a single quantum state [3]. This macroscopically occupied state is described by a single, coherent wave-function, but it can be thousands to millions of times larger than the typical atomic scale at which quantum mechanics dominates the behavior. This makes Bose-Einstein condensates (BECs) ideal systems for studying quantum physics in a laboratory setting.

Today, BECs [2–4] are routinely produced in the laboratory following the same procedures that led to the first condensates in dilute alkali-metal gases 25 years ago [5–8]. These ultracold (~ 100 nK) samples have become a cornerstone of Atomic, Molecular, and Optical (AMO) physics research (though by no means the only avenue of research in this vast and expanding field). While this thesis focuses on BECs, we also wish to note that fermions can be cooled to quantum degeneracy as well, resulting in degenerate Fermi gases (DFGs) [9–12], whose applications are just as varied and fascinating. In the intervening decades since the creation of the first laboratory BEC, research efforts have demonstrated their coherence properties, with applications to atom optics [13–18], wave-like physics of matter including sound [19, 20] and solitons [21, 22], and studies of superfluidity [23, 24]. Degenerate quantum gases of hydrogen and helium [25, 26], alkali metals (e.g. potassium [12, 27] and cesium [28]), and more recently transition metals (chromium [29]), alkaline-earth metals (calcium [30] and strontium [31, 32]), and lanthanides (ytterbium [33],

erbium [34], and dysprosium [35]) have been brought to quantum degeneracy as well.

Through suitable experimental techniques, the aspiring AMO physicist can control just about every relevant parameter of an ultracold gas. For example, utilizing Feshbach resonances [36, 37], the interaction strength between ultracold atoms can be tuned. With the advent of optical lattices [38, 39], it became possible to simulate condensed matter Hamiltonians, such as the Bose-Hubbard model [40] on a square lattice [41], and more recently, in hexagonal, tunable, or graphene like lattices [42–46], and even in quasicrystalline geometries [47, 48]. Fermions in optical lattices can realize the Fermi-Hubbard model and its attendant anti-ferromagnetism [49–53]. Promisingly, we can engineer effective Hamiltonian terms, e.g. via Raman laser pairs for spin-orbit coupling [54–56] or time-periodically modulated system parameters (realize Floquet engineering of effective Hamiltonian terms) allowing for studies of Haldane and Hofst  der models [45, 57, 58] and even relativistic physics [59] or long-range transport across a lattice [60]. Advances in optical technologies have allowed for the resolution of atoms on a single site of an optical lattice, for both bosons [61–63] and even fermions [64–67]. Disorder can be added to a quantum simulation using laser speckle [68] or atomic disorder [69]. Many important models of many-body physics have no known theoretical solution, but they can be directly accessed by quantum simulation [70–73]. Exotically, lattices in momentum space can be realized, offering, e.g., access to studies of self trapping [74] and topological Anderson insulators [75]. In addition to studies of single species, composite degenerate gases can be used to study exotic physics, for example bosons composed of fermions [76, 77] and ultracold polar molecules [78–80].

In order to focus the following discussion, we briefly introduce the notion of quantum simulation [81]. Quantum simulation (either digital or analog) is one of the four pillars of quantum information science, driving major research efforts. Quantum simulation [72] in its analog (or analogue) form is an umbrella term for using one quantum system that is easy to produce and tune with physical properties that are similar or identical to a quantum system of interest, to study a system which is more difficult to study in this way. Ultracold quantum gases are ideal platforms for performing quantum simulation because they are ultracold, which makes them correspondingly “ultra-slow” ($v_{typ} \sim \text{mm/s}$) and “ultra-large” ($r_{typ} \sim \mu\text{m}$), such that their dynamics can be easily observed.

The Schneble laboratory has a storied history of quantum simulation of everything from four-wave mixing of matter-waves [82], the superfluid to Mott-insulator transition in atomic species mixtures [83], disorder in the Bose glass

[69], the interplay of disorder and interactions on Bloch dynamics [84], and matter-wave diffraction from a matter wave crystal [85] and from a non-adiabatic “non-”potential [86]. Furthermore our lab is interested in using BECs to study the physics of open quantum systems, with previous works ranging from studies of a quantum to classical transition in a system of delta kicked rotors [87] to polaron physics [83] in hyperfine state mixtures. Research efforts on polaron physics have also led to attempts to study the spin-boson model [88–90], though so far, technical limitations have frustrated our attempts to realize it. Most recently, we have demonstrated a novel platform for the study of spontaneous emission of matter waves [91].

In order to understand how quantum systems, which are in principle time reversal symmetric, can undergo irreversible processes, a number of theoretical approaches to these open quantum systems have been developed [92, 93]. The central idea is that of a small quantum system coupled to a vast reservoir of quantum states into which information about the system is lost and over time never returns to the system. To be specific, a typical open quantum system consists of a small number of states, e.g. a two-level atom, coupled to (infinitely) many states, e.g. photons in free space, or the Bogoliubov modes in a BEC. If we consider an excited atom in free space, it is known that some time later, the atom will decay to its ground state and release a photon of some energy in some direction. This spontaneous emission serves as a toy open quantum system. The original treatment by Weisskopf and Wigner [94] in 1930 sought to explain the phenomenon using Dirac’s radiation theory [10]. It was realized later by Purcell that the density of available states can have a profound effect on the emission behavior [95]. At one extreme, we have cavity-QED [96] with only one available mode for emission, in which it would be impossible to speak of the single cavity mode as a “large” reservoir. The other extreme is the aforementioned Weisskopf-Wigner situation, in which the decay is completely controlled by the infinite reservoir of photon states. In between these two extremes is the regime of a bounded continuum of photon states. If these boundaries are realized as the edges of a band in one-dimension, the density of states diverges at these points, and any attempt to treat the system in a Markovian approximation is doomed to fail. Historically, consideration of this regime has been limited to photonic crystal materials [97–99] (also called photonic bandgap materials). It is this regime of singly and doubly bounded continua that we implement in a matter-wave context in this thesis. Here, the energetic edge(s) in the density of states leads to a much richer physics in this intermediate regime, including exotic decays and bound states. In particular, such systems provide an exciting platform for the engineering of strong photon-mediated interactions, both in the optical [100] and microwave [99] regimes.

These can result from the formation of atom-photon *bound states* [97] in which an excited atom is surrounded by an exponentially localized cloud of photonic excitations, which may extend over a long range.

While the field of waveguide-QED is broad (see [101–105]), we highlight specifically corrugated optical waveguides in one-dimension [106, 107], which have displayed superradiance and coherent dipole-dipole interactions [108, 109], as well as microwave guides using transmon qubits [110] which have also displayed coherent interactions between two atoms [111]. The reason that we highlight these one-dimensional systems is that we can realize a cold-atomic matter-wave analogue in the lab. First proposed in 2008 [112–114] as a candidate for the quantum simulation of the emission of photons near a photonic crystal, ultracold atoms in state-dependent optical lattices offer a complementary view of the physics of such systems. Since then, a flurry of theoretical research has predicted the behavior of spontaneous emission of matter waves in various geometries and dimensions [115–118] exhibiting strongly modified emission properties and bound states. On the experimental side, we recently developed a corresponding platform utilizing strongly confining 1D tubes with a state selective lattice along the third direction for the direct quantum simulation of photonic crystal physics [91, 114, 119]. Utilizing a microwave to enact an internal state change, we realize an array of initially excited emitters with tunable excited state energy and coupling strength, which we can use to explore in principle all regimes of the system, including those that are difficult to reach in a material sample, as well as gain access directly to complementary observables from the material case, such as the momentum of the emitted matter-wave radiation and the time dynamics of the excited state population.

Due to the somewhat technical nature of much of the work described in this thesis, we first introduce the experimental system in the following chapter. Equipped with a full understanding of the quantum emitter platform, we shall proceed to describe our experiments and the theoretical considerations which led to them.

Chapter 2

Overview of the experimental platform

In order to study the spontaneous emission of matter waves into structured reservoirs (emission vacua) of interest, we must bring together several ingredients. First, we need an emitter of matter waves and a tunable set of states that can be emitted into. Secondly, we require a coupling between the two states, and finally, we require experimental probes of the coupled emitter and emitted matter wave system. Our recent implementation [91], which forms the platform for the experiments discussed in this thesis, is largely based on a theoretical proposal of I. de Vega, et al. [112], though we shall point out where our implementation differs from that proposal.

2.1 Implementing a quantum emitter for matter-waves

In order to implement a system of quantum emitters for matter-waves, we start with a Bose-Einstein condensate (BEC) of rubidium-87 atoms in the $F = 1$, $m_F = -1$ hyperfine ground state (c.f. chapter 5 and [120].) At the heart of our experimental implementation is that we have access to and control over the entire ground state manifold of our rubidium BEC, and so we can choose one hyperfine state $|r\rangle = |F = 1, m_F = -1\rangle$ to be the excitation in the quantum emitter and another hyperfine state $|b\rangle = |F = 2, m_F = 0\rangle$ to be the emitted matter-wave state.

For the sake of our experiments, an $|r\rangle$ atom must be confined in position, and unable to access other states without an applied coupling. This turns out to be conveniently achieved by using an optical lattice potential. The simplest optical lattice is formed by the interference of two laser beams to

create a standing wave. By confining the BEC to a deep optical lattice, we localize the condensate atoms to the ground state wave-functions of the lattice wells. By making the lattice very deep, we suppress tunneling from one well to its neighbors, which is necessary for creating a state which, when suitably coupled, can serve as a quantum emitter for matter waves.

In our lab, we study one-dimensional physics, and we can achieve this through the use of more than one optical lattice. Using two very deep, horizontal optical lattices crossed at ninety degrees, we first create an array of isolated 1D tube potentials using $\lambda = 1064$ nm light. These tubes are isolated in the following sense: the timescale for particle in one tube to tunnel to a neighboring tube is much longer than the experimental timescales of interest, and so neighboring tubes do not play a role in the evolution of the system. We then apply a third optical lattice along the array of tubes, and thus we create an array of quantum emitters which emit into 1D. We control the properties of the array such that each emitter contains one or less $|r\rangle$ atom. This is achieved by first creating a Mott-insulating state and then “thinning it out”, c.f. chapter 5.

2.2 Implementing reservoirs for emitted matter waves

Having discussed how we create an array of quantum emitters in 1D, we now turn our attention to the second ingredient of our platform. As briefly mentioned before, we will use a different hyperfine ground state of rubidium-87, $|b\rangle = |F = 2, m_F = 0\rangle$, as our emitted matter wave state(s). Naively applying an optical lattice along the tubes for the $|r\rangle$ atoms will in principle also create a potential for the $|b\rangle$ atoms, since a typical optical lattice is created using far off resonant light, which affects all of the hyperfine states equally. The resolution to this problem is to take advantage of so-called state-dependent optical lattices (SDOLs), which are detailed in section 5.1.3. In brief, by choosing a laser wavelength between the strong D_1 and D_2 transition in rubidium [121], which for us will be $\lambda \approx 790$ nm, the optical potential can be chosen in such a way as to be small or else vanish outright for $|b\rangle$ atoms, while remaining deep for $|r\rangle$ atoms.

The shallow or vanishing SDOL potential along the tube for $|b\rangle$ atoms suggests the following interpretation of the quantum states in the tube: the available states are plane waves propagating to the left or right (along the axis of the tube, strictly speaking up and down), indexed by the (continuous) momentum of the emitted wave. If the SDOL is nonvanishing for the $|b\rangle$ atoms,

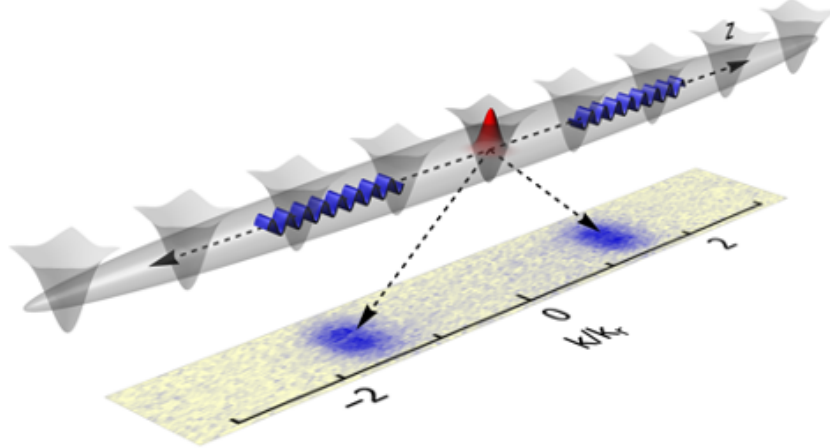


Figure 2.1: Cartoon illustrating our quantum emitter platform. The emitters (shown as individual gray potential wells) contain $|r\rangle$ atoms, and by a suitable coupling (described in section 2.3) can transition to the emitted matter-wave states $|b\rangle$, which are then free to propagate along the 1D tube. A typical experimental absorption image of the propagating atoms in time of flight is shown below the cartoon. Due to the left/right (up/down) symmetry of the situation, we observe two blobs of atoms in the image, corresponding to emission at $|k|/k_r$, as fixed by the emitter excited state energy.

we instead work with Bloch waves of definite quasimomentum.

2.3 Coupling quantum emitters to the reservoir

The primary difference between the theoretical proposal [112] and our experimental implementation is the manner in which we couple the emitters to the propagating states. Rather than using a pair of Raman lasers as in [112], we instead utilize microwaves to couple the states and allow for transitions between them. In particular, our two chosen hyperfine ground states in Rubidium-87 are separated by approximately 6.8 GHz, and by choosing the frequency of our microwave coupling, we can select the energy of $|r\rangle$ relative to $|b\rangle$, as illustrated in Fig. 2.2(B). The strength of the microwave coupling Ω is also a tunable parameter in the experiment. In combination with the SDOL potentials described above, we thus realize an array of quantum emitters with tunable excited state energy $\hbar\Delta$ coupled to freely propagating (or else Bloch wave) modes at tunable energy and tunable coupling strength Ω .

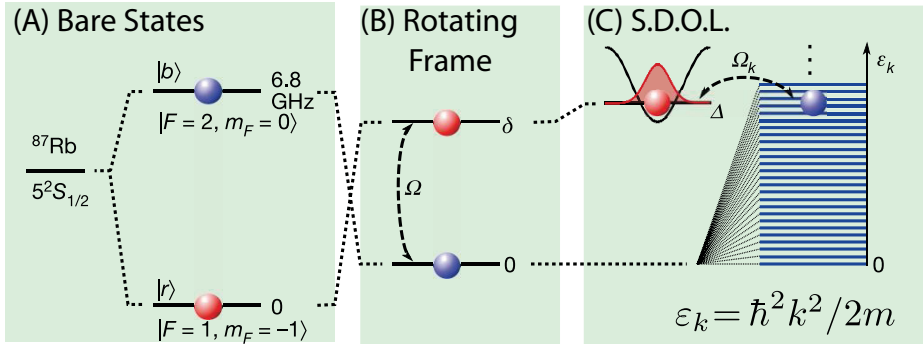


Figure 2.2: Experimental coupling scheme to realize a matter-wave quantum emitter. (A) The bare ground states $|r\rangle = |1, -1\rangle$ and $|b\rangle = |2, 0\rangle$ at 5 G magnetic field along z are chosen as the emitter and emitted states, respectively. (B) Microwave coupling $\omega_\mu \sim 6.8$ GHz, variable strength Ω is applied, and working in the rotating frame, $|r\rangle$ is detuned from $|b\rangle$ by an amount δ . (The fact that the bare $|r\rangle$ state is lower in energy than $|b\rangle$ makes no difference once the coupling is applied.) (C) Introduction of a state-dependent optical lattice (S.D.O.L.). The trapped $|r\rangle$ atoms are shifted upward in energy by $\omega_0/2$, which shifts δ to $\Delta = \delta + \omega_0/2$. $|b\rangle$ atoms are free to propagate along a 1D tube, thus resulting in a continuum of momentum states $|b_k\rangle$ having energy $\varepsilon_k \propto k^2$, coupled to with strength $\Omega_k = \Omega\gamma_k$, c.f. equation 4.13 due to the variable Franck-Condon overlap between the Wannier-state in $|r\rangle$ and the variable momentum state $|b_k\rangle$. Illustration adapted from Krinner, et al., Nature **559**, 589 (2018) [91].

Given these ingredients, all we require is an experimental probe of the system. To this end, our lab utilizes state selective absorption imaging in time of flight. For details of our imaging scheme, see section 5.1.2, but in brief, we let the atomic sample expand and fall, separate the hyperfine components, and then image their shadows on a CCD camera using resonant light.

2.4 Outline of the remainder of this thesis

Having described our experimental platform, we are faced with two questions: what can we do with our platform, and how can we understand what we do? The remainder of this thesis will attempt to answer these two questions. As for what we can do with our platform, chapter 5 will describe experiments on spectroscopy of our system, time dynamics including fractional decay of the emitter population, and the formation of bound states of quantum emitters

and matter waves, for both free particle and Bloch wave reservoirs. In order to understand our results, a detour through the basic theory of open quantum systems, chapter 3, and the specific model of atomic emission that we are interested in [112, 114, 122] is required, and we present our model and calculated effects in detail in chapter 4. While the experiments detailed in this thesis focus primarily on single-particle effects, our platform is well suited to studies of many-body effects, and we give an overview of some such effects in chapter 6, focusing especially on how the well-known superfluid to Mott-insulator transition is modified in our system. We end in chapter 7 with a summary of what we have done up to this point and an outlook towards future work in our lab.

Chapter 3

Introduction to the theory of Open Quantum Systems

3.1 Time reversibility and unitarity: an invitation

Quantum mechanics is well known to be governed by unitary time evolution, or equivalently, by the Schrödinger equation

$$i\hbar \frac{\partial}{\partial t} |\Psi\rangle = \hat{H} |\Psi\rangle \quad (3.1)$$

which has time-reversal as a symmetry. (We note here that we are assuming the absence of magnetic fields, which break the symmetry.) Mathematically [123], this means there exists an anti-unitary operator Θ which leaves the Hamiltonian invariant, $\Theta^{-1}\hat{H}\Theta = \hat{H}$. In short: the laws of physics look the same running forward in time as they do if time were to run backward. However, this contrasts with our everyday experience of the classical world, in which a ball rolling along a rough surface eventually comes to a stop, but without some sort of kick, a stopped ball never spontaneously starts rolling. Implicit in the preceding example is a notion of dissipation, in which some energy in the system is lost to an external environment from which it never returns. One might ask then whether there is a similar process at play in Quantum Mechanics, which after all is understood to describe the natural world on small scales.

It turns out that we have examples of quantum mechanical systems which exhibit dissipative behavior. Perhaps the most fundamental such example is that of spontaneous decay of (and emission of a photon from) an excited atom, which results in a ground state atom having lower energy and a photon prop-

agating away in some direction. To extend the analogy with the classical ball above a bit more, the ground state atom doesn't spontaneously become excited (except if it receives a “kick” by absorbing an appropriate photon that just so happens to pass by). However, in quantum mechanics such an irreversibility should in principle not be possible, because (3.1) is invariant under time reversal. The answer to this puzzle is the introduction of a (sub-)quantum system of interest (the initially excited atom, or else the same atom in its ground state), and an (infinitely-)large reservoir of quantum states (possible photon polarizations, energies, and propagation directions). The system plus reservoir as a whole is governed by reversible, unitary quantum mechanics, but if we do not look too closely at the reservoir, the (sub-)system of interest appears to undergo dissipative behavior as its initial excitation escapes into the reservoir.

As described in detail in [124], many systems are well described as open quantum systems. From diverse applications to quantum information and computing, quantum biology and chemical physics, applications of open quantum systems are varied and it behooves us to understand well how to describe them.

Generally speaking, solid-state physics is concerned with many models of open-quantum systems, especially when the coupling to the environment is weak. Brownian motion, the random motion of a particle in a background fluid, may also display non-Markovian effects, and theoretical and experimental efforts are ongoing for such systems ranging from quantum dots laser-coupled to reservoirs [88, 125] or nanomechanical oscillators coupled to BECs [126–128]. Furthermore, open quantum systems in solid state physics may also couple to fermionic (rather than bosonic) degrees of freedom, or even spin degrees of freedom [129–133]. Even in biological applications, quantum behaviors are seen to arise, and an open quantum system description is appropriate. Much effort studying coherences in photosynthetic complexes (molecules) has shown that these systems must be considered as quantum systems interacting with a phonon bath [134–137]. These phenomena are beyond the scope of this dissertation, but we note they are often treated using the same techniques as solid-state systems [138]. Chemistry as well contains examples of open-quantum-system behavior, where, for example in a large molecule, a system consists of a few bonds (or molecular modes) of interest, and the rest of the bonds serve as a reservoir.

In section 3.2, we will formalize the notions introduced in the preceding paragraphs. Then in section 3.3 we will present what is perhaps the most well known dissipative quantum system: the Weisskopf-Wigner model of spontaneous emission. The reader is strongly encouraged to spend time with the Weisskopf-Wigner model, as it serves as a leitmotif for the rest of this thesis.

3.2 System plus reservoir models

Much theoretical effort has been devoted to describing the dynamics of dissipative quantum systems [92, 93, 139, 140]. One promising approach to understanding dissipation in quantum mechanics is to divide the Hilbert space into two parts: a small system \mathcal{S} consisting of a few states of interest, and a large reservoir (or bath) \mathcal{R} consisting of (infinitely-)many degrees of freedom. The system and reservoir are assumed to be coupled due to an interaction. Furthermore, we will assume that the Hamiltonian of the system plus reservoir can be neatly decomposed as $\hat{H} = \hat{H}_S + \hat{H}_R + \hat{H}_I$, with \hat{H}_S and \hat{H}_R depending only on system (reservoir respectively) degrees of freedom, and \hat{H}_I contains all of the interactions between the two. Note that such a system \mathcal{S} is said to be an open quantum system (OQS) since its interaction with the large reservoir may introduce dissipation or decoherence.

The main idea, then, is to solve for the dynamics of the system of interest without needing to fully solve for or specify what happens in the reservoir. Specifically, if the density operator for the system plus reservoir model is $\hat{\rho}(t)$, our goal shall be to try to understand the dynamics of the *reduced density operator* $\hat{\rho}_S(t)$, which is obtained by tracing over the reservoir degrees of freedom, i.e.

$$\hat{\rho}_S(t) = \text{Tr}_R [\rho(t)] \quad (3.2)$$

The time evolution of this reduced density operator can then in principle be described by a formally exact quantum master equation:

$$\frac{d\hat{\rho}}{dt} = -i [\hat{H}, \hat{\rho}] + \mathcal{D}(\hat{\rho}) \quad (3.3)$$

explored in more detail in chapter 6. In practice, approximations are often made to assist in solving the full equations of motion, though this need not be the case.

Perhaps the most famous system plus bath model is the Caldeira-Leggett model [139], in which a system consisting of a particle of mass m moving in one dimension (coordinate x) is coupled to a bath of quantum harmonic oscillators via a linear interaction. In particular the system and reservoir Hamiltonians may be written

$$\hat{H}_S = \frac{\hat{p}^2}{2m} + \hat{V}(\hat{x}) \quad (3.4)$$

$$\hat{H}_R = \sum_{\alpha} \left[\frac{\hat{p}_{\alpha}^2}{2m_{\alpha}} + \frac{1}{2} m_{\alpha} \omega_{\alpha}^2 \hat{x}_{\alpha}^2 \right] \quad (3.5)$$

If the coupling to the environment is weak, then the interaction between the system and the bath can be assumed to be a linear function of the environment coordinates x_α , and thus the interaction Hamiltonian has the form

$$\hat{H}_I = - \sum_{\alpha} F_{\alpha}(\hat{x}) \hat{x}_{\alpha} + \Delta V(\hat{x}) \quad (3.6)$$

The second term in (3.6) is a counterterm which renormalizes the potential felt by the particle. Our goal here is not to study the Caldeira-Leggett model in general, however, we wish to note this model has found widespread application in the field of open quantum systems due to its generality. In fact, we shall show that the systems we consider have reservoir Hamiltonians of the form (3.5), and only slightly generalized system and interaction Hamiltonians.

The interaction Hamiltonian (3.6) couples states in the system of interest and the reservoir. As hinted at before, it leads to a quantum master equation (3.3) which describes the evolution of the density operator (i.e. populations and coherences) of the quantum system after having traced over the reservoir degrees of freedom. It can be shown generally [92, 124] that the commutator term is nothing more than the usual Heisenberg equation of motion under an effective Hamiltonian (having shifted energy levels), and thus represents unitary evolution. The second piece of the equation is called the *dissipator*, and it is this term which leads to a decrease of the population in the excited states of the quantum system, as well as their coherences, by capturing non-unitary “jumps” induced by the reservoir. In short, dissipation is accompanied by a shift of the energy levels, which we shall see generally applies to the systems we consider!

We stop here to take stock of what we have set out to do. By separating a composite quantum model into a system of interest and a reservoir with which it interacts, we can maintain full unitarity of the total quantum model (and thus time-reversal symmetry) while at the same time introducing apparent dissipation into the small system of interest. At this point, we could proceed by computing the (Markovian or non-Markovian) [124] master equation for the reduced density operator of the system, and in this way, learn about the dissipative dynamics of the model. (See chapter 6 for some details.) However, it is sometimes possible to obtain explicit analytic results for an open quantum system, and we turn our attention to one such model now.

3.3 The Weisskopf-Wigner model

We consider as our worked example of a system plus reservoir model in which irreversible decay arises in quantum mechanics the Weisskopf-Wigner model of spontaneous emission [94], which can be found in many textbooks (see, e.g. [141]). The system, solved using Dirac's radiation theory [10], in this case is an initially excited, two-level atom whose exited (ground) state we label as $|e\rangle$ ($|g\rangle$ respectively). We consider such an atom to be located at the origin of a three-dimensional space, and we assume further that the atom is coupled to an infinite continuum of propagating photon modes, characterized by a wave-vector \mathbf{k} and a polarization labeled by s . For completeness we note that the Hilbert space consists of those states having an excited atom and no photons present, $|e, 0\rangle$, and those containing a ground state atom and exactly one photon with specific wave-vector and polarization, $|g, 1_{\mathbf{k},s}\rangle$. The Hamiltonian of the system can be written

$$\hat{H}_{WW} = \hbar\omega_0 |e\rangle\langle e| + \sum_{\mathbf{k},s} \hbar\omega_{\mathbf{k}} (\hat{a}_{\mathbf{k},s}^\dagger \hat{a}_{\mathbf{k},s} + 1/2) + \hat{H}_I \quad (3.7)$$

where $\hbar\omega_0$ is the excited state energy of the atom, $\hbar\omega_{\mathbf{k}} = c|\mathbf{k}|$ is the energy of a photon with wave-vector \mathbf{k} , and $\hat{a}_{\mathbf{k},s}$ annihilates a photon having wave-vector \mathbf{k} and polarization s . As usual, its conjugate operator $\hat{a}_{\mathbf{k},s}^\dagger$ creates the corresponding photon, and the usual bosonic ladder operator algebra is satisfied, i.e. $[\hat{a}_{\mathbf{k},s}, \hat{a}_{\mathbf{k}',s'}^\dagger] = \delta(\mathbf{k} - \mathbf{k}')\delta_{s,s'}$.

The final term in equation (3.7) is the interaction Hamiltonian which couples the excited atom and the photon modes. It is [141–143]

$$\hat{H}_I = \sum_{\mathbf{k},s} \left[-\hbar g_{\mathbf{k},s} \hat{a}_{\mathbf{k},s}^\dagger |g\rangle\langle e| + H.c. \right] \quad (3.8)$$

where we have introduced a shorthand notation of $g_{\mathbf{k},s}$ to denote the strength of each interaction term. Before discussing what $g_{\mathbf{k},s}$ is in this model, we note that the interpretation of (3.8) is clear: at the expense of transitioning the atom from the excited state to the ground state, we can create a photon of specified wave-vector and polarization with strength $g_{\mathbf{k},s}$, and we can also excite the atom from the ground state to the excited state at the cost of destroying a photon. The interaction strength is derived from a quantum-optics treatment [142], and it can be shown to be

$$g_{\mathbf{k},s} = -i \sqrt{\frac{\hbar\omega_{\mathbf{k}}}{2\epsilon_0 V}} \epsilon_{\mathbf{k},s} \langle g | \hat{\mathbf{d}} | e \rangle \quad (3.9)$$

where $\epsilon_0 \approx 8.854 \times 10^{-12} \text{ F}\cdot\text{m}^{-1}$ is the permittivity of free space, V is system volume, $\boldsymbol{\varepsilon}_{\mathbf{k},s}$ is the polarization vector of the given photon, and $\langle g | \hat{\mathbf{d}} | e \rangle$ is the dipole matrix element coupling the excited state to the ground state via the electromagnetic field [142].

Originally, Weisskopf and Wigner posited that any physically relevant solution to the Hamiltonian (3.7) would exhibit exponential decay, and from this assumption, they derived what the exponential decay rate would be. The virtue of this model as an instructive example of system plus reservoir models lies in the fact that an explicit solution can be found by solving Schrödinger's equation, which we shall demonstrate now. Because we are considering a restricted Hilbert-space having only one excitation present, the general solution to the time-dependent Schrödinger equation will be of the form

$$|\Psi(t)\rangle = A(t)e^{-i\omega_0 t}|e, 0\rangle + \sum_{\mathbf{k},s} B_k(t)e^{-i\omega_{\mathbf{k}} t}|g, 1_{\mathbf{k},s}\rangle \quad (3.10)$$

when working in the interaction picture [144]. We begin with an initially excited atom, so the initial condition is $A(t=0) = 1$ and $B_k(t=0) = 0$ for all \mathbf{k} . Substitution into (3.1) yields the following system of equations:

$$\dot{A}(t) = i \sum_{\mathbf{k},s} g_{\mathbf{k},s}^* e^{-i(\omega_{\mathbf{k}} - \omega_0)t} B_{\mathbf{k},s}(t) \quad (3.11)$$

$$\dot{B}_{\mathbf{k},s}(t) = ig_{\mathbf{k},s} e^{i(\omega_{\mathbf{k}} - \omega_0)t} A(t) \quad (3.12)$$

Formally, we can integrate (3.12) and substitute it into (3.11), which yields the intermediate result

$$\dot{A}(t) = - \sum_{\mathbf{k},s} |g_{\mathbf{k},s}|^2 \int_0^t dt' e^{-i(\omega_{\mathbf{k}} - \omega_0)(t-t')} A(t') \quad (3.13)$$

We note that this solution is formally exact. It is in principle solvable by realizing that a differential equation where the derivative of a function is proportional to its convolution with another function can be solved by the method of Laplace transforms. However, we note instead that the exponential in the integrand oscillates wildly if $\omega_{\mathbf{k}}$ and ω_0 differ, except when $t \approx t'$. We therefore make the approximate replacement $A(t') \rightarrow A(t)$ and remove it from the integrand in (3.13), yielding

$$\dot{A}(t) = - \sum_{\mathbf{k},s} |g_{\mathbf{k},s}|^2 A(t) \int_0^t dt' e^{-i(\omega_{\mathbf{k}} - \omega_0)(t-t')} \quad (3.14)$$

This approximation amounts to assuming that $A(t)$ varies slowly in time, which is a form of Markov approximation. Systems which are Markovian are said to be “memory-less”, that is, their evolution does not depend on their past history. Rather, the current state of a Markovian system fully determines its evolution a short time later, and by removing $A(t)$ from the integral in (3.13) to yield (3.14), we manifestly remove the system’s “memory of its previous trajectory”, hence justifying the name Markov approximation.

In order to proceed, we introduce some notation: let $\Delta_k = \omega_{\mathbf{k}} - \omega_0$ (independent of the wave-vector direction) and let $\tau = t - t'$. Changing the variable of integration in (3.14) from t' to τ and integrating yields

$$\int_0^t dt' e^{-i\Delta_k(t-t')} \approx \lim_{\varepsilon \rightarrow 0} \int_0^\infty d\tau e^{-i\Delta_k\tau - i\varepsilon\tau} = \lim_{\varepsilon \rightarrow 0} \frac{i}{\Delta_k - i\varepsilon} \quad (3.15)$$

where we have introduced an epsilon regulator ε in order to tame the integrand’s behavior at long times. Equation (3.14) now becomes

$$\dot{A}(t) = - \sum_{\mathbf{k}, s} |g_{\mathbf{k}, s}|^2 A(t) \lim_{\varepsilon \rightarrow 0} \frac{i}{\Delta_k - i\varepsilon} \quad (3.16)$$

and it becomes imperative that we treat the summation over wave-vectors and polarizations. Since we are considering a three dimensional system, we may replace the summand as

$$\sum_{\mathbf{k}, s} \rightarrow \frac{V}{(2\pi)^3} \int_0^\infty k^2 dk \int_0^\pi \sin \theta d\theta \int_0^{2\pi} d\phi \sum_{s=1}^2 \quad (3.17)$$

If we convert the momentum integral to energy by swapping the variable of integration from $k = |\mathbf{k}|$ to $\omega_k = ck$, and let $\mathbf{d}_{ge} = \langle g | \hat{\mathbf{d}} | e \rangle$, then (3.16) becomes

$$\begin{aligned} \dot{A}(t) &= - \int_0^\pi \sin \theta d\theta \int_0^\pi d\phi \sum_{s=1}^2 |\boldsymbol{\epsilon}_{\mathbf{k}, s} \cdot \mathbf{d}_{ge}|^2 A(t) \\ &\times \int_0^\infty \frac{d\omega_k}{c} \frac{\omega_k^2}{c^2} \frac{V}{(2\pi)^3} \frac{\omega_k}{2\epsilon_0 V \hbar} \lim_{\varepsilon \rightarrow 0} \frac{i}{\Delta_k - i\varepsilon} \end{aligned} \quad (3.18)$$

In order to make progress in (3.18), we note that the polarization sum can be shown to be

$$\sum_{s=1}^2 |\boldsymbol{\epsilon}_{\mathbf{k}, s} \cdot \hat{\mathbf{d}}_{ge}|^2 = |\mathbf{d}_{ge}|^2 \sin^2 \theta \quad (3.19)$$

and noticing that the ϕ integral contributes a factor of 2π , and with (3.19), the theta integral contributes

$$\int_0^\pi \sin \theta d\theta \sum_{s=1}^2 |\boldsymbol{\varepsilon}_{k,s} \cdot \hat{\mathbf{d}}_{ge}|^2 = |\mathbf{d}_{ge}|^2 \int_0^\pi \sin^3 \theta d\theta = \frac{4}{3} |\mathbf{d}_{ge}|^2 \quad (3.20)$$

and thus (3.18) becomes

$$\begin{aligned} \dot{A}(t) &= -\frac{1}{2} \frac{|\mathbf{d}_{ge}|^2}{4\pi\epsilon_0} \frac{4}{3\pi c^3 \hbar} A(t) \lim_{\varepsilon \rightarrow 0} \int_0^\infty d\omega_k \frac{i\omega_k^3}{(\omega_k - \omega_0) - i\varepsilon} \\ &= \text{Constants} \times \lim_{\varepsilon \rightarrow 0} \int_{-\omega_0}^\infty d\Delta_k \frac{i(\Delta_k + \omega_0)^3}{\Delta_k - i\varepsilon} \end{aligned} \quad (3.21)$$

where we have written the energy integral in a suggestive form.

At this point, we recall the Sokhotski-Plemelj theorem [145], whose statement is as follows: let $a < 0 < b$. The following replacement holds:

$$\lim_{\varepsilon \rightarrow 0^+} \int_a^b \frac{f(x)}{x \pm i\varepsilon} dx = \mp i\pi f(0) + \mathcal{P} \int_a^b \frac{f(x)}{x} dx \quad (3.22)$$

where here \mathcal{P} indicates the Cauchy principal-value. This is the formal underpinning of the common physicist's replacement

$$\frac{1}{x \pm i\varepsilon} \approx \mp i\pi \delta(x) + \mathcal{P} \frac{1}{x}. \quad (3.23)$$

(As an aside, the author was always uncomfortable using this replacement in course-work until discovering this rigorous formulation in a research context.) Returning to the matter at hand, we see that the integral in (3.21) satisfies the hypotheses of the theorem since in order to describe something physically real, $\omega_0 > 0$. We can thus utilize the Sokhotski-Plemelj theorem to write

$$\lim_{\varepsilon \rightarrow 0} \int_{-\omega_0}^\infty d\Delta_k \frac{i(\Delta_k + \omega_0)^3}{\Delta_k - i\varepsilon} = i\pi \times i(0 + \omega_0)^3 + i\mathcal{P} \int_{-\omega_0}^\infty d\Delta_k \frac{(\Delta_k + \omega_0)^3}{\Delta_k} \quad (3.24)$$

We therefore finally arrive at the solution to (3.14) by utilizing (3.24) in (3.21), and we find the (perhaps expectedly) simple form

$$\dot{A}(t) = \left(-\frac{\Gamma}{2} t + i\delta_L t \right) A(t) \quad (3.25)$$

where we have introduced the decay rate Γ arising from the first term in (3.24):

$$\Gamma = \frac{1}{4\pi\epsilon_0} \frac{4}{3} \frac{\omega_0}{\hbar c^3} |\mathbf{d}_{ge}|^2 \quad (3.26)$$

which is exactly the predicted spontaneous decay rate found in standard atomic physics references [146], and the Lamb-shift δ_L which arises from the second term in (3.24):

$$\delta_L = \frac{1}{4\pi\epsilon_0} \frac{2}{3} \frac{|\mathbf{d}_{ge}|^2}{\pi\hbar c^3} \mathcal{P} \int_0^{2m_e c^2/\hbar} d\omega_k \frac{\omega_k^3}{\omega_k - \omega_0} \quad (3.27)$$

where in order to avoid a divergently large integral in (3.27), we have cut off the upper limit of integration from infinity to the electron-positron pair production threshold. The population in the initially excited state decays exponentially with rate Γ , and the energy of the state is shifted by an amount δ_L [147].

We see from (3.25) that the population in our initially excited atom decays exponentially with a rate determined by properties of the atom and the electromagnetic field, namely, proportionally to $|\mathbf{d}_{ge}|^2$. This exponential decay appears to be a dissipative effect, however, we can think of it instead as a fully coherent evolution of a combined system and bath featuring an infinitely long beat note between the initially excited atom and all possible photon modes. If one is only concerned with the evolution of the system, then one can trace over the effects of the bath and arrive at an effective model featuring exponential decay. We note that without replacing the upper limit of integration in (3.27) by the pair production threshold for electrons and positrons, the integral diverges. This problem was originally resolved by Bethe [148] using mass-renormalization of the electron.

We have worked out this simple example in great detail for two reasons. First, the models presented in the following chapters will differ from the solution presented here in that the Markovian approximation will no-longer be applicable. In order to fully appreciate the richness of the non-Markovian solution, one must first grapple with the Markovian model. Secondly, in solving the Weisskopf-Wigner model, we arrived at a decay rate, but interestingly, we also arrived at a frequency shift, the celebrated Lamb shift of atomic physics. This connection between decay and energy shifts, a manifestation of the Kramers-Kronig relations, is quite profound in physics, and we will also see it again and again in the following work. We next turn our attention to a system plus reservoir model where we cannot make the Markov approximation, and in so doing, develop a model which is ripe for quantum simulation in an ultracold atom lab.

Chapter 4

Atomic spontaneous emission into structured reservoirs

This chapter is partly based on our publication *Analysis of non-Markovian coupling of a lattice trapped atom to free space*, Michael Stewart, Ludwig Krinner, Arturo Pasmiño, Dominik Schneble, Phys. Rev. A, **95**, 013626 (2017) [114] (section 4.3), and on our recent preprint *Fractional decay of matter-wave quantum emitters in a synthetic bandgap material*, Michael Stewart, Joonhyuk Kwon, Alfonso Lanuza, Dominik Schneble, arXiv:2003.02816 (2020) [149] (section 4.4).

4.1 Emission near a band gap

The spontaneous emission of photons from excited atoms is extremely sensitive to the density of states of the radiation field, and the observed emission behaviors thus depend upon whether an atom emits into free space (as in section 3.3) or else into a cavity or some kind of material structure. This modification of emission due to the density of states was first pointed out by Purcell in 1946 [95]. In the extreme case of an optical cavity, where the spectrum consists of a single state, an excited atom performs coherent vacuum Rabi oscillations for as long as the photon remains in the cavity, which is a stark deviation from an initially excited atom in free space [96, 150, 151]. In between these two regimes is the regime of an emission vacuum with a (singly or doubly) bounded, continuous spectrum of emission modes, for which stark deviations from exponential decay occur close to the energetic edge(s), realized decades later in the context of optical waveguides [96].

The latter scenario is realized in a photonic band-gap material, in which a periodic modulation of the index of refraction on the scale of the optical

wavelength creates a series of energy bands and gaps in which photos can propagate or are forbidden to propagate respectively. Such materials were theoretically considered first in the 1970s [97], and later (and independently) in the late 1980s [98, 99], and a range of emission phenomena beyond the Weisskopf-Wigner treatment were predicted, including modified spontaneous emission rates and spectral signatures [152–155], as well as atom-photon bound states [97–99]. As first proposed in 2008 [112], it is possible to realize the physics of modified spontaneous emission and bound states using ultracold atoms in optical lattices. It was later demonstrated theoretically [115–118, 122] that the original proposal for emission of free matter waves in 1D (mimicking emission near a single band edge) could be modified to include lattices and geometries leading to even more exotic fractional decays and couplings.

4.2 Matter-wave emission: overview

We have previously demonstrated that certain system plus reservoir models can be solved analytically, and in particular, we have shown that spontaneous emission of light from an excited atom is one such model. However, we made use of a Markovian approximation in deriving (3.14), which is perfectly reasonable for atoms emitting into free space. However, when such an atom emits into a photonic band gap material, as discussed in section 4.1, the density of states diverges near the band edges, and for emission near such divergences, it is impossible to make a Markov approximation. We will now present a model of spontaneous emission of massive matter-waves [114] which emulates the behavior of an atom emitting a photon near the bottom of a band in a PBG-material in one dimension, and we will show that the density of states has a profound effect on the observable dynamics. In particular, we show explicitly the transition between Markovian decay to non-Markovian, oscillatory decays featuring an observable population in the emitter at infinite times, called fractional decay. We will also demonstrate the existence of exotic, dynamically-bound states in the non-Markovian regime, and analyze their spatial structure. We note that the results of [112] consider a 3D system, whereas here we consider a 1D system. The stronger non-Markovianity in 1D can be difficult to observe in a material system [101], making our atomic simulator an even more attractive platform for such experiments. We then will generalize to a study of emission into a full band, again in 1D, rather than a semi-infinite continuum, highlighting the similarities and differences with the single edge case. We note finally that these models are experimentally realizable in an ultracold ^{87}Rb lab, and we will present experimental details and results in 5.

4.3 Emission near a single energetic edge

(This section presents the results of [114].) Behavior analogous to that of spontaneous emission in photonic band gap materials has been predicted for an atom-optical system consisting of an atom confined in a well of a state-dependent optical lattice that is coupled to free space through an internal-state transition [112]. Using the Weisskopf-Wigner approach and considering a one-dimensional geometry, we analyze the properties of this system in detail, including the evolution of the lattice-trapped population, the momentum distribution of emitted matter waves, and the detailed structure of an evanescent matter-wave state below the continuum boundary. We compare and contrast our findings for the transition from Markovian to non-Markovian behaviors to those previously obtained for three dimensions.

4.3.1 Introduction to the 1D model

As first proposed in [112], ultracold atoms in state selective optical lattices can be used to simulate spontaneous emission of photons in a PBG-material. With an eye on experimental implementations [83, 156, 157], we set up the following model: an atom in a tightly-confining well of a deep optical lattice (with negligible tunneling to other wells) is coupled to unconfined states via a near-resonant coupling field of frequency ω_μ , cf. figure 4.1(A). The trapped atom, in the internal state $|a\rangle$, is assumed to be in the harmonic-oscillator ground state with energy $\hbar\omega_a = \hbar\omega_a^0 + d\hbar\omega_0/2$ where $\hbar\omega_a^0$ is the bare (untrapped) energy of $|a\rangle$, and d is the system dimensionality (we will set $d = 1$ after deriving the Hamiltonian in full generality.) The wavefunction in the well is Gaussian,

$$\phi_0(\mathbf{r}) = \frac{1}{\pi^{d/4}a_{ho}^{d/2}} \exp\left[\frac{-\mathbf{r}^2}{2a_{ho}^2}\right] \quad (4.1)$$

with $a_{ho} = \sqrt{\hbar/m\omega_0}$ the harmonic oscillator length.

The atoms in the unconfined state are assumed to be simple plane waves $\psi_{\mathbf{k}}(\mathbf{r}) = \exp(i\mathbf{k} \cdot \mathbf{r})/L^{d/2}$, having momentum \mathbf{k} and kinetic energy $E_k = \hbar^2 k^2/2m$, where $L \rightarrow \infty$. These states sit on an energy floor associated with the internal energy of $|b\rangle$, namely $\hbar\omega_b = \hbar\omega_b^0$. The system Hamiltonian can be written as

$$\hat{H} = \sum_{j=a,b} \int d^d r \hat{\Psi}_j^\dagger(\mathbf{r})(H_j + \hbar\omega_j^0)\hat{\Psi}_j(\mathbf{r}) + \hat{H}_{ab} \quad (4.2)$$

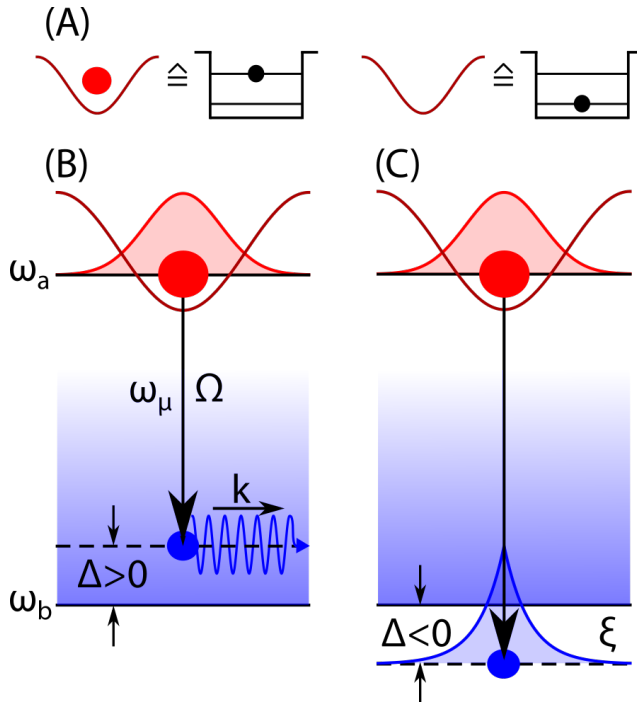


Figure 4.1: Decay mechanism for an atom confined to a well of a deep, state-selective lattice potential with coupling to a continuum of momentum modes through an internal state transition. (A) The population in the well can be viewed as an occupational spin represented by an excited state (contain 1 atom) or ground state (contain 0 atoms). The coupling, with strength given by the Rabi frequency Ω and frequency ω_μ , can be tuned to positive (B) or negative (C) detunings Δ around the (zero-momentum) boundary of the mode continuum. In (B), k is the momentum of the resonantly coupled freely propagating mode. In (C), an evanescent matter wave with decay length ξ is formed.

with the interaction

$$\hat{H}_{ab} = \frac{\hbar\Omega_1}{2} \int d^d r e^{-i\omega_\mu t} \hat{\Psi}_a(\mathbf{r}) \hat{\Psi}_b^\dagger(\mathbf{r}) \hat{\mu}(\mathbf{r}) + H.c. \quad (4.3)$$

The operator $\hat{\mu}(\mathbf{r})$ annihilates a coupling field quantum. Assuming the coupling field to be classical, $\hat{\mu}(\mathbf{r})$ can be replaced by its expectation value $\langle \hat{\mu} \rangle = \sqrt{N} \approx \sqrt{N+1} = \langle \hat{\mu}^\dagger \rangle$, and can be pulled out of the integral to re-scale the single-photon Rabi frequency to the N -photon Rabi frequency, $\Omega_N = \sqrt{N}\Omega_1 \equiv \Omega$.

To proceed, the field operators in (4.3) are expanded in the basis of states

discussed above:

$$\hat{\Psi}_a(\mathbf{r}) = \phi_0(\mathbf{r}) e^{-i\omega_a t} \hat{a} \quad (4.4)$$

$$\hat{\Psi}_b(\mathbf{r}) = \sum_{\mathbf{k}} \psi_{\mathbf{k}}(\mathbf{r}) e^{-i(E_k/\hbar + \omega_b)t} \hat{b}_{\mathbf{k}} \quad (4.5)$$

The bare-Hamiltonian terms do not contribute to the Schrödinger equation governing the time evolution of the state amplitudes in the interaction picture. Hence, the interaction Hamiltonian becomes

$$\begin{aligned} \hat{H}_{ab} &= \frac{\hbar\Omega}{2} \sum_{\mathbf{k}} \exp[-i(\omega_{\mu} + \omega_a)t + i(E_k/\hbar + \omega_b)t] \hat{a} \hat{b}_{\mathbf{k}}^\dagger \int d^d r \phi_0(\mathbf{r}) \psi_{\mathbf{k}}^*(\mathbf{r}) + H.c. \\ &= \sum_{\mathbf{k}} \frac{\hbar\Omega}{2} e^{i\Delta_k t} \gamma_{\mathbf{k}} \hat{a} \hat{b}_{\mathbf{k}}^\dagger + H.c. \end{aligned} \quad (4.6)$$

where Δ_k is a k -dependent detuning and $\gamma_{\mathbf{k}}$ is a Franck-Condon overlap:

$$\Delta_k = \frac{\hbar k^2}{2m} - \Delta; \quad \Delta = \omega_{\mu} - (\omega_b - \omega_a) \quad (4.7)$$

$$\gamma_{\mathbf{k}} = \int d^d r \phi_0(\mathbf{r}) \psi_{\mathbf{k}}^*(\mathbf{r}) \quad (4.8)$$

The atom can either be in the trapped state with no freely propagating modes occupied, $|1_a, \{0\}_{\mathbf{k}}\rangle$, or it can be in the untrapped state with a freely propagating excitation present, $|0_a, 1_{\mathbf{k}}\rangle$, and hence we represent $\hat{a} = |0_a\rangle \langle 1_a|$. (Note that this reduced Hilbert space has exactly the same form as the Hilbert space of the Weisskopf-Wigner model discussed in section 3.3.) The interaction Hamiltonian is then reduced to the form

$$\hat{H}_{ab} = \sum_{\mathbf{k}} \frac{\hbar\Omega}{2} \gamma_{\mathbf{k}} e^{i\Delta_k t} \hat{b}_{\mathbf{k}}^\dagger |0_a\rangle \langle 1_a| + H.c. \quad (4.9)$$

By identifying $|0_a\rangle$ and $|1_a\rangle$ with the ground and excited states of an occupational spin as defined in fig. 4.1(A), and upon introducing $g_{\mathbf{k}} = \Omega \gamma_{\mathbf{k}}/2$, (4.9) exactly reproduces the standard Weisskopf-Wigner Hamiltonian for the description of spontaneous photon emission from a two-level atom [141] in the interaction picture, albeit with different momentum dependences in the $g_{\mathbf{k}}$ and Δ_k terms. The differences are caused by the quadratic dispersion relation of the matter-waves, which coincides with that of light in a PBG material [153]. We note that, while the coupling to the continuum requires the introduction of the external drive, this does not affect the structure of the Hamiltonian,

in which the coupling is a simple constant in either case, albeit with different strength which can be modulated in general, and for which spontaneous emission arises for selected strengths.

4.3.2 Population dynamics

In order to contextualize what we have done, we briefly consider what roles the trapped atom and freely propagating modes play. The states $|1_a\rangle$ and $|0_a\rangle$ of the trapped atom (occupational spin) are our small system \mathcal{S} of interest, and the propagating matter wave modes $|1_{\mathbf{k}}\rangle$ represent the reservoir \mathcal{R} of our system plus reservoir model. In analogy with the Weisskopf-Wigner model, we will attempt a direct solution of the model for a certain initial condition, and we will demonstrate that the dynamics are strongly modified compared to the free space case. Furthermore, without explicitly tracing over the reservoir degrees of freedom, we recover a transition from mostly Markovian behavior to strongly non-Markovian behavior.

To proceed, we follow the usual approach of expanding the initial state as [141]

$$|\Psi(t)\rangle = A(t)|1_a, \{0\}_{\mathbf{k}}\rangle + \sum_{\mathbf{k}} B_{\mathbf{k}}(t)|0_a, 1_{\mathbf{k}}\rangle \quad (4.10)$$

where, due to the choice of the interaction picture, the dynamical phases have been left in the Hamiltonian. Application of the Hamiltonian (4.9) to this initial state, left multiplication by $\langle 1_a, \{0\}_{\mathbf{k}} |$ or $\langle 0_a, 1_{\mathbf{k}} |$, and cancellation of terms arising from the bare Hamiltonian, then results in the following system of differential equations for the state amplitudes:

$$\dot{A}(t) = i \sum_k g_{\mathbf{k}}^* e^{-i\Delta_k t} B_{\mathbf{k}}(t) \quad (4.11)$$

$$\dot{B}_{\mathbf{k}}(t) = ig_{\mathbf{k}} e^{i\Delta_k t} A(t) \quad (4.12)$$

For concreteness, we note that the dimensionality d modifies the Franck-Condon factor (4.8). We will be interested in experiments in one spatial dimension, and so we specialize to the case of $d = 1$ now.

To determine the time-dependent amplitude $A(t)$ of the population trapped in the well, we proceed in analogy to the treatment of an excited atom coupled to a PBG material [153]. In our case, the excited (ground) state of the emitting atom is replaced by the occupational spin in the well. A straightforward computation for $d = 1$ shows that

$$\gamma_k = \sqrt{\frac{2\pi^{1/2}a_{ho}}{L}} \exp\left[-\frac{1}{2}k^2a_{ho}^2\right] \quad (4.13)$$

Next, (4.12) is formally integrated and inserted into (4.11). With the assumption that the momenta are closely spaced, i.e. that L diverges (for a typical experiment, this assumption can be cast in terms of a limit on energetic resolution, c.f. section (REF)), the sum in (4.11) is replaced by an integral, and the result for the excited-state amplitude with (4.13) is

$$\dot{A}(t) = -\frac{a_{ho}(\Omega/2)^2}{\sqrt{\pi}} \int_{-\infty}^{\infty} dk \int_0^t dt' e^{-k^2 a_{ho}^2} e^{i\Delta_k(t-t')} A(t') \quad (4.14)$$

where the explicit dependence on the system size L from the Franck-Condon factor is canceled out by the usual replacement $\sum_k \rightarrow (L/2\pi) \int dk$.

It is here that our approach first differs from that in section 3.3. Specifically, due to the form of the matter wave dispersion relation, i.e. $\omega_k \propto k^2$, we can analytically compute the k -integral first before attempting to compute the time-integral in (4.14). Said another way, we do not invoke the Markov approximation here, and our solution going forward should be understood to not depend on the separation of system and reservoir timescales which such an approximation requires. In fact, the full solution to (4.14) will exhibit regimes in which the reservoir acts back strongly on the system and exchanges population for many cycles before damping.

The k integration is carried out first in closed form, as it is simply a Gaussian integral, giving

$$\dot{A}(t) = -\sqrt{2} \int_0^t dt' A(t') \frac{(\Omega/2)^2 e^{i\Delta(t-t')}}{\sqrt{2 + i\omega_0(t-t')}} \quad (4.15)$$

which can also be re-written in the form

$$\dot{A}(t) = - \int_0^t dt' A(t') G_{1D}(t-t') \quad (4.16)$$

with the correlation function of the continuum [122] (bath correlation function)

$$G_{1D}(\tau) = \frac{(\Omega/2)^2}{\sqrt{1 + i\omega_0\tau/2}} e^{i\Delta\tau} \quad (4.17)$$

Eq. (4.16) is easily solved by the Laplace transform method. Denoting by $\tilde{f}(s)$ the Laplace transform of a function $f(t)$

$$\tilde{f}(s) = \mathcal{L}\{f(t)\} = \int_0^\infty f(t) e^{-st} dt \quad (4.18)$$

and using its standard relations, specifically the convolution property

$$\mathcal{L} \left\{ \int_0^t f(t')g(t-t')dt' \right\} = \mathcal{L} \{(f * g)(t)\} = \tilde{f}(s)\tilde{g}(s) \quad (4.19)$$

we can show that in Laplace space, eq. (4.16) results in

$$\tilde{A}(s) = \frac{1}{s + \tilde{G}_{1D}(s)} \quad (4.20)$$

where we have chosen the specific initial condition that the emitter is initially excited, i.e. $A(t=0) = 1$ and $B_k(t=0) = 0$ for all k .

We can solve (4.20) by inversion, which for the case at hand has the formal solution

$$\begin{aligned} e^{-i\Delta t} A(t) &= \frac{1}{2\pi i} \int_{\epsilon-i\infty}^{\epsilon+i\infty} ds \tilde{A}(s + i\Delta) e^{st} \\ &= \frac{1}{2\pi i} \int_{\epsilon-i\infty}^{\epsilon+i\infty} ds \frac{e^{st}}{s + i\Delta + \tilde{G}_{1D}(s + i\Delta)} \end{aligned} \quad (4.21)$$

with ϵ chosen such that all singularities of the integrand lie to the left of the integration contour, which in this case is a vertical line (Bromwich contour).

In general, eq. (4.21) cannot be solved analytically, but progress can be made, as in the 3D case [122], by making the assumption of strong *confinement*¹ $\omega_0 \gg s, \Delta$, or equivalently $|\eta| = |(\Delta + is)/\omega_0| \ll 1$. Physically, this is tantamount to assuming that the Wannier function for the trapped a atom is made up of contributions due to many different plane waves. This assumption does not accurately capture times below ω_0^{-1} , so the model is expected to break down at very short times. The Laplace transform of the bath correlation function (written in terms of the previously defined η) is

$$\tilde{G}_{1D}(\eta) = -\sqrt{2\pi} \frac{\Omega^2}{4\omega_0} i\eta^{-1/2} e^{-2\eta} \left(i + \text{Erfi}(\sqrt{2\eta}) \right) \quad (4.22)$$

where Erfi is the imaginary error function defined with respect to the usual error function Erf as follows:

$$\text{Erfi}(z) = -i\text{Erf}(iz) \quad (4.23)$$

In strong coupling to leading order in η (keeping only the constant and negative

¹Note that we erroneously referred to this approximation as strong coupling in [114]. The name strong confinement accurately reflects the assumption we are making.

power terms), this becomes

$$\tilde{G}_{1D}(s) \approx -i\delta_L + \frac{C(1-i)}{\sqrt{s-i\Delta}}; \quad \delta_L = \frac{\Omega^2}{\omega_0}; \quad C = \frac{\sqrt{\pi}}{4} \frac{\Omega^2}{\sqrt{\omega_0}} \quad (4.24)$$

and therefore one must evaluate

$$e^{-i\Delta t} A(t) = \frac{1}{2\pi i} \int_{\epsilon-i\infty}^{\epsilon+i\infty} ds \frac{e^{st}}{s + i\tilde{\Delta} + C(1-i)/\sqrt{s}} \quad (4.25)$$

The quantity $\delta_L = \Omega^2/\omega_0$ in (4.24) corresponds to a Lamb shift of the detuning to

$$\tilde{\Delta} = \Delta - \delta_L = \Delta - \Omega^2/\omega_0 \quad (4.26)$$

The inversion of (4.25) is now a straightforward exercise in examining the singularities of the integrand and deforming around a branch cut. The solution, using the notation of [153], can be written as

$$A(t) = \exp(i\Delta t) \left[\sum_j \frac{2u_j^2}{3u_j^2 + \tilde{\Delta}} \exp(iu_j^2 t) + e^{-i\pi/4} \frac{D}{\pi} \int_0^\infty \frac{\zeta^{1/2} \exp(-\zeta t) d\zeta}{\zeta^3 - 2i\tilde{\Delta}\zeta^2 - \tilde{\Delta}^2\zeta - iD^2} \right] \quad (4.27)$$

with $D = \sqrt{2}C$. The u_j 's are the roots of

$$u^3 + \tilde{\Delta}u - D = 0 \quad (4.28)$$

such that $-3\pi/4 < \arg(u_j) < \pi/4$ to ensure that the roots u_j do not lie on the branch cut in s -space. We comment here that the dimensions of D are $[D] = T^{-3/2}$, which is a consequence of working in one spatial dimension with freely propagating matter waves. For convenience, we define a frequency scale (equivalently timescale)

$$\tilde{\Omega} = D^{2/3} = \left(\pi \frac{\Omega}{\omega_0} \right)^{1/3} \frac{\Omega}{2} \quad (4.29)$$

which sets the scale over which the dynamics occur. We shall later see that $\tilde{\Omega} \approx 0.3\Omega$ in experimental contexts.

Since (4.27) is analytic, it can be evaluated over any range of interest; an example with the salient features is shown in fig. 4.2. In analogy to what is observed in PBG materials near a band gap [153, 158], depending on the detuning there is a transition from a (nearly) exponential decay to oscillatory

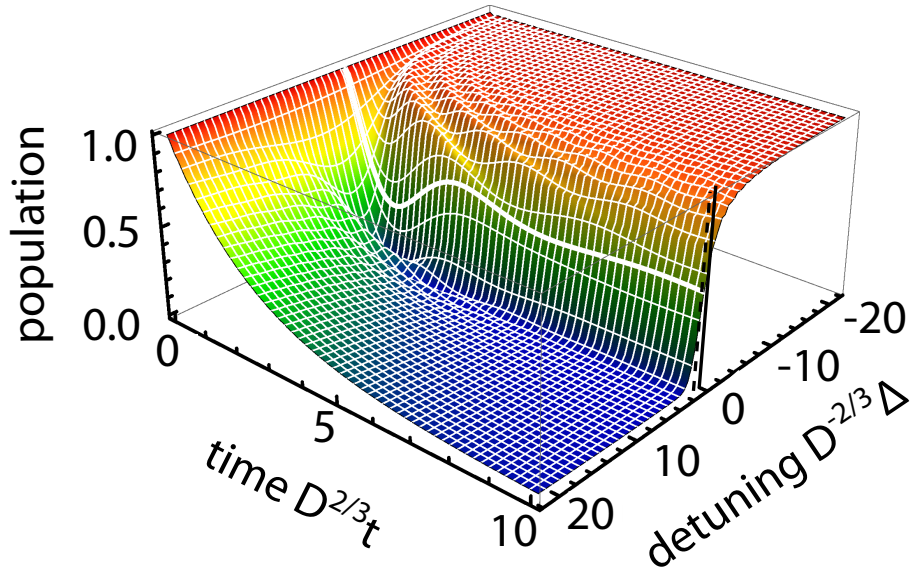


Figure 4.2: Computed population $|A(t)|^2$ in the potential well as a function of drive time and detuning in characteristic time and frequency units. The thick white curve corresponds to $\Delta = 0$ (see vertical solid line), and the Lamb shift is $\delta_L/\tilde{\Omega} = 0.1$ (see the dotted vertical line on the detuning axis). The chosen frequency scale is $\tilde{\Omega}/2\pi \approx 200$ Hz. For the depicted plot, ω_0 and Ω are fixed by matching to experimentally reasonable values ($\omega_0 \approx 2\pi \times 30$ kHz and $\Omega/\omega_0 = 0.03$).

behavior, in which the atomic population decays slightly but remains trapped in the well.

For large positive detunings $\Delta \gg 0$, the system is so far away from the continuum boundary that the density of levels looks essentially unchanged from the original situation considered by Weisskopf and Wigner. In this regime, one may make the standard Markov approximation, the details and results of which can be found in the appendix. In particular, the population is found to decay exponentially with a rate $\Gamma = \delta_L \sqrt{\pi \omega_0 / 2\Delta} \exp(-2\Delta/\omega_0)$, c.f. (4.41).

For detunings that are smaller than the Lamb shift, $\Delta < \delta_L$ (this includes arbitrarily large negative detunings), the population in the well does not decay completely, even for arbitrarily long times. This is a consequence of the fact that eq. (4.28) has a real root for $\Delta \lesssim 0$, i.e. for $\Delta \lesssim \delta_L$, which signals that the solution has an imaginary pole at $s = -iu_j^2$, corresponding to a long-lived excitation. This excitation is a dressed state which evolves at the frequency determined by the real root of eq.(4.28). (We will show in section 4.3.5 how this mathematical object corresponds to a long-lived bound-state of an emitter

dressed with a cloud of approximately exponentially localized matter-waves.)

The behavior for $\Delta = 0$, i.e. the resonant case, is reminiscent of a damped Rabi oscillation, though the frequency appears to vary weakly with time. (For much stronger couplings than considered here, the trap potential and the flat continuum hybridize into dressed potentials, eventually leading to an undamped Rabi oscillation [86]). We note that the case under consideration in fig. 4.2 corresponds roughly to the small coupling limit considered in [86], however with an initial state having a broad momentum spread.

In contrast to 3D results discussed in [112], the oscillations in the population in the 1D case persist for many characteristic times at negative detunings. Furthermore, the decay rate is maximum at detunings around δ_L , and it becomes slower as the detuning is increased. The pronounced oscillatory behavior in 1D is consistent with the divergence of the 1D density of states at zero energy. While the fundamental differences between 1D and 3D systems would be difficult to measure in PBG materials [101] (see also [105]), the tunability of the atom-optical system makes it an ideal candidate for the exploration of dimensional effects.

4.3.3 Markovian limit

We note that while we do not have to resort to a Markov approximation to solve (4.14), we can invoke it and compare the results to the full solution, as well as make contact with the results from Fermi's Golden Rule for time dependent transition amplitudes, and we find it instructive to do so. The computation which follows here is essentially the same as that of 3.3, and as such, we shall omit details which are essentially already presented.

The starting point for a Markov approximation treatment is again assuming that in (4.14), the exponential term oscillates quickly except for times $t-t' \approx 0$, so we will replace $A(t')$ by $A(t)$ and remove it from within the time integral. We can then evaluate the exponential time integral at the cost of introducing an epsilon-regulator, recalling (3.15). The expression for the excited emitter population is thus

$$\dot{A}(t) = -\frac{a_{ho}\Omega^2}{4\sqrt{\pi}} A(t) \lim_{\varepsilon \rightarrow 0} \int_0^\infty dk \frac{2ie^{-k^2 a_{ho}^2}}{\Delta_k + i\varepsilon} \quad (4.30)$$

wherein we have used the fact that the integrand is an even function of k in order to change the limits of integration and introduce a factor of two. We recall that $\Delta_k = \hbar k^2/2m - \Delta$, and thus we are motivated to introduce the

following change of variables

$$\omega = \frac{\hbar k^2}{2m}; d\omega = \frac{\hbar k}{m} dk; a_{ho} dk = \frac{1}{\omega_0} \sqrt{\frac{\omega_0}{\omega}} d\omega; a_{ho}^2 k^2 = 2 \frac{\omega}{\omega_0} \quad (4.31)$$

and using (4.31) in (4.30), we rewrite the equation in the form

$$\dot{A}(t) = -A(t) \frac{\delta_L}{\sqrt{2^3 \pi}} \lim_{\varepsilon \rightarrow 0} \int_0^\infty d\omega \sqrt{\frac{\omega_0}{\omega}} \frac{i e^{-2\omega/\omega_0}}{\omega - \Delta + i\varepsilon} \quad (4.32)$$

with $\delta_L = \Omega^2/\omega_0$ as in 4.3.2. It is now our intention to make use of the Sokhotski-Plemelj theorem (3.22), however our integrand does not yet satisfy the hypotheses of the theorem. To this end, we shift the integration variable to a new variable $\omega' = \omega - \Delta$, in terms of which (4.32) becomes

$$\dot{A}(t) = -A(t) \frac{\delta_L}{\sqrt{2^3 \pi}} \lim_{\varepsilon \rightarrow 0} \int_{-\Delta}^\infty d\omega' \sqrt{\frac{\omega_0}{\omega' + \Delta}} \frac{i e^{-2(\omega' + \Delta)/\omega_0}}{\omega' + i\varepsilon} \quad (4.33)$$

Now, we will apply the Sokhotski-Plemelj theorem, i.e. use the replacement $1/x + i\varepsilon = -i\pi\delta(x) + \mathcal{P}(1/x)$, but we must be careful to understand what we are doing. In particular, we must consider that Δ is a signed quantity which may be positive or negative (or zero), so we consider two cases. First, for positive detunings $\Delta > 0$, the hypotheses of the theorem are manifestly satisfied, so we may write (calling the $\lim_{\varepsilon \rightarrow 0} \int \dots$ terms in (4.33) $\mathcal{I}(\Delta, \omega_0)$)

$$\mathcal{I}(\Delta > 0, \omega_0) = \pi \sqrt{\frac{\omega_0}{\Delta}} e^{-2\Delta/\omega_0} \left[1 - i \operatorname{Erfi} \left(\sqrt{2 \frac{\Delta}{\omega_0}} \right) \right] \quad (4.34)$$

consisting of both a real and imaginary part. Secondly, we can likewise consider the case of negative detunings, i.e. $\Delta < 0$, for which $-\Delta = |\Delta| > 0$. In this case, the hypotheses of the Sokhotski-Plemelj theorem are *not* satisfied, however, as the integrand does not contain any singularities over the region of integration, we may simply evaluate the integral, yielding

$$\mathcal{I}(\Delta < 0, \omega_0) = i\pi \sqrt{\frac{\omega_0}{|\Delta|}} e^{-2\Delta/\omega_0} \operatorname{Erfc} \left(\sqrt{2 \frac{|\Delta|}{\omega_0}} \right) \quad (4.35)$$

with Erfc the complimentary error function $\operatorname{Erfc}(z) = 1 - \operatorname{Erf}(z)$. For negative detunings, the result is purely imaginary. Denoting by $\Theta(z)$ the Heaviside step

function, we can condense our results and rewrite (4.33) as

$$\dot{A}(t) = -A(t) \frac{\delta_L}{2} \sqrt{\frac{\pi\omega_0}{2|\Delta|}} e^{-2\Delta/\omega_0} \left\{ \left[1 - i \text{Erfi} \left(\sqrt{2\frac{\Delta}{\omega_0}} \right) \right] \Theta(\Delta) - i \text{Erfc} \left(\sqrt{2\frac{|\Delta|}{\omega_0}} \right) \Theta(-\Delta) \right\} \quad (4.36)$$

The solution to (4.36) is exponential with an imaginary part corresponding to a frequency shift and a real part for positive detunings only which corresponds to a decay. That is

$$n(t) = |A(t)|^2 = \exp \left(-\delta_L \sqrt{\frac{\pi\omega_0}{2|\Delta|}} e^{-2\Delta/\omega_0} \Theta(\Delta) \times t \right) \quad (4.37)$$

We note that this differs from our non-Markovian solution (4.27), where even for negative detunings we have some decay of the population. For the regime in which $\Delta/\Omega \gg 1$, the Markovian and non-Markovian solutions converge.

The Markovian decay rate furthermore must also arise in a treatment due to Fermi's Golden Rule. Specifically, the decay rate $dn(t)/dt \equiv \Gamma$ must be reproduced by

$$\Gamma = \frac{2\pi}{\hbar} |\langle 0_a | \hat{H}_I | 1_a \rangle|^2 \rho(E = \hbar\Delta) \quad (4.38)$$

where $\rho(E)$ is the density of states and $|\langle 0_a | \hat{H}_I | 1_a \rangle|^2$ is a squared transition matrix element arising from the interaction Hamiltonian. For our system of interest, these are

$$\rho(E = \hbar\Delta) = \frac{L}{\pi\hbar} \sqrt{\frac{m}{2\hbar\omega_0}} \sqrt{\frac{\omega_0}{\Delta}} \Theta(\Delta) \quad (4.39)$$

and

$$|\langle 0_a | \hat{H}_I | 1_a \rangle|^2 = \frac{\hbar^2 \Omega^2 \pi^{1/2}}{2L} \sqrt{\frac{\hbar}{m\omega_0}} e^{-2\Delta/\omega_0} \quad (4.40)$$

Combining these results in (4.38), we recover

$$\Gamma = \delta_L \sqrt{\frac{\pi\omega_0}{2|\Delta|}} e^{-2\Delta/\omega_0} \Theta(\Delta) \quad (4.41)$$

in full agreement² with (4.37).

²Equation 4.41 corrects a typo in the in-line equation for Γ in section III of [114].

4.3.4 Momentum distribution of the emitted matter-waves

It is common in ultracold atom experiments to use time-of-flight imaging as an experimental probe and thus gain access to the momentum distribution of the ultracold atomic cloud. For this reason, it is highly interesting to consider the momentum composition of the radiation which is emitted from our initially excited emitter. In particular, the coupled differential equations (4.11) and (4.12) contain the amplitudes of both the occupied well and the emitted matter waves. Using eq (4.27) for $A(t)$, we may formally integrate the eq. (4.12) for $\dot{B}_k(t)$, leading to

$$B_k(t) = i \frac{\Omega}{2} \sqrt{\frac{2\pi^{1/2} a_{ho}}{L}} e^{-k^2 a_{ho}^2/2} \int_0^t e^{i\Delta_k t'} A(t') dt' \quad (4.42)$$

The absolute square of (4.42) gives the time-dependent momentum distribution:

$$L|B_k(t)|^2 = \sqrt{\pi} \frac{\Omega^2}{2} a_{ho} e^{-k^2 a_{ho}^2} \left| \int_0^t \exp \left[i \left(\frac{\hbar k^2}{2m} - \Delta \right) t' \right] A(t') dt' \right|^2 \quad (4.43)$$

which for long times defines the emission spectrum as a function of k :

$$S(\omega_k) = \lim_{t \rightarrow \infty} |B_k(t)|^2. \quad (4.44)$$

Note that in the nomenclature and formalism of [155], this matter wave emitter corresponds to a $\gamma = \sqrt{2\pi}\Omega^2/\omega_0$ and $F(\omega_k) = \exp(-2\omega_k/\omega_0)\sqrt{\omega_0/\omega_k}\Theta(\omega_k)$, a spectral weight function not previously considered.

Using the numerical solution for $A(t)$ with parameters $0 \leq t' \leq t$, Δ , Ω , and ω_0 , the integral in (4.43) and the momentum distribution $L|B_k(t)|^2$ can then be computed numerically. An example for the Markovian limit is shown in fig. 4.3A. The doubly-peaked momentum structure is characteristic of a system in 1D with left-right symmetry; while the individual peaks are not generally symmetric around their centers, their location varies with detuning in a simple way. The detuning supplies a kinetic energy $\hbar\tilde{\Delta} = \hbar(\Delta - \delta_L)$ to the transferred atoms, which corresponds to a particular momentum

$$k(E_{kin})/k_{rec} = \sqrt{\hbar\tilde{\Delta}/\hbar\omega_{rec}} \quad (4.45)$$

where we have introduced $\hbar\omega_{rec} = (\hbar k_{rec})^2/2m$ with $k_{rec} = 2\pi/\lambda_{latt}$ and λ_{latt} the wavelength of the optical lattice. Fig. 4.3B shows the extracted peak loca-

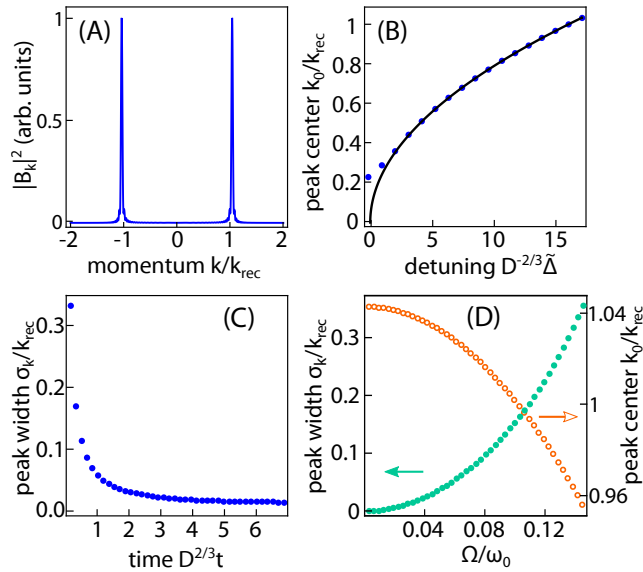


Figure 4.3: Momentum distributions of emitted matter waves (positive detunings, Markovian limit). (A) Sample momentum distribution taken at time $\tilde{\Omega}t \approx 1.5$ and positive detuning $\tilde{\Delta}/\tilde{\Omega} \approx 17$. The width and position of the peaks depends on time and detuning, but the shape is representative for a large range of parameters. (B) Calculated momentum peak position k_0 (in units of k_{rec} , see text) as a function of detuning $\tilde{\Delta}/\tilde{\Omega}$ for $\tilde{\Omega}t \approx 4.0$. The solid curve is a guide to the eye for the expected momentum based on exact energy conservation (see text). (C) Momentum peak width vs. time for $\tilde{\Delta}/\tilde{\Omega} \approx 17$, saturating at a value set by the decay rate (see text). (D) Momentum peak width (green, filled circles, left vertical axis) and momentum peak position (orange, unfilled circles, right vertical axis) vs. Rabi frequency Ω for $\tilde{\Omega}t \approx 1.5$ and $\tilde{\Delta}/\tilde{\Omega} \approx 17$. The peak width is obtained as the standard deviation about one peak in (A).

tion, k_0 , given by the computed center-of-mass in fig. 4.3A from the numerical data, as well as a no-free-parameter fit to the data of square-root form. The close agreement with the simulated data degrades at small detunings, where the doubly-peaked structure is lost due to edge effects near the boundary, such that one characteristic momentum in this regime cannot be identified. This is one indicator of the strongly non-Markovian character of emission near the band edge where the density of states diverges.

It is also seen that the momentum distribution evolves in time, starting from wide peaks and tending to a tightly confined value, cf. 4.3C. To understand this behavior, consider that in the Markovian regime, the decay is

exponential, and so will have an (approximately) Lorentzian emission spectrum $S(\omega)$ [155]. The width of the momentum distribution is limited at early times by the corresponding spectral Fourier width ($\Delta t \Delta \omega \approx 1$), but at long times should tend to a finite value set by the line width Γ of the excited state, given by (4.41). Indeed, computation of the emission spectrum $S(\omega)$ (not shown) by an appropriate change of variables (i.e. momentum to energy), and extracting its width, c.f. fig. 4.3(C), yields a value of 1.25Γ for long times, in good qualitative agreement with the expectation.

So far, the discussion of fig. 4.3 has focused on a fixed Rabi frequency Ω . When Ω is varied, both the decay rate Γ and the Lamb shift δ_L change proportionally to Ω^2 . Thus, the width in kinetic energy (i.e. the width of momentum squared) at long times should vary quadratically with Ω , and indeed, the extracted *momentum* width increases approximately linearly with Ω . Furthermore, the extracted peak separation decreases with increasing Rabi frequency as the growing Lamb shift δ_L pulls the lattice-trapped state to a lower energy.

4.3.5 Matter-wave bound states

The decay of the population in the initially excited emitter decays to a non-zero value for a finite range of detunings Δ , most notably, for negative detunings, where the decay of the excited state population is small and oscillatory, c.f. fig. 4.2. This is the result of the presence of a bound state that the system supports and which does not decay in time. We now elucidate the origin of this bound state and demonstrate that it has a simple form.

First, we can write the differential equations for the emitter and the emitted momentum components, (4.11) and (4.12) using ω rather than k as our label, in Laplace transformed space as

$$\tilde{A}(s + i\Delta) = [s + i\Delta + \tilde{G}(s)]^{-1} \quad (4.46)$$

$$\tilde{B}_\omega(s) = \frac{-i\gamma^*(\omega)\tilde{A}(s + i\Delta)}{s + i\omega} \quad (4.47)$$

where in general $\tilde{G}(s)$ is the Laplace transform of the bath correlation function (4.17). In general, this quantity is computed as

$$\tilde{G}_{bath}(s) = \int_0^\infty \frac{\mathcal{G}(\omega)}{s - \omega} d\omega \quad (4.48)$$

again, having switched to an energy viewpoint rather than a momentum viewpoint at the cost of introducing a density of states $\rho(\omega)$. The function

$\mathcal{G}(\omega) = |\gamma(\omega)|^2 \rho(\omega)$, with $\gamma(\omega)$ the Franck-Condon factor (4.13) expressed as a function of energy instead of momentum. For completeness, in this model, these quantities take the form

$$|\gamma(\omega)|^2 = \frac{\sqrt{\pi} a_{ho}}{L} \frac{\Omega^2}{2} e^{-2\omega/\omega_0}; \quad \rho(\omega) = \frac{L}{\pi} \sqrt{\frac{2m}{\hbar\omega}} \quad (4.49)$$

Now, in order to learn about the excitation spectrum of the system, we analyze (4.46), and we realize that the singularities in the denominator will correspond to stable or unstable excitations. In particular, suppose that there is a purely imaginary pole of the form $s = -i\omega_B$. We will discuss under which conditions this is possible in what follows. However, for the moment if we just assume that such a solution exists, then from the Cauchy residue theorem, it must correspond to a non-decaying exponential term in the solution for $A(t)$. To see this, it is enough to first note that the pole will lie to the left of the Bromwich integration contour, and thus schematically

$$A(t) = \frac{1}{2\pi i} \int_{\zeta-i\infty}^{\zeta+i\infty} \tilde{A}(s) e^{st} ds = \text{Res}_{-i\omega_B} [\tilde{A}(s) e^{st}] + A_c(t) \quad (4.50)$$

where the residue may be computed as

$$\begin{aligned} \text{Res}_{-i\omega_B} [\tilde{A}(s) e^{st}] &= \left. \frac{e^{st}}{\partial_s(s + i\Delta + \tilde{G}(s))} \right|_{s=-i\omega_B} \\ &= \left(1 + \partial_s \tilde{G}(s) \Big|_{s=-i\omega_B} \right)^{-1} e^{-i\omega_B t} \\ &= c_B e^{-i\omega_B t} \end{aligned} \quad (4.51)$$

justifying the preceding claim that solutions $s = -i\omega_B$ correspond to non-decaying exponential terms in the excited state population. Hence (4.50) takes the form

$$A(t) = c_B e^{-i\omega_B t} + A_c(t) \quad (4.52)$$

The term $A_c(t)$ is the complement of our non-decaying solution. We are not interested in its precise details here, though we will note that in the present model, it decays to zero as $t \rightarrow \infty$, since there will only be one such solution $s = -i\omega_B$. In principle, if there were more such solutions, then we could separate out each such solution using the residue theorem and leave behind $A_c'(t)$ which tends to zero as described.

The result from (4.52) is directly inserted into the equation for $\tilde{B}_\omega(s)$ and, defining $\tilde{\gamma}(s) = (s + i\omega)^{-1}$, using the convolution property of Laplace trans-

forms to solve for $B_\omega(t)$:

$$\begin{aligned}\tilde{B}_\omega(s) &= -i\gamma^*(\omega)\tilde{A}(s)\tilde{\gamma}(s) \\ \Rightarrow B_\omega(t) &= -i\gamma^*(\omega)\int_0^t \gamma(t-\tau)A(\tau)d\tau\end{aligned}\quad (4.53)$$

The convolution in (4.53) can be evaluated

$$\begin{aligned}B_\omega(t) &= -i\gamma^*(\omega)\int_0^t e^{-i\omega(t-\tau)}(c_B e^{-i\omega_B \tau} + A_c(t))d\tau \\ &= \frac{-i\gamma^*(\omega)ic_B(e^{-i\omega t} - e^{-i\omega_B t})}{\omega - \omega_B} + B'_{\omega,c}(t) \\ &= \frac{-\gamma^*(\omega)c_B e^{-i\omega_B t}}{\omega - \omega_B} + B_{\omega,c}(t)\end{aligned}\quad (4.54)$$

where $B_{\omega,c}(t)$ is again the complementary piece to our non-decaying solution whose precise form is irrelevant. Again, the exact form of $B_{\omega,c}(t)$ has no closed form. Now, combining (4.52) and (4.54) into the state expansion for the system yields the state

$$\begin{aligned}|\Psi(t)\rangle &= A(t)|1_a, \{0\}\rangle + \int_0^\infty B_\omega(t)\rho(\omega)|0_a, 1_\omega\rangle d\omega \\ &= c_B e^{-i\omega_B t}|1_a, \{0\}\rangle + A_c(t)|1_a, \{0\}\rangle \\ &\quad - c_B e^{-i\omega_B t} \int_0^\infty \frac{\gamma^*(\omega)}{\omega - \omega_B} \rho(\omega)|0_a, 1_\omega\rangle d\omega \\ &\quad + \int_0^\infty B_{\omega,c}(t)\rho(\omega)|0_a, 1_\omega\rangle d\omega \\ &= |\psi_B\rangle e^{-i\omega_B t} + |\Psi_c(t)\rangle\end{aligned}\quad (4.55)$$

with

$$|\psi_B\rangle = c_B \left(|1_a, \{0\}\rangle - \int_0^\infty \frac{g^*(\omega)}{\omega - \omega_B} \rho(\omega)|0_a, 1_\omega\rangle d\omega \right)\quad (4.56)$$

and

$$|\Psi_c(t)\rangle = A_c(t)|1_a, \{0\}\rangle + \int_0^\infty B_{\omega,c}(t)\rho(\omega)|0_a, 1_\omega\rangle d\omega\quad (4.57)$$

The state $|\psi_B\rangle$ has no time dependence outside of the phase $e^{-i\omega_B t}$, which we now identify with the energy of the bound state, $\hbar\omega_B$. The first term in eq. (4.56) corresponds to the excited state of the lattice well, whereas the second term yields an evanescent matter-wave cloud, including the ground state of

the well. The state $|\Psi_c(t)\rangle$ satisfies,

$$|\Psi_c(t)|^2 = 1 - c_B \quad (4.58)$$

because $|\psi_B|^2 = c_B$. Since c_B is the probability to remain bound, the interpretation of $|\Psi_c(t)\rangle$ becomes clear. It represents the atomic population in the well that is released into propagating modes and does not return in time. The existence of this term is understandable if one considers that a sudden turn-on of the coupling at $t = 0$, as in the preceding treatment, represents a transient, resonant coupling to many different momentum modes. (This effect vanishes if the coupling is turned on adiabatically.)

The above described state (4.56) is manifestly a bound state of emitted matter waves “stuck” to the emitter. This is in direct analogy to the so-called *atom-photon bound state* in PBG materials [97, 153, 158–161] as a “dynamic state in a superposition of the excited and ground states with an admixture of a photon “cloud”, which surrounds the atom”[97]. They are of experimental interest as, for example, mediators of tunneling beyond the nearest neighbor in lattice models and for the engineering of resonant dipole-dipole interactions between emitters.

Returning now to the question of when such a bound state exists, we recall that we are looking for purely imaginary roots of the denominator of (4.46). In other words, we are seeking to solve the defining equation [153]

$$-i\omega_B + i\Delta + \tilde{G}(-i\omega_B) = 0 \quad (4.59)$$

Now, if we recall (4.49), we can integrate (4.59) and arrive at the transcendental equation

$$\omega_B = \Delta - \sqrt{\frac{\pi}{2}}\delta_L \sqrt{\frac{\omega_0}{|\omega_B|}} \exp\left(\frac{2|\omega_B|}{\omega_0}\right) \text{Erfc}\left(\sqrt{\frac{2|\omega_B|}{\omega_0}}\right) \quad (4.60)$$

with Erfc again the complimentary error function. The assumption of strong lattice confinement, ω_0 being much larger than any other frequency scale in the problem, allows for the Taylor expansion of this result, and keeping the leading order term $\propto \sqrt{\omega_0/\omega_B}$ and the sub-leading order term which does not depend on ω_B , results in

$$\omega_B = (\Delta - \delta_L) - \frac{iD}{\sqrt{\omega_B}} \quad (4.61)$$

Comparison with the denominator in eq.(4.25) reveals this to be the same

form upon rotating $s = -i\omega_B$. Thus the dynamical equations in sec. 4.3.2 have been recovered in a slightly different formalism.

The notable feature of this state is that it is made up of contributions from all possible emitted matter waves, but they evolve with a fixed phase ω_B rather than according to their own dynamical phases. If we focus on the emitted wave part of (4.56) only, then we find the following expression for the bound state wave function

$$\psi_B^{mw}(x) = c_B^{1/2} \int_0^\infty \frac{\gamma^*(\omega)}{\omega - \omega_B} \rho(\omega) \langle x | 0_a, 1_\omega \rangle d\omega \quad (4.62)$$

The matter-wave of eq. (4.62) contains contributions from all possible eigenstates $\langle x | 0, 1_\omega \rangle$ with frequency ω . Using $k(\omega) = \sqrt{2m\omega/\hbar}$, the eigenstates are $\varphi_\omega(x) = \langle x | 0_a, 1_\omega \rangle \propto \cos[k(\omega)x]$. In this way, the spatial profile of the wave can be constructed by solving for ω_B given at fixed detuning, and then computing (4.62), c.f. fig. 4.4A.

As is particularly apparent from fig. 4.4A, $\psi_B(x)$ is exponentially localized. Note that the decay is different from the 3D case, where a Yukawa-type profile is seen to arise away from the center of the bound state [112]. Fitting an exponential to the wings of the computed states and extracting this decay for a large range of negative detunings allows for a comparison of the decay length to an evanescent-wave model of the form

$$\xi = a_{ho} \sqrt{\frac{\omega_0}{2|\tilde{\Delta}|}} \quad (4.63)$$

The resulting fit decay lengths are shown in fig. 4.4B (red circles) [We plot three sample curves in units of $d_0 = \lambda_{latt}/2$ with $\lambda_{latt} = 790.4$ nm the lattice wavelength as the characteristic length scale of the problem. We do so looking ahead to the experimental implementation, c.f. 5 and [91].] It should be noted that eq. (4.63) matches the expectation in which one naively assumes a matter wave with negative energy and a corresponding imaginary wave-vector κ set by the detuning only for large negative detunings $\tilde{\Delta}$. To properly capture the physics of the system, $\hbar\omega_B$, the bound state energy must be used instead of the detuning, with the associated characteristic length

$$\xi = a_{ho} \sqrt{\frac{\omega_0}{2|\omega_B(\Delta)|}} \quad (4.64)$$

To determine $\omega_B(\Delta)$, the soft cutoff in the integral in eq.(4.48), $\exp(-2\omega/\omega_0)$ can be approximated by a sharp cutoff of the integral at $\omega \approx \omega_0$. Expanding the integrand to leading order in the, assumed small, quantity ω/ω_0 and inte-

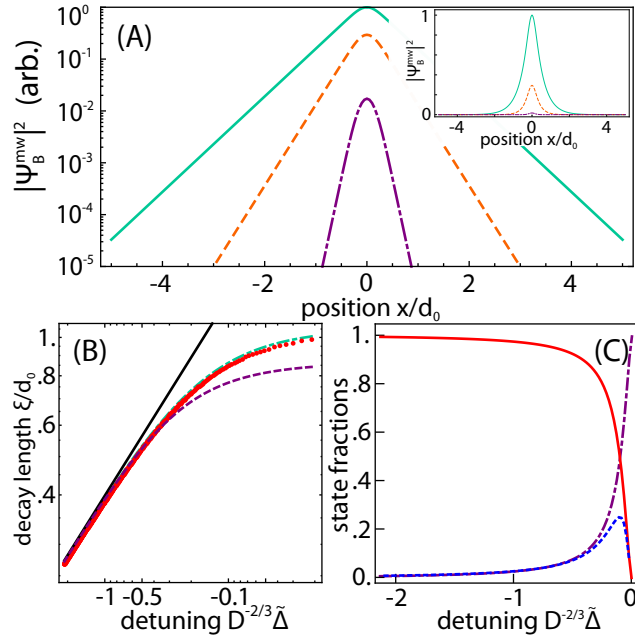


Figure 4.4: Characteristics of the evanescent matter-wave. (A) Density distribution as a function of distance in lattice spacings $d_0 = \lambda_{latt}/2$ for $\tilde{\Delta}/\tilde{\Omega} = -27$ (purple, dot-dashed), -2.7 (orange, dashed), and -0.27 (green, solid). (B) Extracted decay length in lattice spacings as a function of the detuning (red dots). The slope of the black line is $-1/2$ (after reversing the horizontal axes), the scaling expected in 1D for large detunings. The purple (dotted) curve is the model based on eq. 4.65, and the green (dot-dashed) curve is a more sophisticated model (see text). (C) The relative populations of the well (i.e. excited state of the well) (red, solid), and the evanescent matter wave (blue, dashed) as a function of detuning. We also depict the population that is radiated away (purple, dot-dashed).

grating, leads to an effectively quadratic equation for ω_B . This equation has a non-trivial negative root

$$\omega_B = \frac{\Delta}{2} + \frac{1}{2}\sqrt{\Delta^2 + \Xi\Omega^2} \quad (4.65)$$

which for small Ω coincides with the set detuning from the edge of the continuum. The second term has the form of a generalized Rabi frequency $\sqrt{\Delta^2 + \Xi\Omega^2}$ (Ξ is a numerical prefactor of order 1), and suggests that for intermediate detunings, the correction to the decay length is due to an AC Stark shift induced by the coupling (note that it is independent of the lattice

potential). This expression (4.64) with (4.65), however, underestimates the decay length for small detunings, c.f. fig. 4.4B (purple, dotted). In order to recover the proper behavior in this limit, eq. (4.60) must be solved. For the regimes of validity of this work, this amounts to solving eq. (4.61), an effectively *cubic* equation for the bound state energy, whose real root, when inserted into eq. (4.64), gives the true decay length of the system. This curve is also shown in fig. 4.4B (green, dot-dashed), giving much better agreement with the fit decay lengths.

As a final consideration of this dynamically bound state, we further analyze the internal-state composition of the state $|\psi_B\rangle$. The constant, c_B , which depends on the bound state energy $\hbar\omega_B$, has the full form

$$c_B = \left\{ 1 + \frac{\delta_L}{\sqrt{2\pi}\omega_0} \frac{\exp(2|\nu_B|)}{2|\nu_B|^{3/2}} \left[2\exp(-2|\nu_B|)\sqrt{2\pi|\nu_B|} + \pi(1 - 4|\nu_B|)\text{Erfc}\left(\sqrt{2|\nu_B|}\right) \right] \right\}^{-1} \quad (4.66)$$

where the parameter ν_B is defined to be ω_B/ω_0 . This constant gives the probability amplitude to measure the system in the lattice-well atomic matter-wave bound state, which as noted, is a superposition of the excited occupational spin state and the evanescent wave. The probability to measure the atom in the bound state, starts at 0 for a detuning of δ_L and then increases monotonically with decreasing detuning before saturating at a value of 1, c.f. fig. 4.4C (red, solid).

The relative proportion of the free space modes which make up the evanescent wave in $|\psi_B\rangle$ initially rises with increasing (negative) detuning before reaching a maximum and then dropping off to essentially zero (blue, dotted curve in fig. 4.4C). For larger and larger negative values of the detuning, the bound state energy $\hbar\omega_B$ sinks farther and farther below the continuum boundary, and in this regime, it is impossible for the free-particle modes to participate in the formation of the bound state in a significant way, leading to the above-noted drop-off behavior.

4.4 Emission near a band with two edges

We recall that our motivation for studying spontaneous emission of matter waves was as a simulator for the behavior of an atom emitting a photon into a photonic band gap material. However, our previous model considering emission of freely propagating matter waves is an approximation, i.e. near the bottom of a band, we can take the quadratic approximation,

$\varepsilon(k)/\hbar \approx \hbar k^2/2m^*$, and treat the case of essentially massive photons of effective mass m^* . However, real photonic band gap materials feature a band structure, so it becomes reasonable to ask whether we can refine our treatment to consider a band structure. Remarkably, one can make progress for a variety of band structures and lattice geometries, and this is still an area of active theoretical research today [115, 117, 118]. Here, we consider the case of a 1-dimensional sinusoidal energy band. We will see that the new singularities in the density of states (at the upper and lower band edges) introduce quantitative differences with the single edge case in section 4.3. Specifically, we will find even stronger non-Markovianity resulting in persistent oscillations for long time, which we understand to be a beating between *two* bound states now supported by the system. The theoretical approach in this section is largely inspired by the resolvent operator approach of [117] who considers emission into a 1D sinusoidal band, but we feel that it considers regimes which are heretofore unexplored and makes satisfying connections with well-known atomic physics results.

4.4.1 Solution for emission into a 1D band

Our starting point is to consider the simplified single-emitter Hamiltonian for spontaneous emission as in [91, 114]. Specifically, we consider $\hat{H} = \hat{H}_r + \hat{H}_b + \hat{H}_{int}$ with $\hat{H}_r = \Delta\sigma_{ee}$ and $\hat{H}_b = \sum_q \omega(q)\hat{b}_q^\dagger\hat{q}$ and the interaction Hamiltonian is

$$\hat{H}_{int} = g \sum_q \hat{b}_q \sigma_{eg} + \text{H.c.} \quad (4.67)$$

Note that we are now working in a frame where the excited state energy of our single-emitter is Δ , and we will use the terms detuning and excited state energy interchangeably throughout what follows. We also have introduced the nomenclature “red” for our emitter state and “blue” for our emitted matter wave states with an eye towards the experimental implementation described in [91] and section 5.3.

This model differs from section 4.3 in two ways: first, we take for our emitted matter-wave (henceforth “blue”) states the Bloch waves of an optical lattice having bandwidth $4J$ and dispersion $\omega(q) = -2J \cos(qd)$, where $d = \lambda/2$ (which is equivalent to having a state dependent lattice for both the emitter (henceforth “red”) *and* blue atoms, albeit with different depths), and second, following [115], we assume that all of these modes are coupled to equally with strength $g = \hbar\Omega/2$. (This approximation holds when the lattice for the red state is much deeper than other energy scales in the problem, so the momentum width of the initial emitter excited state is very large. This is

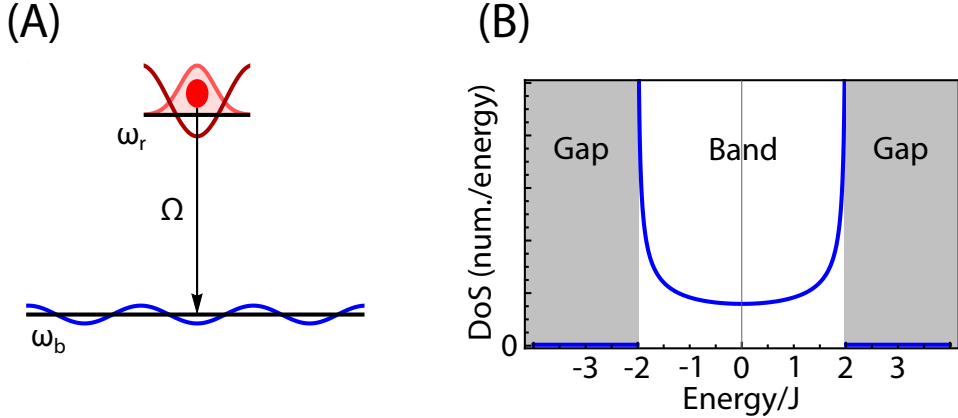


Figure 4.5: Cartoon displaying the scheme for emission into a band structure. (A) Red $|r\rangle$ atoms are confined to the wells of a deep, state-selective optical lattice potential, coupled to blue $|b\rangle$ atoms (different internal states) which only feels a shallow optical potential. (Cartoon shows a Wannier interpretation for both states, but in the model, we will treat the $|b\rangle$ states in a Bloch wave formalism.) (B) Schematic of the density of states in the tight-binding limit for the $|b\rangle$ atoms. In this case, there are *two* divergences in the density of states, resulting in a richer physics compared to the single edge case.

the same as the strong confinement approximation made in section 4.3.)

As before, we take for our state ansatz

$$|\psi(t)\rangle = C_r(t) |e_r, 0_b\rangle + \sum_q C_q(t) |g_r, 1_q\rangle \quad (4.68)$$

subject to the initial condition that $C_r(0) = 1$ and $C_q(0) = 0$. Substitution into the Schrödinger equation yields the coupled set of differential equations

$$\dot{C}_r = -i\Delta C_r - ig \sum_q C_q \quad (4.69)$$

$$\dot{C}_q = -i\omega(q)C_q - igC_r \quad (4.70)$$

We can now make a rotating frame transformation in the expansion coefficients to simplify the equations of motion by taking $A_r = C_r e^{i\Delta t}$ and $A_q = C_q e^{i\omega(q)t}$.

In such a case, equations (4.71) and (4.70) reduce to

$$\dot{A}_r = -ig \sum_q A_q e^{-i\Delta_q t} \quad (4.71)$$

$$\dot{A}_q = -ig A_r e^{i\Delta_q t} \quad (4.72)$$

where we have introduced $\Delta_q = \omega(q) - \Delta$. These two equations (4.71) and (4.72) have manifestly the same structure as (4.11) and (4.12). We therefore can solve the equations of motion in the same way.

Equation (4.72) may be formally integrated in time and substituted into (4.71), and the sum over quasimomentum q in the resulting equation may be traded for an integral. After integration over quasimomentum, the equation of motion for $A_r(t)$ takes the by now expected convolution form

$$\dot{A}_r(t) = - \int_0^t A_r(t') G_{latt}(t-t') dt' \quad (4.73)$$

where we have introduced the bath memory function

$$G_{latt}(\tau) = g^2 e^{i\Delta\tau} J_0(2J\tau) \quad (4.74)$$

where $J_0(x)$ is a Bessel function of the first kind.

We proceed as in 4.3.2 and note that the Laplace transform of (4.73) subject to the initial condition $A_r(0) = 1$ is analogous to (4.20)

$$\tilde{A}_r(s) = \frac{1}{s + \tilde{G}_{latt}(s)} \quad (4.75)$$

with

$$\tilde{G}_{latt}(s) = \frac{g^2}{\sqrt{(s-i\Delta)^2 + 4J^2}} \quad (4.76)$$

The inversion of this Laplace transform can be performed using the standard Bromwich contour method

$$\begin{aligned} e^{-i\Delta t} A_r(t) &= \frac{1}{2\pi i} \int_{\epsilon-i\infty}^{\epsilon+i\infty} ds \tilde{A}_r(s + i\Delta) e^{st} \\ C_r(t) &= \frac{1}{2\pi i} \int_{\epsilon-i\infty}^{\epsilon+i\infty} \frac{e^{st} ds}{s + i\Delta + g^2/\sqrt{4J^2 + s^2}} \end{aligned} \quad (4.77)$$

Since $e^{-i\Delta t} A_r(t) = C_r(t)$, we can return to working with $C_r(t)$. Next, we rotate variables $s = iz$, essentially changing a Laplace transform into a Fourier

transform, whence (4.77) becomes

$$C_r(t) = \frac{1}{2\pi i} \int_{-\infty}^{\infty} dz \frac{e^{-izt}}{z - \Delta + \Sigma_1(z)} \quad (4.78)$$

where we have introduced the self-energy $\Sigma_1(z)$:

$$\Sigma_1(s) = \frac{g^2}{2\pi} \int_{BZ} \frac{dq}{z - \omega(q)} = \frac{g^2}{\sqrt{z^2 - 4J^2}} \quad (4.79)$$

The self energy, well known in the context of condensed matter systems [162], captures the influence of the environment acting back on the single emitter. We note that the self energy and the Laplace transform of the bath correlation function are related to each other by a shift and rotation:

$$\Sigma_1(z) = i\tilde{G}_{latt}(-iz + i\Delta) \quad (4.80)$$

At this point, we note that the definition of our self energy (4.79) matches that of [115], and furthermore that our approach starting from the Schrödinger equation eventually matches the approach of the authors of [115] starting from the resolvent operator, up to a minus sign in the denominator of (4.78) whose origin we have thus far been unable to determine. As such, we follow their approach for the calculation of the Fourier integral. The integrand contains two branch cuts running parallel to the negative imaginary axis located at $z = \pm 2J$, and we must therefore analytically continue it into the region $|\text{Re}(z)| \leq 2J$ by making the substitution $\sqrt{z^2 - 4J^2} \rightarrow -\sqrt{z^2 - 4J^2}$. Note that there are three types of contribution [115] to the time evolution:

- *Bound states*: These arise from real poles of (4.78), and they yield non-zero population in the excited state at long times. They physically correspond to bound states of matter waves evanescently localized to the atomic emitter. (Note that in section 4.3.5, the bound states corresponded to purely imaginary solutions. In rotating from a Laplace to a Fourier picture, the real and imaginary axes have switched roles, whence now real poles yield bound states.) There will in general be two such poles, corresponding to a bound state in the band gaps both below and above the band. Their energies/frequencies are given as the solutions to

$$z - \Delta = \text{Re}(\Sigma_e(z)) \quad (4.81)$$

which is quite complicated in general. We will deal with explicit expressions for it shortly.

- *Unstable pole:* This pole has a negative imaginary part, and as such, it corresponds to an oscillatory excitation which decays over time. In general, there will be one such pole solution, and it will occur in the analytically continued region.
- *Branch cut detours:* In order to close the Laplace inversion contour, it becomes necessary to go around branch cuts at nonanalytic points of the band. These contributions must be carefully computed by analytically continuing onto the correct Riemann sheet and integrating. However, they are all transient and eventually decay with time.

Armed with this knowledge and the residue theorem, we define a few terms and then schematically represent the excited state population as a function of time. First, let the upper (lower) bound state frequencies (energies/ \hbar) be denoted by ω^\pm . These are two purely real frequencies. Next, denote the frequency of the unstable pole contribution by $\tilde{\omega} = \omega_{UP} + i\Gamma_{UP}/2$ where here Γ_{UP} is a negative real number representing the decay rate of the excitation. Also, denote by R^\pm and R_{UP} the complex residues at these poles. Lastly, denote by the function $\Phi_{BC}(t)$ all of the contributions from the branch cut detours. then the time evolution of an emitter starting in its excited state is

$$C_r(t) = R^+ e^{-i\omega^+ t} + R^- e^{-i\omega^- t} + R_{UP} e^{(i\omega_{UP} - |\Gamma_{UP}|/2)t} + \Phi_{BC}(t) \quad (4.82)$$

In principle, (4.82) represents everything that we need to know about the system under consideration.

We can determine ω^\pm by solving the following polynomial equation (which is equivalent to (4.81)):

$$\frac{1}{g^4} (z^4 - 2\Delta z^3 + (\Delta^2 - 4J^2)z^2 + 8J^2\Delta z - 4J^2\Delta^2) = 1 \quad (4.83)$$

whose real roots for $|\text{Re}(z)| > 2J$ determine the bound state energies. The complex root of (4.81) having negative imaginary part is $\tilde{\omega}$. We note that as (4.81) is a quartic polynomial, there is another root, conjugate to $\tilde{\omega}$ with positive imaginary part. However, this root lies outside the integration contour, and thus does not contribute to the time evolution. The algebraic solution to (4.81) is quite complicated, and it does not grant us much physical intuition. However, we note that it may be solved numerically for any chosen set of parameters efficiently using modern numerical methods. The residues which correspond to these poles may be computed as follows:

$$\text{Res}_G(z_0) = \frac{1}{\partial(z - \Delta + \Sigma_1(z))|_{z=z_0}} = \left(1 + \frac{g^2 z_0}{(z_0^2 - 4J^2)^{3/2}}\right)^{-1} \quad (4.84)$$

where here, z_0 may be any of ω^\pm or $\tilde{\omega}$, and due to the analytic continuation, the second term in parentheses in (4.84) takes a minus sign for $\tilde{\omega}$. Furthermore, with a little bit of effort, we may write down an explicit form for the branch cut detour contribution $\Phi_{BC}(t)$. We do not give its explicit form here, and instead reference equation (10) in [118]. The important fact to note is that for long times t , the integrands both vanish, and thus the contributions from the branch cuts are incoherent, decaying behavior. We will later use this fact that $\lim_{t \rightarrow \infty} \Phi_{BC}(t) = 0$. With equations (4.83), (4.84), and (10) from [118], we may numerically solve (4.82) for any range of parameters in which we are interested. As an example, consider the different behaviors displayed in fig. 4.6, which displays nearly Markovian behavior across a whole band for weak coupling (A) and strongly non-Markovian behavior across the band for strong coupling (B). In particular, for large bandwidths, where the coupling to the edges in the density of levels is weak, we recover largely the Markovian decay observed for large detunings in [91]. The other, more exotic effects displayed in fig. 4.6 are the domain of the next sections.

4.4.2 Bound state oscillations

In numerically solving (4.82) for certain ranges of parameters, we observe behavior in which the excited state population decays to zero before rising back up to some finite value and oscillating between this value and zero for all observed times t thereafter, c.f. fig. 4.7.

These long-lived oscillations can be interpreted as a beat between the two bound states (above and below the band). We may demonstrate this as follows: Consider the last two contributions in (4.82). We have already indicated that $\lim_{t \rightarrow \infty} \Phi_{BC}(t) = 0$. Furthermore, “by inspection”, we may observe that $\lim_{t \rightarrow \infty} R_{UP} e^{(i\omega - |\Gamma_{UP}|)t} = 0$. Therefore, at late times, (4.82) becomes

$$C_r(t \rightarrow \infty) = R^+ e^{-i\omega^+ t} + R^- e^{-i\omega^- t} \quad (4.85)$$

and thus the observable excited state population is the absolute square:

$$|C_r(t)|^2 = |R^+|^2 + |R^-|^2 + 2\text{Re}(R^+ R^-) \cos((\omega^+ - \omega^-)t) \quad (4.86)$$

In other words, it is apparent from (4.86) that the population in the excited state at long times oscillates with a certain amplitude $2\text{Re}(R^+ R^-)$ around some “mean value” $|R^+|^2 + |R^-|^2$ at a frequency corresponding to the differences in genergy between the two bound states $\omega^+ - \omega^-$.

The relative size of the residue terms determines how pronounced this effect is, and as such, considerations of the residues can determine where in

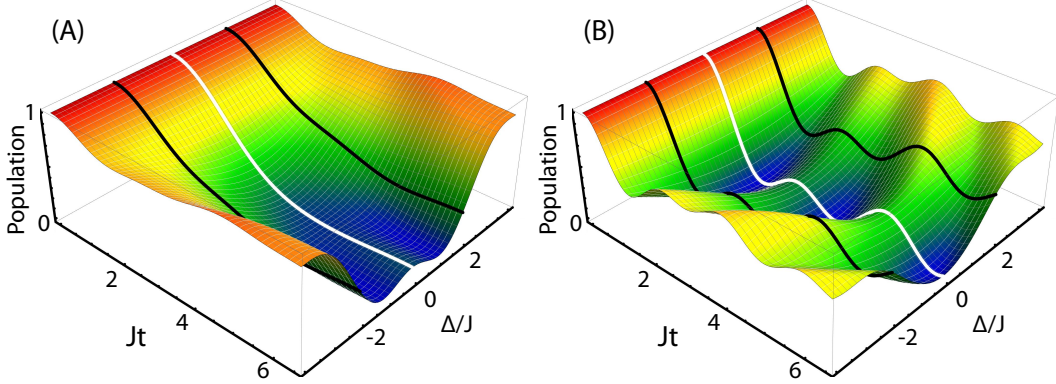


Figure 4.6: Transition from nearly Markovian decay to Rabi-like oscillation. Here we present the results of time evolution of the excited ($|r\rangle$) population as a function of time for and detuning with a coupling strength of (A) $g = 2\pi \times 0.43 \text{ kHz}/2$ and (B) $g = 2\pi \times 1 \text{ kHz}/2$ and bandwidth $J = 2\pi \times 0.45 \text{ kHz}$. In (A), the decay approaches Markovian exponential decay for a range of parameters within the band, only displaying significant oscillatory behavior outside the band. In (B), the coupling strength and bandwidth are comparable, and a more exotic set of behaviors is predicted. The decay is not Markovian anywhere within the band, instead displaying a partial decay and oscillatory behavior for all detunings. As we demonstrated in 4.4.2, this behavior is a consequence of two bound states beating strongly for the chosen parameters. Note also that at the level of a single band model, the time evolution behavior is symmetric around the band center $\Delta = 0$. This results from the assumption of a sinusoidal band.

parameter space we hope to observe such oscillations. We note that similar behavior was considered for an array of coupled cavities [163] and in slow-light waveguide-QED [164].

Furthermore, as a test of this prediction, we have numerically evaluated the long-time behavior of the excited state population dynamics for varying tunneling frequencies J (bandwidths $4J$) at zero detuning and fit a sinusoid to the results. The fit frequency and amplitude are then compared in 4.8 to the expected bound state frequency difference $\omega^+ - \omega^-$ and predicted oscillation amplitude:

$$(\omega^+ - \omega^-)_{\Delta=0} = 2\sqrt{2J^2 + \sqrt{g^4 + 4J^4}} \quad (4.87)$$

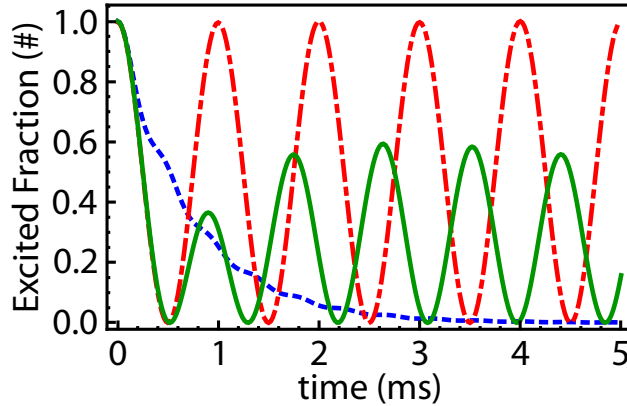


Figure 4.7: Emission dynamics into a band structure. Here we present the results of time evolution of the excited ($|r\rangle$) population as a function of time for 5 ms with a coupling strength of $g = 2\pi \times 1 \text{ kHz}/2$ and various bandwidths (computed in the tight-binding approximation). For bandwidths larger than the coupling strength, here $\approx 4 \text{ kHz}$ (blue, dashed), the decay into the band is approximately a Markovian exponential decay. For bandwidths much less than the coupling, in the figure $\approx 10 \text{ Hz}$ (red, dash-dotted), the behavior exhibits a nearly perfect Rabi oscillation. For intermediate bandwidths approximately the same as the coupling strength, here $\approx 1 \text{ kHz}$ (green, solid), the behavior exhibits first a complete decay of excited state population before a revival settling to a long time oscillation which persists for all future times. These oscillatory effects are discussed in detail in sections 4.4.2 (similar behavior was reported in [163]).

$$\begin{aligned} Amp &= |R^+|^2 + |R^-|^2 + 2\text{Re}(R^+R^-) \\ &= 4 \left(1 + \frac{g^2}{(\sqrt{g^4 + 4J^4} - 2J^2)\sqrt{1 - 4J^2/(2J^2 + \sqrt{g^4 + 4J^4})}} \right)^{-2} \end{aligned} \quad (4.88)$$

The results agree exceptionally well, suggesting that the predicted behavior is indeed physically explained as an oscillation between these two states.

4.4.3 Deep lattice limit

The above observations suggest a connection to well-understood atomic physics, namely, that of a Rabi oscillation. In particular, if the bath lattice becomes very deep, then the tunneling rate in the lattice should tend to zero ($J \rightarrow 0$) as the band gets narrower. In such a limit, one expects Rabi-oscillations between

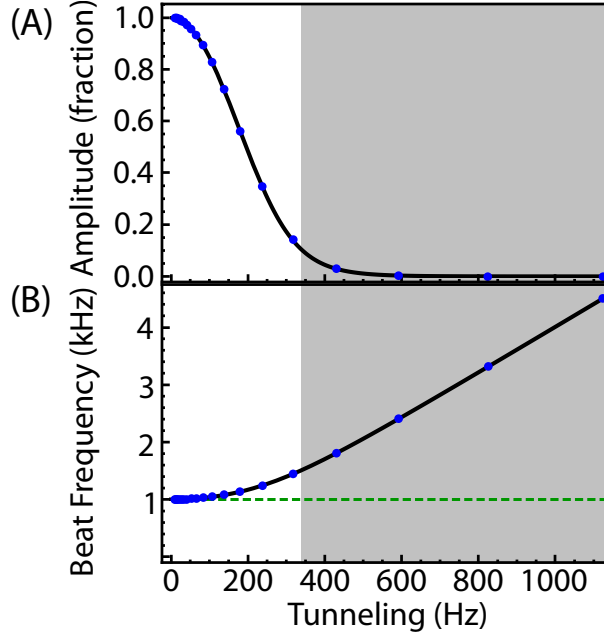


Figure 4.8: Relation between the bandwidth of the emission band and the bound state beat frequency and amplitude at long times for fixed coupling strength $g = 2\pi \times 1 \text{ kHz}/2$ and detuning at the band center: (A) Oscillation amplitude and (B) beat frequency. The dots are data points extracted from a sinusoidal fit to the numerical solution of the equations of motion for long times (15-20 ms) and the solid line is the expectation based on the model. The shaded gray box indicates the region of bandwidths for which the oscillation amplitude is less than 10% of full contrast, for which parameters the behavior e likely not resolvable in an experiment.

the bath and the excited emitter. We now demonstrate that this is, in fact, the behavior that occurs.

We note first that in the case where $J \rightarrow 0$, the bound-state energy defining polynomial (4.83) becomes particularly simple

$$z - \Delta = \frac{g^2}{z} \quad (4.89)$$

or equivalently $z^2 - \Delta z - g^2 = 0$. This quadratic equation may be solved using the quadratic formula, and the roots are found to be

$$\omega^\pm = \frac{1}{2} \left(\Delta \pm \sqrt{\Delta + 4g^2} \right) = \frac{\Delta \pm \tilde{\Omega}}{2} \quad (4.90)$$

where we have introduced the generalized Rabi frequency $\tilde{\Omega}^2 = \Omega^2 + \Delta^2$, as in typical atomic physics applications. For intuition, we first consider the case of resonant coupling, i.e. $\Delta \rightarrow 0$. In this case, we note that the bound state frequencies are just $\omega^\pm = \pm\Omega/2 = \pm g$. The residues may be computed for the zero bandwidth case from

$$\text{Res}_G(z) = \left(1 + \frac{g^2}{z^2}\right)^{-1} \quad (4.91)$$

and thus on resonance, $\omega^\pm = \pm g$, so $R^\pm = 1/2$. We also note that since the band has zero bandwidth in this considered situation, there is no contribution from the branch cuts or from an unstable pole. In such a case, (4.86) becomes exact for all times, and using the values we have computed for the residues, we find

$$p_e(t) = \frac{1}{2} + \frac{1}{2} \cos\left(\left(\frac{\Omega}{2} + \frac{\Omega}{2}\right)t\right) = \cos^2\left(\frac{\Omega}{2}t\right) \quad (4.92)$$

which is exactly the evolution we expect for a Rabi oscillation when the population starts in the excited state. Thus, we have recovered the regular Rabi oscillation as a limit of emission into a deep lattice. We recognize the two bound states in this case as having converged to the dressed states of the internal state evolution.

We next generalize to the case of finite detuning Δ , guided by our intuition from the resonant case. The bound state frequencies are (4.90). The corresponding residues are computable as

$$R^+ = \frac{(\Delta + \tilde{\Omega})^2}{(\Delta + \tilde{\Omega})^2 + \Omega^2}, \quad R^- = \frac{(\Delta - \tilde{\Omega})^2}{(\Delta - \tilde{\Omega})^2 + \Omega^2} \quad (4.93)$$

One may show, after much tedious algebra, using (4.93) that the following hold:

$$|R^+|^2 + |R^-|^2 = \frac{1}{2} \left(1 + \frac{\Delta^2}{\tilde{\Omega}^2}\right), \quad 2\text{Re}(R^+ R^-) = \frac{\Omega^2}{2\tilde{\Omega}^2} \quad (4.94)$$

Thus we find

$$\begin{aligned} p_e(t) &= \frac{1}{2} \left(1 + \frac{\Delta^2}{\tilde{\Omega}^2}\right) + \frac{\Omega^2}{2\tilde{\Omega}^2} \cos\left(\left(\frac{\Delta + \tilde{\Omega} - \Delta + \tilde{\Omega}}{2}\right)t\right) \\ &= \frac{\Delta^2}{\tilde{\Omega}^2} + \frac{\Omega^2}{\tilde{\Omega}^2} \cos^2\left(\frac{\tilde{\Omega}}{2}t\right) \end{aligned} \quad (4.95)$$

We note that this is the well known result for the population of the initial

state in a detuned Rabi oscillation. As a check on our logic, we point out that the (more) well known expression for the population of the state which is not initially populated is recovered by simply taking $1 - p_e(t)$. Specifically,

$$1 - p_e(t) = \frac{\Omega^2}{\tilde{\Omega}^2} \sin^2 \left(\frac{\tilde{\Omega}}{2} t \right) \quad (4.96)$$

which confirms our intuition. A two-state Rabi oscillation arises as the deep-lattice limit of our spontaneous emission system, as physical intuition says it must when the density of levels of the target state becomes delta-like. We note that another way of thinking about this limit of a very deep lattice is to realize that the coupling strength is so much larger than the bandwidth $4J$ that we effectively only couple a single emitter state to a single blue state, roughly corresponding to a cavity-QED limit [96].

4.4.4 Weak-lattice limit

We can also consider the case in which the lattice potential felt by the blue atoms is vanishingly small. In this case, we expect to recover the free-particle results of section 4.3. We shall now demonstrate that this is the case.

We note that for a very weak lattice, or no lattice at all, the assumption of momentum independent coupling g breaks down. Instead, we must consider a momentum dependent coupling $g \rightarrow g_q$. The exact details of this coupling will depend upon the problem at hand. We thus must refine the expression for the 1D self energy in such a case to

$$\Sigma(z) = \frac{1}{2\pi} \int_{BZ} dq \frac{|g_q|^2}{z - \omega(q)} \quad (4.97)$$

For a shallow lattice, $\omega(q) = \omega(k) \approx \hbar k^2/2m^*$, and thus we may write for (4.97)

$$\Sigma(z) = \frac{1}{2\pi} \int_{-\pi/a}^{\pi/a} dk \frac{|g_k|^2}{z - \hbar k^2/2m^*} = \frac{1}{\pi} \int_0^{\pi/a} dk \frac{|g_k|^2}{z - \hbar k^2/2m^*} \quad (4.98)$$

with the second equality following from the evenness of the integrand. We have replaced q with k since in the limit of a vanishing lattice, quasimomentum becomes indistinguishable from usual momentum.

It turns out to be useful to note that for the zero lattice limit, we have reintroduced the units of the lattice spacing a , which we take to zero, thus sending the upper limit of integration in (4.98) to infinity. Next, we introduce

the change of variables from momentum to energy at the cost of introducing a density of states $\rho(\omega)$. Formally, $dk \rightarrow \rho(\omega)d\omega$, and $\omega = \hbar k^2/2m^*$. Thus, the self-energy becomes

$$\Sigma(z) = \int_0^\infty d\omega \frac{|g(\omega)|^2 \rho(\omega)}{z - \omega} = \int_0^\infty d\omega \frac{\mathcal{G}(\omega)}{z - \omega} \quad (4.99)$$

where we have absorbed $1/\pi$ into the definition of $\rho(\omega)$, and where $\mathcal{G}(\omega)$ is defined³ after (4.48) in subsection 4.3.5.

We next note that if we take

$$|g(\omega)|^2 = \frac{\sqrt{\pi}a_{ho}}{L} \frac{\Omega^2}{2} e^{-2\omega/\omega_0}, \quad \rho(\omega) = \frac{L}{\pi} \sqrt{\frac{2m^*}{\hbar\omega}} \quad (4.100)$$

as is the case for a 1D free particle motion coupled to a deeply confining harmonic oscillator well of frequency ω_0 with strength Ω , then we find

$$\begin{aligned} \Sigma(z) &= \frac{1}{\sqrt{2\pi}} \frac{\Omega^2}{\omega_0} \int_0^\infty d\omega \sqrt{\frac{\omega_0}{\omega}} \frac{e^{-2\omega/\omega_0}}{z - \omega} \\ &= \sqrt{\frac{\pi}{2}} \delta_L \frac{1}{\sqrt{-z}} e^{-2z/\omega_0} \text{Erfc}\left(\sqrt{\frac{-2z}{\omega_0}}\right) \end{aligned} \quad (4.101)$$

as a function of a complex frequency z . After appropriately rotating (4.101), we see that it is the same as the last term in (4.60). Therefore, we conclude that in the limit of no lattice, we exactly recover the results and solutions from section 4.3.

4.4.5 Bound states above and below the band

In addition to examining the time dynamics across the various limits of bandwidth and coupling strength, we can also study the bound states whose existence is indicated by the poles in the Laplace transforms of (4.69) and (4.70). In particular, a purely imaginary pole in the Laplace transform $s_B = -i\omega_B$ (corresponding to a purely real pole in the Fourier transform inversion integral (4.78), c.f. discussion in 4.4.1) yields a non-decaying bound state. For

³N.B.: it is NOT the Green's function of the resolvent operator approach in [115].

completeness, the Laplace transforms of $C_r(t)$ and $C_k(t)$ are

$$\tilde{C}_r(s) = \frac{1}{s + i\Delta + \Sigma_e(z)} \quad (4.102)$$

$$\tilde{C}_k(s) = \frac{-ig\tilde{C}_r(s)}{s - i\omega(k)} \quad (4.103)$$

Following the same procedure as in section 4.3.5, one can show that the pole s_B corresponds to a bound state having the structure

$$|\Psi_B\rangle = |e_r, vac_q\rangle - \frac{g}{2\pi} \int_{-\pi}^{\pi} \frac{dq}{\omega(q) - \omega_B} |g_r, 1_q\rangle \quad (4.104)$$

which has the same structure as encountered previously (up to a q independent coupling constant g and a differing dispersion relation $\omega(q)$), when we make a switch to a frequency representation rather than a momentum representation. For computational purposes, it is sufficient to work in momentum. The spatial structure of the shallow lattice contribution to (4.104) is revealed by taking the product with $\langle x|$, and we find

$$\psi_{B,mw}(x) = \frac{-g}{2\pi} \int_{-\pi}^{\pi} \frac{\psi_q(x) dq}{\omega(q) - \omega_B} \quad (4.105)$$

where we have tacitly chosen units in which $q_{rec} = 1$ and $\psi_q(x)$ is now the *Bloch wave* corresponding to quasimomentum q in the band structure. As such, we expect the bound states (4.105) to reflect the periodicity of the underlying lattice. The first difference to note from the case of free momentum waves is that there are two bound states corresponding to a pole above and below the upper and lower edges of the band respectively.

Functionally, we can compute the Bloch waves $\psi_q(x)$ numerically by exact diagonalization for a number of discrete quasimomentum values q and then compute the spatial distribution (4.105) to any desired degree of numerical accuracy. The results for various lattice depths and detunings are considered in fig. 4.9. We note that the bound states below the band exhibit a sort of plateau into the neighboring wells, and the state above the band shows a sharp modulation with a revival on the neighboring sites. We understand this to be the result of the fact that below the band, the bound state is coupled most strongly to the $q/q_{rec} = 0$ Bloch waves, whereas above the band, it is coupled most strongly to $q/q_{rec} = \pm 1$. Indeed, a naïve Fourier transform of (4.105)

$$\varphi_B(k) = \frac{1}{\sqrt{2\pi}} \int_{-\infty}^{\infty} e^{-ikx} \psi_{B,mw}(x) \quad (4.106)$$

shows that below the band, the momentum is most strongly concentrated at $k/q_{rec} = 0$ and above the band, this momentum decomposition is doubly peaked near $k/q_{rec} = \pm 1$, c.f. fig. 4.9.

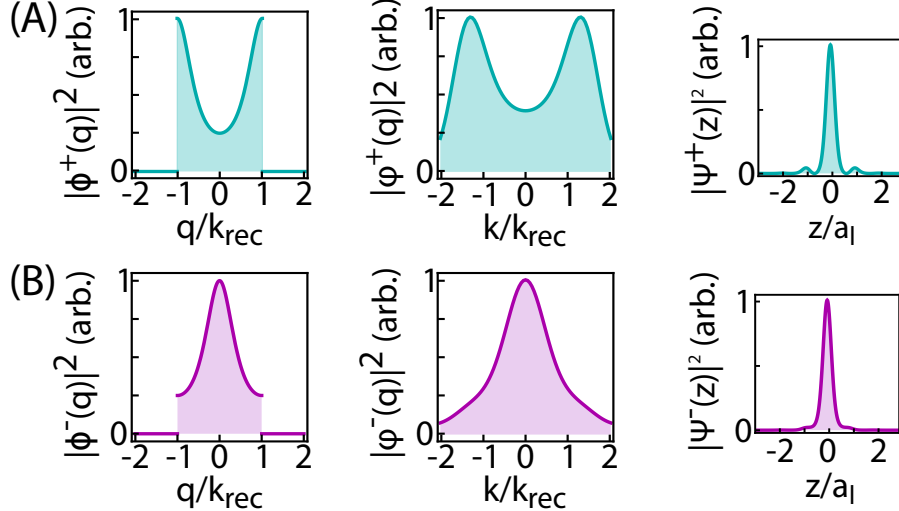


Figure 4.9: Computed momentum space ($|\phi_B(q)|^2$ and $|\varphi_B(k)|^2$) and position space ($|\psi_B(z)|^2$) wavefunctions for representative bound states above (A) and below (B) the single band. The representative bound states are computed for $\omega_B^\pm = \pm 6J$, i.e. one bandwidth away from the band edges. The bound state above the band displays a maximum quasimomentum composition around $q = \pm q_{rec}$, and the bound state below the band is maximally populated by $q = 0$. Note that compared to $\phi_B(q)$, $\varphi_B(k)$ extends out of the first Brillouin zone. The position space wavefunctions are modulated at the periodicity of the lattice, potentially resulting in observable effects in an experiment.

We note that the Fourier transform is a decomposition into plane waves, but it is also natural to ask what is the contribution of each Bloch wave to the state $\psi_{B,mw}(x)$. Indeed, we can compute the elements of a ‘‘Bloch’’ series, since the Bloch waves form a complete basis, i.e.

$$\int_{-\pi/d_0}^{\pi/d_0} \psi_p^*(x) \psi_q(x) dx = \delta(p - q) \quad (4.107)$$

The resulting ‘‘Bloch’’ series coefficients $\varphi_B(p)$, defined by

$$\phi_B(p) = \int_{-\infty}^{\infty} \psi_p^*(x) \psi_{B,mw}(x) dx \quad (4.108)$$

indicate how much of a contribution each Bloch wave, equivalently quasimomentm, makes to the bound state. We can compute this decomposition $\phi_B(q)$ “by inspection” from (4.105), whereupon we find

$$\phi_B(q) = \frac{g}{2\pi} \frac{1}{\omega_B - \omega(q)} \quad (4.109)$$

The results are shown in fig. 4.9. We note that for the case under consideration, in which $\omega(q)$ is a single sinusoidal band that there are two possibilities for the shape of $\phi_B(q)$. In particular, for ω_B below the band, the denominator of (4.109) is largest for $q/q_{rec} = 0$, whereas for ω_B above the band, the the quasimomentum distribution is largest for $q/q_{rec} = \pm 1$, confirming our understanding of the distributions based on the simple Fourier transform. It is further interesting to note that for $\omega_B^+ = -\omega_B^-$ (i.e. if we choose bound states located symmetrically around the band) the corresponding distributions (4.109) can be obtained from each other by shifting all quasimomenta by half of the Brillouin zone. This exact symmetry will be lost if we consider non-sinusoidal bands or multiple bands.

The difference between the momentum and quasimomentum decompositions (or, in practice, their absolute squares, $|\phi_B(k)|^2$ and $|\varphi_B(q)|^2$) is not just a question of academic interest, for in an experiment, we may access both the momentum distribution of the matter wave component, as well as the quasimomentum distribution via a band map procedure. We shall discuss this further in section 5.3.

4.5 Concluding remarks

In this section, we have explored in detail spontaneous emission behavior of an atom trapped in a well of a deep optical lattice with variable coupling to free space and to shallow lattice. The boundaries strongly modify the decay of the population in the lattice well, which displays crossovers from Markovian to non-Markovian dynamics. For free space emission, the emitted matter-wave spectrum at positive detunings is matched well by a simple model for freely-propagating massive particles, and the evanescent wave state formed for negative detunings decays exponentially away from the well. For emission into a band structure, we expect an even stronger Markov to non-Markov crossover, as well as the presence of multiple bound states strongly modified by the lattice periodicity.

Chapter 5

Experiments on spontaneous emission of matter waves into a tunable band structure

This chapter discusses experimental results partly based on our publication *Spontaneous emission of matter waves from a tunable open quantum system*, Ludwig Krinner, Michael Stewart, Arturo Pazmiño, Joonhyuk Kwon, Dominik Schneble, *Nature*, **559**, 589 (2018) [91] (sections 5.1 and 5.2) and partly based on our preprint *Fractional decay of matter-wave quantum emitters in a synthetic bandgap material*, Michael Stewart, Joonhyuk Kwon, Alfonso Lanuza, Dominik Schneble, arXiv:2003.02816 (2020) [149] (sections 5.1 and 5.3).

5.1 Experimental tools and techniques

Experiments in our lab are performed utilizing a moving-magnetic coil transporter apparatus to create Bose-Einstein condensates of Rubidium-87 [120]. Starting from a Magneto-Optical Trap (MOT) of $\approx 1 \times 10^9$ ^{87}Rb atoms, we produce BECs having 1×10^3 atoms up to 2×10^5 atoms (depending on the specifics of the experiment) with a duty cycle of approximately 20 seconds. Specifics of the apparatus have been well documented [120, 165–172], and in the following we provide a brief overview of the most important components required to realize the models discussed in chapter 4.

5.1.1 Condensate production in brief

Here, we very briefly discuss condensate production in our moving-magnetic coil transporter apparatus. (For more detail, see [120]) We utilize ^{87}Rb atoms

in their ground state $5^2S_{1/2}$ (hyperfine states $|F = (1, 2), m_F\rangle$ with two excited states $5^2P_{1/2}$ and $5^2P_{3/2}$, of which the second one is separated from the ground state by $\lambda \approx 780$ nm. Starting from a magneto-optical trap (MOT) consisting of three counter-propagating pairs of cycling light (cycling transition $F = 2 \rightarrow F' = 3$) and a gradient magnetic field, we capture and cool approximately 1×10^{10} atoms at a temperature of about 1 mK. (We note that in addition to the cycling light, we apply repumping light, $F = 1 \rightarrow F' = 2$, to return atoms which escape from the cycling transition back to cyclable states.) Following the cooling in the MOT, we turn off the magnetic potentials and subject the atoms to a phase of optical molasses cooling [173] to achieve sub-Doppler cooling to about $50\mu\text{K}$. The atoms are then pumped into the $|1, -1\rangle$ state and transported to an ultra-high vacuum cell using our magnetic-transporter apparatus [120, 172].

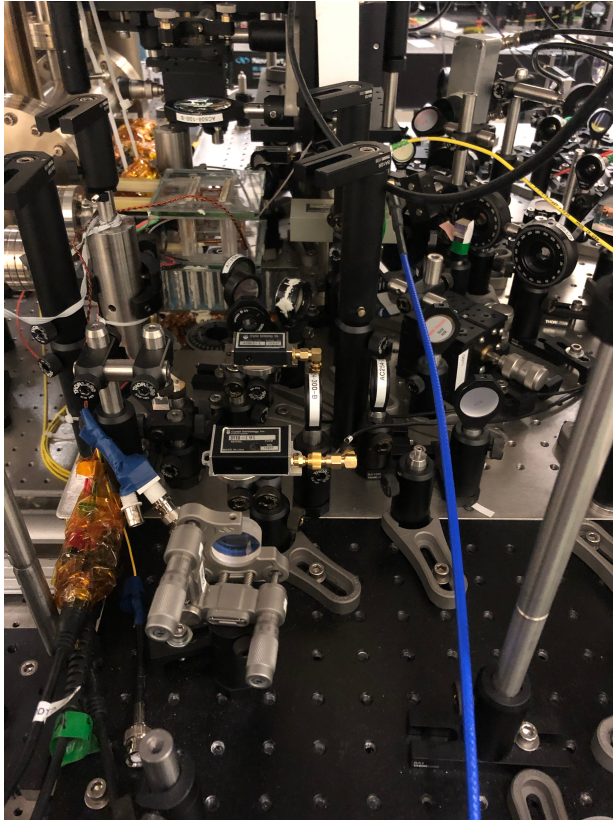


Figure 5.1: Picture of the science cell (ultrahigh vacuum cell) in which BECs are produced (glass cell, upper left). Visible in front and just left of center is the retro-reflection set-up used for creating one horizontal lattice.

After transport to the ultra-high vacuum cell, we evaporatively cool the

atoms in the quadrupole magnetic trap using a radio-frequency knife. After about 10 s, the efficiency of this evaporation becomes limited, and we switch to a time-orbiting-potential trap (TOP trap) [174] and continue efficiently evaporating in the magnetic trap followed by an optical trap composed of two crossed 1064 nm beams (XODT, crossed optical dipole trap), ultimately reaching BEC with a temperature of $T \sim 100$ nK and remaining condensate atom number anywhere between 10^4 and 10^6 atoms, determined by the specific XODT evaporation parameters. We note that due to many technical improvements during the author's tenure in the lab [172, 175], the duty cycle of the experiment is approximately 20 to 30 seconds, allowing for a factor of 2 or 3 increase in the number of data points which we can acquire in a given time.

5.1.2 Atom Imaging Scheme

We also briefly discuss our atomic detection scheme, for which more details may be found in [120]. After creating a BEC in the XODT, we perform an experimental iteration, and then quickly turn off all trapping potentials in a band-mapping procedure [176]. The atoms thus fall in time-of-flight, during which time they ballistically expand. This expansion during the approximately 15 ms time-of-flight used in the experiments described in this thesis results in an atomic sample which is large enough to be imaged using absorption imaging techniques [177] on a CCD camera (Princeton PIXIS 1024B). The time-of-flight also essentially performs a Fourier transform operation on the atoms, and thus our absorption images are approximately the momentum distribution of the initial atomic cloud at the time of their release from the trap, albeit with only density and not phase information.

After the atoms have fallen for an appropriate time-of-flight, we apply a Stern-Gerlach separation protocol in order to spatially separate atoms having different hyperfine projections m_F . The application of a gradient field perpendicular to the atoms' direction of motion separates the different spin components, thus resolving these states on the CCD. Since, however, there are two possible values for F , Stern-Gerlach separation is not enough to recover the full information of the atomic state, as, e.g., $|2, 1\rangle$ and $|1, -1\rangle$ have the same m_F times their respective Landé g-factors. In order to circumvent this problem, we first image atoms having $F = 2$ using resonant imaging light onto approximately one third of the CCD chip operating in kinetics mode. After a short time, the camera moves the illuminated pixels into an unused and shaded off region, and we apply first repump light and then imaging light to image the $F = 1$ atoms, which will have fallen by an additional 3 ms during this time. In this way, we separate all possible hyperfine states of our atoms in our imaging process, and thus we have access to the full atomic state population

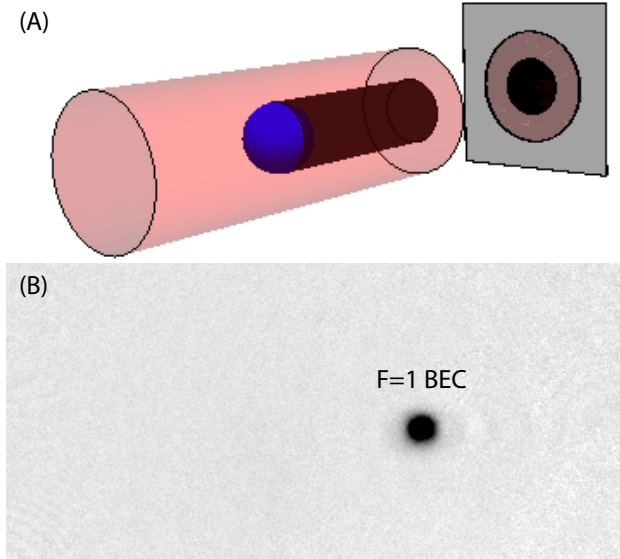


Figure 5.2: (A) Cartoon illustrating the principle behind absorption imaging of a BEC. Resonant $F = 2$ light shines upon an atomic sample, which absorbs and re-scatters the imaging light. This casts an effective shadow on a CCD camera. (B) Sample absorption image of an $F = 1$ BEC after converting photon counts from the CCD camera into an optical density (OD). This image is typical for a condensate only experiencing a crossed optical dipole (XODT) trap, and for this image, the condensate is found to have $\sim 100,000$ atoms.

information in our experiments.

5.1.3 State-selective Optical Potentials

Laser fields have long been used to create potentials for ultracold atom experiments, including the creation of periodic potentials (optical lattices) by retro-reflection of a laser beam to create a standing wave of light. In order to perform the experiments discussed in chapter 4, we require a deep optical lattice potential for one atomic species and a shallow or vanishing lattice potential for the other. The answer can be found in the form of state-selective lattice potentials, that is, potentials which have a different magnitude (and even sign) for different atomic hyperfine states. The details of a state-selective lattice have been thoroughly discussed in [125, 156, 157], and many experiments in our research group make use of them to study phenomena from atomic wave mixing, the Bose-glass transition in the presence of disorder, and matter-wave diffraction from an atomic or else from no potential [69, 82, 83, 86, 87].

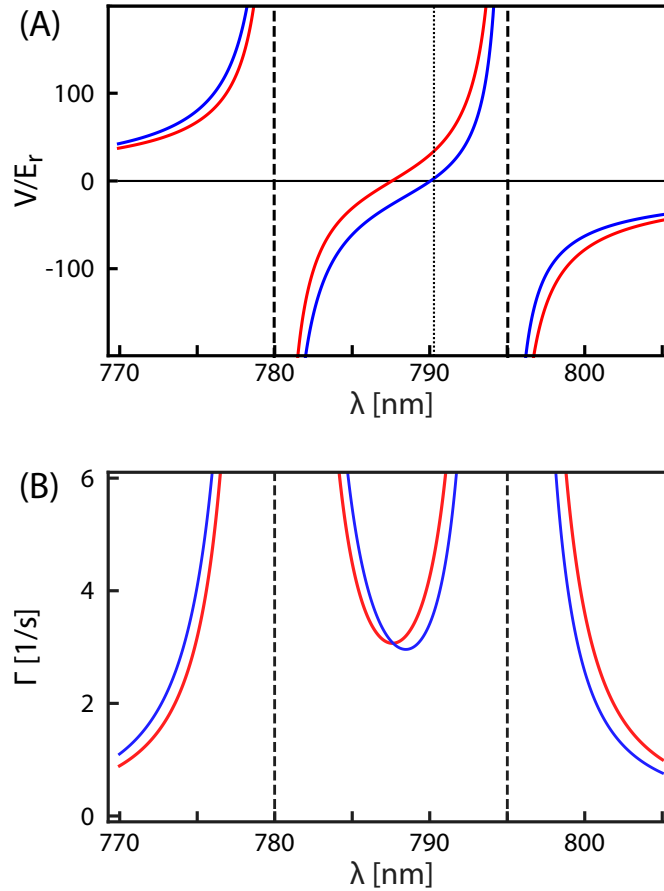


Figure 5.3: (A) Calculated optical potential for state selective light based on equation (5.1). The potentials are shown for $|r\rangle = |1, -1\rangle$ in red and $|b\rangle = |2, 0\rangle$ in blue with σ^- polarized laser light as a function of wavelength. The overall scale is intensity dependent, and the selected curves are computed for $I = 0.38$ kW/cm 2 . The small-dashed line shows the wavelength used in section 5.3, $\lambda = 790.4$ nm, for which the lattice depths are $s_r = 20$ and $s_b = 2.5$. (B) Corresponding scattering rates for the same parameters. At $\lambda = 790.4$ nm, they are respectively $\Gamma_r = 5$ s $^{-1}$ and $\Gamma_b = 4$ s $^{-1}$

The basic idea behind a state-selective potential for ^{87}Rb is that due to the presence of two strong ground state transitions (from the ground state ${}^1S_{1/2}$ to excited states ${}^2P_{1/2}$ and ${}^2P_{3/2}$), usually called D_1 and D_2 at ≈ 795 nm and ≈ 780 nm respectively [121], the light shifts relative to each transition line can cancel for a certain hyperfine state of ${}^1S_{1/2}$ at a certain polarization. That is, if we tune the laser wavelength to be between the D_1 and D_2 lines, we

can select a wavelength for which the blue-detuned shift from D_1 partially or fully cancels the red-detuned shift from D_2 . A full calculation can be found in [151,89], with the result

$$U(\mathbf{r}, i, p) = \frac{3\pi c^2}{2} \left[\frac{\Gamma_{D_1}}{\omega_{D_1}^3} \sum_{l \in P_{1/2}} \frac{|c_p^{li}|^2}{\omega - \omega_{li}} + \frac{2\Gamma_{D_2}}{\omega_{D_2}^3} \sum_{l \in P_{3/2}} \frac{|c_p^{li}|^2}{\omega - \omega_{li}} \right] I(\mathbf{r}) \quad (5.1)$$

where i indexes the initial hyperfine state, $\Gamma_{D_{1,2}}$ is the scattering rate of the $D_{1,2}$ transition, c_p^{li} is a Clebsch-Gordon coefficient between the initial and final hyperfine states, p denotes the polarization of the light, which may be σ^\pm or π -polarized, and $I(\mathbf{r})$ is the intensity profile of the optical potential.

We note that (5.1) depends on the choice of polarization and hyperfine state. We plot in fig. 5.3(A) the optical potential for the state pair $|r\rangle = |F = 1, m_F = -1\rangle$ and $|b\rangle = |2, 0\rangle$. The tune-out wavelength for $|b\rangle$ atoms occurs at $\lambda = 790.0$ nm independently of polarization, and for σ^- light, this wavelength produces a residual blue-detuned optical lattice for $|r\rangle$ atoms. By choosing wavelengths appropriately around this point, we may create a differential lattice for $|r\rangle$ and $|b\rangle$ atoms having the same detuning or opposite detunings, resulting in an effectively *shifted* lattice for one state by $\lambda/4$.

For completeness, we note that near the D_1 and D_2 lines, the ^{87}Rb atoms are subject to near resonant scattering, whose rate may be computed similarly to (5.1) [178] with the result

$$\Gamma_i(\mathbf{r}, t) = \frac{\pi c^2 \Gamma_{D_2}}{2\hbar\omega_0^3} \left[\Gamma_{D_1} \frac{1 - g_F m_F q}{\Delta_{D_1}^2} + \Gamma_{D_2} \frac{2 + g_F m_F q}{\Delta_{D_2}^2} \right] I(\mathbf{r}, t) \quad (5.2)$$

The scattering rate is shown for the same parameters as the optical potentials in fig. 5.3(B). For the experiments we will describe in the following, the scattering rates for $|r\rangle$ and $|b\rangle$ atoms are approximately 4.8 s^{-1} and 3.7 s^{-1} respectively, which will not prove to be limiting for the experiments described below.

5.1.4 Microwave hyperfine transitions

In order to perform our experiments, we require precise control over the hyperfine state of our Rubidium-87 BECs. Specifically, we will work completely in the ground state manifolds $F = 1$ and $F = 2$ after preparing an initial $|F = 1, m_F = -1\rangle$ BEC [120]. In order to perform emission experiments, we must prepare atoms in $|r\rangle = |1, -1\rangle$ and $|b\rangle = |2, 0\rangle$, and for magnetic field post-selection, we require also the ability to the populate $|2, -1\rangle$ and $|2, -2\rangle$

hyperfine states [175]. At a fixed magnetic field, applied in the laboratory by three sets of Helmholtz-coils (one per spatial direction), the transitions within the $F = 1$ and $F = 2$ manifolds are in the radio-frequency (RF) range, whereas the transitions between the $F = 1$ and $F = 2$ manifold are in the microwave regime, as can be calculated from the Breit-Rabi formula [179].

In order to generate microwave fields for hyperfine state transitions, we utilize a microwave synthesizer locked to an external Rubidium frequency standard, to which we mix in a smaller, RF signal created according to the experimental design needs using Agilent Tektronix arbitrary function generators. This signal is ultimately fed into a rectangular microwave waveguide antenna, which generates the microwave field at the position of the atoms. (For full details of the microwave set-up, see [169].)

5.1.5 Sample preparation

The experiments described in this chapter begin by creating an optically-trapped Bose-Einstein condensate, as discussed in section 5.1.1. Ultimately, we seek to create a Mott-insulating phase having average site occupation number $\langle n_i \rangle \lesssim 0.5$. The experiments all deal with 1D physics, for which we create deep horizontal (state-independent) lattices such that the tunneling time between neighboring tubes is much larger than the experimental timescales. We note that in ramping on optical lattice potentials, we incur a shift of the position of the trap minimum with respect to the un-shifted trap due to gravity, known as gravitational sag. In the experiments of section 5.2, we turned on all optical lattice potentials at the same time, resulting in an appreciable gravitational sag, which had consequences on our observations, described in more detail in section 5.2.2. In order to minimize gravitational sag for the experiments of section 5.3, the horizontal lattices are first adiabatically ramped up in 80ms followed by the vertical state-dependent lattice (90 ms) to final depths of $40E_{r,1064\text{nm}}$, $40E_{r,1064\text{nm}}$ and $20E_{r,790.41\text{nm}}$ so that the atomic cloud sits at approximately the trap minimum potential, with a residual confinement along the z -direction of $\omega_z \approx 2\pi \times 100$ Hz. Here, $E_{r,\lambda}$ is the recoil energy of the lattice. We determine the lattice depths using Kapitza-Dirac diffraction [38, 180–184] of the atomic sample in the three directions of interest. This procedure creates a Mott-insulating sample deep within the Mott regime. With atoms loaded into the lattice, a variable fraction f is transferred, at a bias field of 5 G, to an intermediate $|2, 1\rangle$ state using a two-photon microwave and radio-frequency pulse of about 2 ms duration. The transferred atoms are removed using resonant light on the D_2 cycling transition. After the pulse sequence (in which f is adjusted between 0.6 and 0.85 to compensate for differing initial atom number), the remaining sample has about $2.7(3) \times 10^4 |r\rangle$ atoms with an average

site occupation of $\langle n_i \rangle \lesssim 0.5$ in the tubes.

5.1.6 Determining the resonance condition

The resonance condition $\Delta = 0$ is defined with respect to the transition between the band minimum $\varepsilon_{n=1,q=0}$ and the harmonic-oscillator ground state in the emitter potential (with a residual bandwidth of $1 \times 10^{-2} E_r$). We use lattice transfer spectroscopy [86] to determine the resonance condition. An optically trapped BEC of $|r\rangle$ atoms is first transferred into the $|b\rangle$ state, after which the state-dependent lattice potential is ramped on slowly. Microwave pulses of duration $\tau = 400\mu\text{s}$ are then applied at a fixed strength $\Omega = 2\pi \times 1.0$ kHz and variable frequency to transfer maximally 30% of population into the $|r\rangle$ state. The $\Delta = 0$ frequency for use in the experiment is obtained from a fit of a Rabi spectrum to the data. Systematic residual mean-field shifts are estimated to be between 150 and 270 Hz for all initial atom numbers used, based on a direct simulation of the 1D time-dependent Gross-Pitaevskii equation. The resonance condition (which depends on both optical and magnetic fields) is stabilized using a post-selection magnetometry technique, yielding an uncertainty of $\sigma_E \approx 350$ Hz [91, 175].

5.2 Experiments on free-particle emission

In this section, we highlight some of the experimental results of [91], with a special focus on where the data obtained therein do and do not match the models presented in sec. 4.3. We note that while material photonic crystal systems have observed many predicted features of spontaneous emission near a continuum edge (such as modified spontaneous emission rates [101, 105] and Lamb shifts [185], spectral signatures of non-exponential decay [186], and evidence for photon bound states in photonic crystal waveguides [109] and corrugated microwave guides [110]), a direct observation of many salient features was first accomplished using our cold atomic platform [91]. This experiment has been described in detail in the PhD thesis of my colleague Ludwig Krinner [172], thus we shall only survey the results here.

5.2.1 Spontaneous Emission near a Single Edge

We briefly discuss how to use the techniques of sec. 5.1 in order to simulate the physics of spontaneous emission near a single energetic edge. We create a strongly-confining array of 1-dimensional tubes using retro-reflected $\lambda = 1064$ nm light (depth $V_0 = sE_r$ with $s = 40$ and $E_r = \hbar^2 k^2 / 2m_{Rb}$ the recoil energy,

related to the wavelength through $k = 2\pi/\lambda$). Along the third axis, we apply state-selective light at $\lambda = 790$ nm, for which the state $|b\rangle = |2, 0\rangle$ experiences no lattice potential at all, $s_b = 0$, and with power chosen such that the state $|r\rangle = |1, -1\rangle$ feels a blue-detuned lattice of depth $s_r = 30$. In this way, the red atoms $|r\rangle$ realize the ground and excited states of the emission model in sec. 4.3 as an occupational spin, that is, an empty well of the deep lattice is $|g\rangle$, and a well with a single atom present is $|e\rangle$. The atoms in state $|b\rangle$ are free to propagate along the tube axis, and thus they form a continuum of states corresponding to the momentum of the atom: $|0\rangle$ is the state with no blue atom present, and $|1_k\rangle$ is the state with one blue atom having momentum (equivalently, wavevector) k .

By applying a microwave coupling at a given strength Ω and detuning Δ , we realize the Hamiltonian of eq. (4.9), and we schematically present the scheme in fig. 2.2. It is important to note that the detuning Δ now plays the role of the excited state energy of the atomic quantum-emitter (QE), and that this value may be tuned arbitrarily above or below the edge of the mode continuum (corresponding to $\Delta = 0$). We note in contrast that the QE excited state energy is fixed by a material's properties in a photonic band-gap material, and furthermore that we may also tune the strength of our coupling $g_k \propto \Omega$ by varying the strength of our microwave signal.

Much like the Weisskopf-Wigner model discussed in sec. 3.3, there should exist a regime well inside of the continuum (i.e. for $\Omega/\Delta \ll 1$) for which the emission of atoms from the excited state is Markovian, and whose rate is given by Fermi's Golden Rule, c.f. sec. 4.3.3. We experimentally probe this regime in fig. 5.5 for $\Omega/\Delta \approx 0.4$ and $\Delta \approx 2\pi \times 2$ kHz by creating a (mostly empty array of) QE(s) and applying coupling at strength Ω for a time τ and recording the relative population of $|r\rangle$ and $|b\rangle$ atoms. Due to residual axial confinement along the 1D tube, we restrict our attention to times shorter than the inverse trapping frequency, $\tau_{exp} < \tau_z = 2\pi/\omega_z \approx 10$ ms. The predicted Markovian decay rate is $\Gamma = 2\pi \times 72$ Hz, and for comparison with the theory of chapter 4, we show the full solution. The theoretical model is seen to differ dramatically from the observed behavior in that the model decays to zero population for long times and the experimental data only partially decay in the long time limit. We understand this effect as a manifestation of the fact that we have more than one QE (in fact, a whole lattice of them at the start of the experiment), and this plateau is consistent with numerical simulations displaying a phenomenon similar to radiation trapping [91, 172].

In addition to the decayed fraction of $|r\rangle$ atoms, we can measure the momentum of the emitted atoms. Conservation of energy dictates that for a fixed QE energy $\hbar\Delta$, the momentum will vary according to $\bar{k} = \sqrt{2m\Delta/\hbar}$, and in

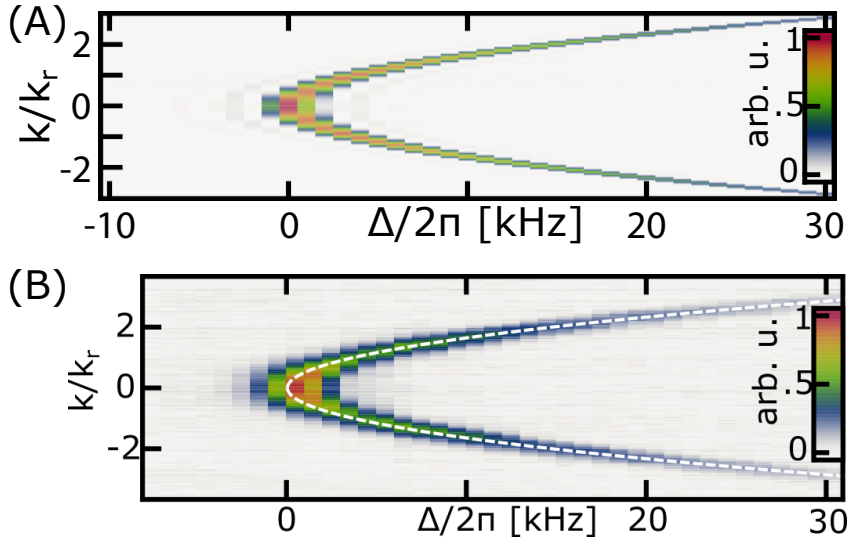


Figure 5.4: (A) Theoretically predicted momentum space emission profiles for a pulse of $\tau = 400 \mu\text{s}$, $\Omega = 2\pi \times 1.5 \text{ kHz}$, and variable detuning Δ . The computation assumes a deep lattice potential of depth $s_r = 30$. (B) Measured momentum space profile for the parameters as in (A) (reproduced from [91]). The white-dashed line shows the expectation based on energy conservation.

addition to this naïve estimate, we may compute the distribution of the emitter radiation as a function of time and QE energy. We present a comparison of both theoretical approaches to the data, taken for $\tau = 0.4 \text{ ms}$ and $\Omega = 2\pi \times 1.5 \text{ kHz}$, in the lower half of fig. 5.4, with the theoretical expectation for $|B_k|^2$ (c.f. equation (4.43)), shown in the top half of fig. 5.4. We see that the qualitative and quantitative features are generally well explained by the model presented in section 4.3.

The strongest non-Markovian behavior is predicted for the regime where $\Delta \sim 0 \text{ kHz}$, where the 1D density of states diverges at the band edge. We plot results from time-dependent population measurements near the edge ($\Delta = 2\pi \times -0.1 \text{ kHz}$ and $\Omega = 2\pi \times 3.0 \text{ kHz}$) and at negative QE energy ($\Delta = 2\pi \times -1.7 \text{ kHz}$) in fig. 5.5. The theoretical model of sec. 4.3.2 (shown as a black line in fig. 5.5) is found to display qualitative behavior similar to that which is observed for approximately $\Delta = 0$, and good quantitative agreement with the data is achieved for the model at negative detunings. The deviations of the data from the model for $\Delta \approx 0$ are consistent with numerical simulations featuring more than one emitter (see [91]), and when the QE energy is very negative, the coupling to $|b\rangle$ modes is reduced to the point that the dynamics is effectively governed by a single QE, thus recovering the quantitative

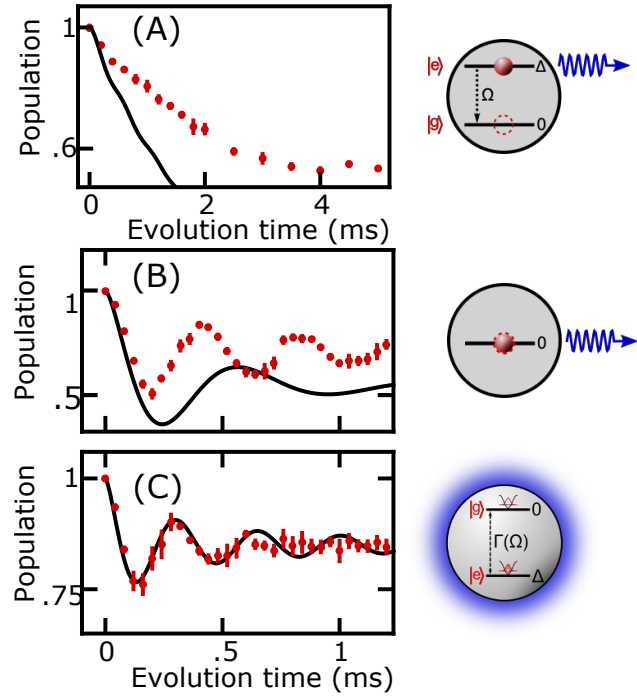


Figure 5.5: Predicted (black line) and observed (red circles with error bars) decay dynamics of the emitter population when emitting in the vicinity of a single edge in 3 regimes. (A) (Quasi-)Markovian regime (when $(\Omega/\Delta)^2 \ll 1$) displays an exponential decay. Data taken at $\Omega = 2\pi \times 0.74$ kHz and $\Delta = 2\pi \times 1.9$ kHz, and the error bars are the standard error of the mean (s.e.m.) from at least three iterations. (B) Non-Markovian behavior near the edge, $\Delta \sim 0$, with $\Delta = 2\pi \times -0.1$ kHz and $\Omega = 2\pi \times 3.0$ kHz. Observed behavior in (A) and (B) deviates from the model of section 4.3, and this can partially be explained by presence of neighboring emitters [91]. (C) Non-Markovian behavior away from the edge $\Omega/\Delta < 0$, with $\Delta = 2\pi \times -1.7$ kHz and $\Omega = 2\pi \times 3.0$ kHz. Here, where neighboring emitters play no role, the data and model agree within the error bars. Figure partially reproduced from [91], see also [172].

predictions of the model.

5.2.2 Matter-Wave Emitter Bound State

The fractional decay in the theoretical model of sec. 4.3.2 has its roots in the presence of a long-predicted bound state in which the emitter dresses itself with a coherent cloud of emitted modes [97]. In particular, the incomplete

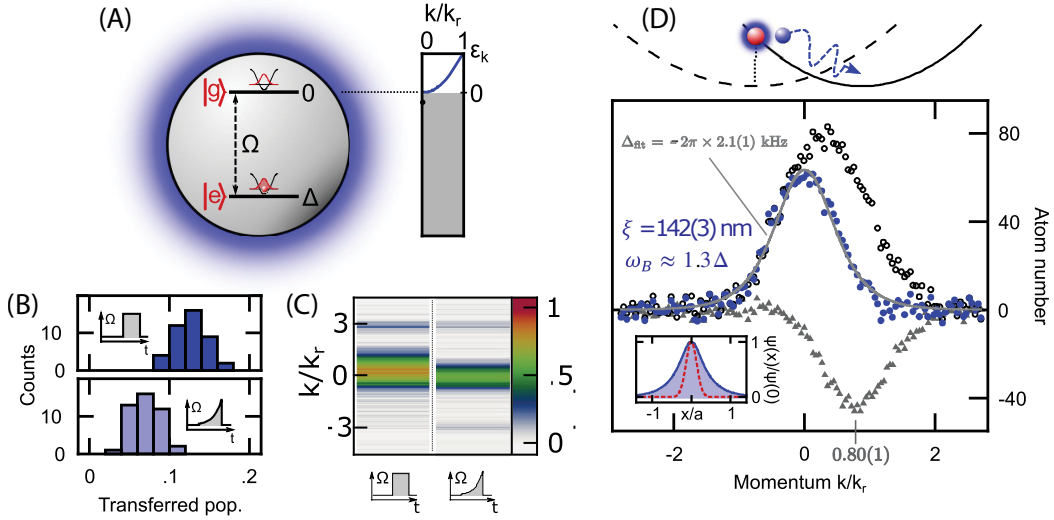


Figure 5.6: (A) Schematic illustration of bound states when the quantum emitter energy is negative. (B) Histograms showing the asymptotic population of $|b\rangle$ atoms after $\tau = 2.6$ ms, $\Omega = 2\pi \times 3.0$ kHz and $\Delta = -2\pi \times 2.2$ kHz. The top (bottom) panel shows the results for a sudden (respectively adiabatic) coupling of $|r\rangle$ to $|b\rangle$, and the shift in their centers hints at the formation of a bound state “smoothly” for the slow coupling case. Each histogram is taken for 50 points. (C) Sample momentum distributions for sudden (left) and slow (right) microwave couplings at parameters as in (B). The apparent asymmetry in the sudden coupling case suggests that some portion of the population is moving preferentially in one direction along the tubes. (D) Measured bound state. Guided by the observation in (C), the sudden coupling case is asymmetric due to the system being located away from the trap center, and the emitted atoms being subject to the gravitational potential due to this gravitational sag [91] (top panel). We plot the atom number for sudden coupling (empty black circles), slow coupling (blue circles), and the difference of the two (gray triangles). The gray triangles are distributed about $k_{sag} = 0.8k_r$, as expected from the gravitational sag in the trap. The gray curve passing through the blue data is a Fourier transform of (4.62) fit to $\Delta_{fit} = -2\pi \times 2.1$ kHz (in good agreement with the experimental value). This wavefunction has a spatial decay length of $\xi = 142$ nm. Inset: Comparison of the size of the Wannier function on a site (red) and the evanescent matter wave cloud of the bound state (blue, shaded). Figure reproduced from [91], c.f. also [172].

decay is governed by how strongly the bound-state excitation is coupled to (4.27). This bound state has a wavefunction that is roughly exponentially

localized around the QE, c.f. fig. 4.4, with a decay length ξ approximately given by (4.63), namely, $\xi \propto 1/\sqrt{|\Delta|}$.

In order to study the bound state in detail, it is important to not populate any propagating modes $|1_k\rangle$ appreciably, for which we develop a protocol to ramp up the microwave coupling slowly with respect to the bound state binding energy $\omega_B \approx \Delta$. This slow coupling strength ramp prevents propagating modes from becoming populated, and thus all observed $|b\rangle$ atoms belong to the bound state. The result is shown in fig. 5.6. We note that a Fourier transform of the bound-state wavefunction (4.62) fits the data well with only the QE energy Δ as a fit parameter, and the corresponding decay length is predicted to be $\xi \approx 142$ nm. Further evidence is provided for the existence of the bound fraction resulting from a roll-down of the emitted population from the side of the harmonic potential, a discussion of which can be found in [91], and which was discovered and understood by L. Krinner independently of the considerations arising from the theoretical model of sec. 4.3.5.

5.3 Experiments on emission into a band structure

This section presents in large part the results of our preprint [149]. As discussed in section 4.4, distinctive features in emission dynamics and bound state structures arise in the presence of a band-structure, specifically in the presence of a band with two edges rather than a semi-infinite continuum. Since material systems have a band structure consisting of multiple bands, the insights we gain in our ultracold-atomic simulator may be of relevance to diverse applications in waveguide-QED.

5.3.1 Band Spectroscopy

The experiment proceeds as in 5.2, however, in the present experiment we choose a non-vanishing $s_b > 0$ (depth of the lattice for $|b\rangle$ atoms) such that the mode continuum acquires a band structure. The dynamics of an isolated emitter (ground and excited states $|g\rangle$ and $|e\rangle$) is then governed by the Hamiltonian

$$\hat{H} = \sum_{n,q} \hbar g_{n,q} e^{i\Delta_{n,q} t} |g\rangle \langle e| \hat{b}_{n,q}^\dagger + \text{H.c.} \quad (5.3)$$

involving Bloch bands, where $\Delta_{n,q} = \Delta - \varepsilon_{n,q}/\hbar$ is the effective detuning of the emitter (excitation energy $\hbar\Delta$) from the Bloch state $|n, q\rangle = \hat{b}_{n,q}^\dagger |0\rangle$ with energy $\varepsilon_{n,q}$ (band index n , quasimomentum q); the vacuum coupling

$g_{n,q} = \gamma_{n,q}\Omega/2$ contains the Franck-Condon overlap $\gamma_{n,q} = \langle n, q | \psi_e \rangle$ with the originating harmonic-oscillator ground state $|\psi_e\rangle$ in an emitter. We choose $s_b = 2.5$ (at $\lambda = 790.4$ nm) giving a ground-band width $W_1 = (\varepsilon_{1,k} - \varepsilon_{1,0}) = 0.5 E_r \approx h \times 1.8$ kHz. The band structure and corresponding Franck-Condon factors are illustrated in Fig. 5.7(B).

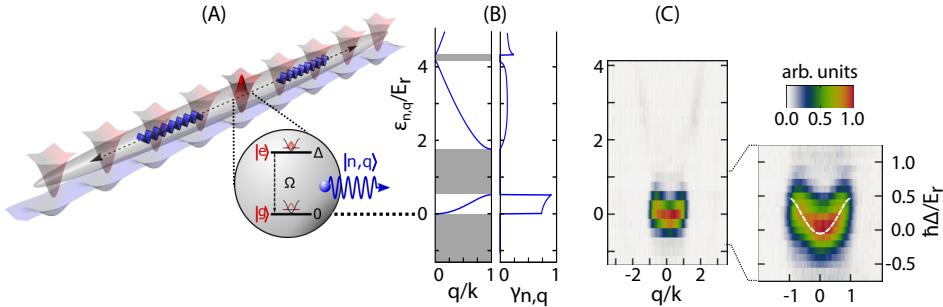


Figure 5.7: (A) Experimental scheme. ^{87}Rb atoms in two hyperfine ground states $|r\rangle$ (“red”) and $|b\rangle$ (“blue”) are confined in state-independent 1D lattice tubes. A state-dependent longitudinal lattice provides strong confinement for one hyperfine state ($s_r \gg 1$) and a shallow band structure for the other ($s_b \approx 2.5$). Coupling between $|r\rangle$ and $|b\rangle$ (strength Ω , detuning Δ) leads to emission into the band structure; each well acts as an emitter characterized by an occupational spin (states $|e\rangle$ and $|g\rangle$) and excitation energy $\hbar\Delta$. (B) Band structure and relative strength of the vacuum coupling $\gamma_{n,q(\varepsilon)}$ (Franck-Condon factor computed for a selection of densely spaced Bloch waves) for $s_b = 2.5$ and $s_r = 20$. (C) Measured quasimomentum distribution versus emission energy $\hbar\Delta$, as seen with absorption imaging after 14 ms time of flight, and averaged over at least 3 runs. The lattice parameters are as in (B); the coupling strength is $\Omega/2\pi = 1.0(3)$ kHz and the pulse duration $\tau = 400\mu\text{s}$. The zoom in is taken with a smaller step size of $0.1E_r$, and an average over at least 4 runs for each quasimomentum distribution, and the calculated band-structure is shown (white, dashed).

We first characterize the momentum distribution of the emitted $|b\rangle$ atoms as a function of the excitation energy $\hbar\Delta$ (calibrated using lattice transfer spectroscopy [172]). After loading the array with $|r\rangle$ atoms, we apply a rectangular microwave pulse of duration $\tau = 400\mu\text{s}$ and Rabi frequency $\Omega = 2\pi \times 1$ kHz; following a $500\mu\text{s}$ -long rampdown of all three lattices for band mapping. The emitted $|b\rangle$ atoms are detected after time-of-flight using state-selective absorption imaging. The measured distribution, shown in Fig. 5.7(C), reveals that emission into the ground band is much stronger than that into the first and higher excited bands. The suppression results from the structure of the

vacuum coupling $g_{n,q}$, which for even- n bands is reduced due the approximate parity of the relevant Bloch states for $s_b > 0$; a further suppression of the relevant Franck-Condon factor for higher n is due to the finite momentum width of $|\psi_e\rangle$ and the decrease in the density of states.

We note that it is also possible in our system to study the case where $s_b < 0$, which we can accomplish by changing the state-selective lattice wavelength using the tunability of our Coherent 899 Titanium-Sapphire laser. Specifically, by shifting the wavelength in the opposite direction from the tune-out point for $|b\rangle$ atoms, we create a situation in which the lattice depth for the $|b\rangle$ atoms is negative. We note that this results in an effective shift by $\lambda/4$ of the lattice wells for the emitters and the emitted matter-waves. This results in Franck-Condon factors that are appreciable for excited bands $n \geq 2$, c.f. Fig. 5.8(A), and in observed emission profiles with appreciable contributions from both the ground and first excited bands, cf. Fig. 5.8(B).

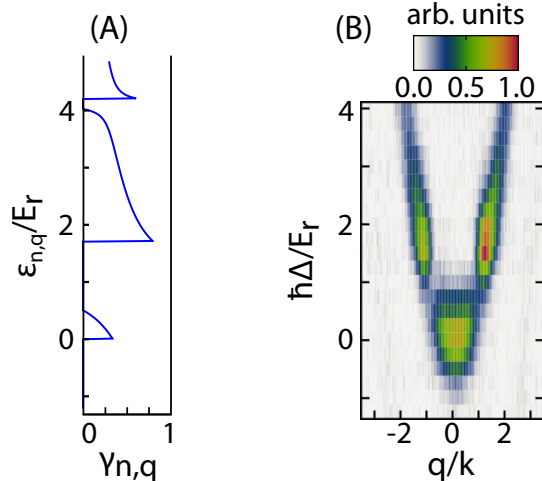


Figure 5.8: (A) Franck-Condon factor $\gamma_{n,q}$ and observed emission profile (B) for $s_b = -2.6$ at $\lambda = 789.8$ nm. The strongest emission signal occurs in the first excited band; the relatively strong percentage of atoms within the first band gap results from the strong coupling to the first excited band, giving rise to non-Markovian emission in the band gap. We note a residual asymmetry in the momentum distribution, which we attribute to residual gravitational effects.

While the case $s_b < 0$ is certainly interesting in its own right, both for the difficulty of realizing a similar system in a material as well as effects arising from the coupling to multiple bands, it is beyond the scope of this thesis. We shall instead focus on the case $s_b > 0$. As is apparent from fig. 5.7,

coupling to bands other than the ground band is suppressed on experimentally observable scales, and this justifies using the single band model of section 4.4. We therefore focus on the effects of only the ground band in what follows.

We have found in section 5.2 that the decay dynamics in an array of emitters is generally subject to propagation, reabsorption and collisional effects [91]; however a description for an isolated emitter should apply in the short-time limit. Furthermore, due to the experimentally motivated choice of $\varepsilon_{1,0} = 0$, the equations of section 4.4 are modified in the following way: the ground band is approximately sinusoidal,

$$\varepsilon(q) = -\hbar\bar{\omega} \cos\left(\frac{q\pi}{k}\right) + \hbar\bar{\omega} \quad (5.4)$$

(denoting $\varepsilon(q) \equiv \varepsilon_{1,q}$, and $\hbar\bar{\omega} \equiv W_1/2$) and the vacuum coupling $g = \langle g_{1,q} \rangle_q \approx 0.39\Omega$ is approximately constant over the band, with negligible coupling to other bands. We have re-introduced physical momentum units by taking $k = \pi/d$ to be the recoil wave-vector. The excited-state amplitude $A(t)$ then evolves as the Fourier transform

$$A(t) = \frac{i}{2\pi} \int_{-\infty}^{\infty} d\omega G(\omega + i0^+) e^{i(\Delta-\omega)t} \quad (5.5)$$

of the Green's function

$$G(\omega) = \frac{1}{\omega - \Delta - \Sigma(\omega)/\hbar} \quad (5.6)$$

in which the interaction of the emitter with the band is captured through the self-energy

$$\Sigma(\omega) = \frac{\hbar^2 g^2}{2k} \int_{-k}^k \frac{dq}{\hbar\omega - \varepsilon(q)} = \frac{\hbar g^2}{\sqrt{\omega(\omega - 2\bar{\omega})}} \quad (5.7)$$

whose singularities now lie at $\omega = 0$ and $\omega = 2\bar{\omega}$, which are the band edges given (5.4).

The dynamics of the emitter is governed by the singularities of $G(\omega)$ defined by $\omega - \Delta - \Sigma(\omega)/\hbar = 0$ which can be determined using standard analytical techniques (see section 4.4). In contrast to the single-edge case of section 4.3, there are now *two* bound states [116], one below the band and one in the gap *above* the band, as well as a nearly Markovian decay resulting from coupling to the band and additional, incoherent losses due to the divergence of the self energy at the band edges.

For a comparison with the model, we first consider the ground-band emission spectrum, which can be obtained from fig. 5.7(C) by integrating over the

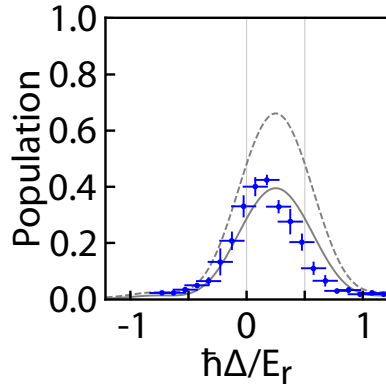


Figure 5.9: Ground-band emission spectrum for $g/\bar{\omega} = 0.43$ and $\tau = 400 \mu\text{s}$, obtained from the distributions in fig. 5.7 (C) by summing over quasimomenta. The dashed curve is the prediction of the isolated-emitter model, and the solid curve is the same prediction reduced by 40%. Deviations from the model have already set in by $\tau = 400 \mu\text{s}$, as can be seen in fig. 5.10.

quasimomenta. The agreement of the spectrum with the prediction (fig. 5.9) is good up to an overall scaling factor of order unity. This discrepancy arises from the fact that for the parameters chosen, the model of a single emitter already breaks down, even for short pulses of $400 \mu\text{s}$. This can be seen most apparently when we consider the time dynamics of an initially excited population.

5.3.2 Time Dynamics for Emission into a Band

In addition to measuring emission dynamics as a function of excited emitter energy $\hbar\Delta$, we can also fix the emitter energy, e.g. at the band center $\hbar\Delta = \hbar\bar{\omega}$ and instead record the population of the excited emitter as a function of the coupling pulse duration. We can distinguish three behavior regimes in the time dynamics as a function of the ratio of coupling strength to bandwidth $g/\bar{\omega}$, cf. fig. 5.10(A): irreversible decay for $g/\bar{\omega} \ll 1$ (weak coupling), damped oscillatory decay for $g/\bar{\omega} \sim 1$ (intermediate coupling), and undamped oscillations for $g/\bar{\omega} \gg 1$ (strong coupling).

A Wannier picture provides an intuitive interpretation of the model's predictions via the quantum Zeno effect [187, 188] (cf. fig. 5.10(B)): here, the atom coherently cycles with Rabi frequency $\Omega' = 2g$ between the strongly confining emitter well and a corresponding $|b\rangle$ well of the shallower lattice, where it is subject to tunnel escape at a rate $\sim \bar{\omega}$ that damps the coherent local evolution. In the strong-coupling limit, the bandwidth is negligible, and the population

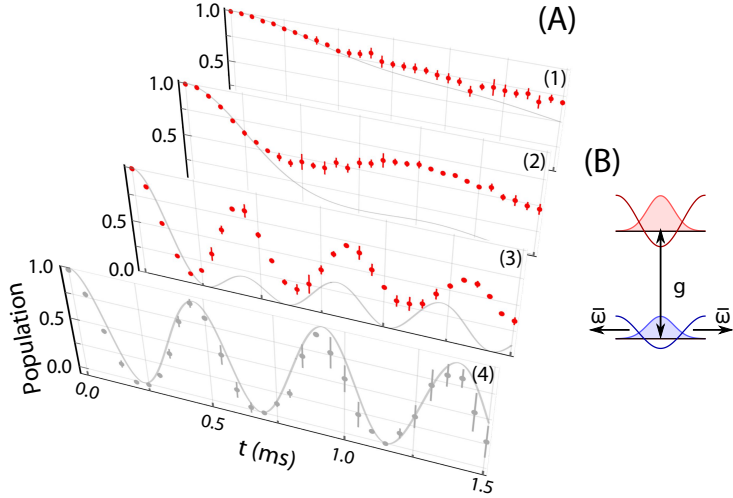


Figure 5.10: (A) Decay dynamics for $\hbar\Delta = h \times 1.8(1)$ kHz (at the band center) for (1) weak coupling with $\Omega = 2\pi \times 0.4$ kHz ($g/\bar{\omega} = 0.18$), (2,3) intermediate coupling with $\Omega = 2\pi \times (1.0, 2.3)$ kHz ($g/\bar{\omega} = 0.43, 1.0$), and (4) strong coupling for a reduced bandwidth ($W_1 = 0.1E_r$) with $\Omega = 2\pi \times 2.2$ kHz ($g/\bar{\omega} = 4.9$). The dots are data taken for different hold times, averaged over at least 3 runs each, with error bars representing the standard error of the mean (S.E.M.). The gray lines represent the predictions of the isolated-emitter model. (B) Schematic illustrating the competition between coupling g and tunnelling $\sim \bar{\omega}$ in the shallow lattice (see text)

trivially performs coherent Rabi oscillations between the emitter and the (now effectively single-mode) vacuum, in analogy to a simple cavity-QED scenario. A remnant of this effect persists even in the weak coupling regime for short times $t \lesssim \bar{\omega}^{-1} \sim 0.2$ ms when the associated Heisenberg uncertainty in energy exceeds the band width such that the band is not resolved and appears as a single state. This results in a decay dynamics that always starts quadratically, as a Rabi oscillation.

Generally there is good agreement between the model and the observation before significant population has been emitted (which mostly coincides with the short-time regime). Deviations, including an offset and enhanced oscillations, are expected to appear when atom reabsorption by neighboring empty emitters becomes relevant [91]. Proper accounting for these effects would necessitate a multi-emitter model, possibly including collisional interactions, which is beyond the scope of this paper. That said, the observed decay dynamics displays oscillations that last to long times, in qualitative agreement with the single emitter model, and for the spectrum of fig. 5.9, taken at $400 \mu\text{s}$,

the data only differ from the model by a constant scaling factor. For $g/\bar{\omega} \gg 1$, the emitters effectively decouple such that the isolated emitter model applies fully.

5.3.3 Bound States Above and Below the Band

Importantly, the spatial structure of a given bound state qualitatively depends on whether it is located below or above the band. Using the approach of section 4.4.5, it is straightforward to show that the bound states contain evanescent matter waves of the form

$$\psi_B^\pm(z) = \int_{-k}^k dq \phi^\pm(q) \langle z | 1, q \rangle \quad (5.8)$$

with quasimomentum probability amplitudes

$$\phi^\pm(q) = \frac{\hbar g}{2k} \frac{1}{\hbar\omega_B^\pm - \varepsilon(q)} \quad (5.9)$$

For the bound state above the band, where the energetic difference between $\hbar\omega_B^+$ and $\varepsilon_{1,\pm q}$ is smallest near $q = \pm k$, this means that $|\phi^+(q)|^2$ possesses a double-peaked structure in quasimomentum space. In contrast, for the bound state below the band, the quasimomentum is concentrated around $q = 0$.

To demonstrate these features, we directly detect the spatial features of two representative bound states symmetrically located on opposite sides of the band (where $\phi^\pm(q+k) = \phi^\mp(q)$) with emission energies $\hbar\Delta^\pm = (1 \pm 3)\hbar\bar{\omega}$ and weak coupling $(g/\Delta^\pm)^2 \ll 1$ (such that $\omega_B^\pm \approx \Delta^\pm$). We prepare the states by slowly ramping on the coupling g using a sinusoidal ramp. The ramp duration of 2 ms is long with respect to the bound state frequencies ω_B^\pm , and no dynamics are observed for a variable hold time between 0 and 0.5 ms following the ramp. The resulting quasimomentum distributions are observed in time-of-flight after a band-map of all optical potentials as before, c.f. fig. 5.11. The observed distributions match qualitatively the predictions for $|\phi^\pm(q)|^2$ (with a small higher-band contamination, see methods), with quantitative agreement if we allow for a blurring of $0.1k$ due to finite size effects (system size $\sim 10\mu\text{m}$) and imaging resolution. We note that the predicted below-band bound state, cf. fig. 5.11(A), resembles the state found near a single edge [91] while the sharp edges at $\pm k$ (not resolved in the data) lead to modulations in its spatial shape with the lattice periodicity, a feature that was suggested earlier in [97].

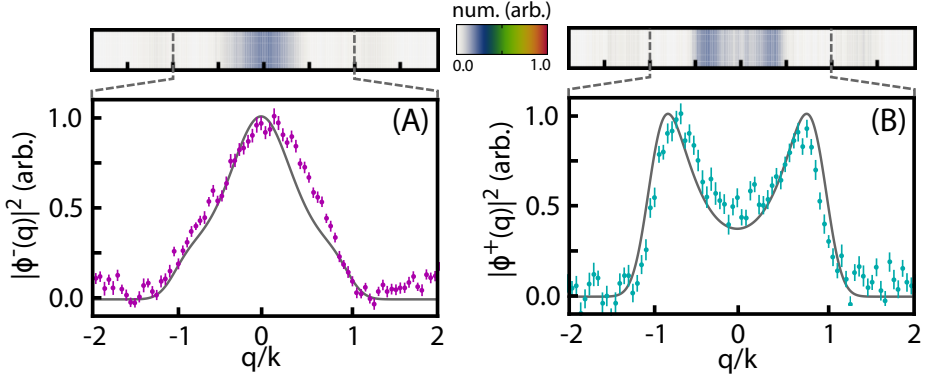


Figure 5.11: Structure of the bound states at $\hbar\Delta^+ = 1.0(1)E_r$ and $\hbar\Delta^- = -0.5(1)E_r$ below (A) and above (B) the band edges. (A) Observed quasimomentum distribution of the bound state below the band at $\hbar\omega_B^- = -2\hbar\bar{\omega} \approx h \times -1.9(3)$ kHz, where $a_l = \lambda/2$ is the lattice spacing, from time-of-flight following an adiabatic (2 ms long) ramp on of the coupling up to $g/\bar{\omega} = 0.43$. Each data-point is the average of more than 30 individual repetitions. The density plot shows the average time-of-flight picture. The gray curve is the quasi-momentum distribution from (A) convolved with a Gaussian blur ($\sigma = 0.1k$) to accomodate finite size effects and imaging resolution. (B) Observed distribution for the bound state above the band at $\hbar\omega_B^+ = 4\hbar\bar{\omega} \approx h \times 3.9(3)$ kHz, taken as in (A). The gray curve is blurred with the same Gaussian as in panel (A).

Chapter 6

Theoretical considerations for bound-state induced many-body physics in optical lattices

Given that our experimental system features many emitters in an array, we might be tempted to ask whether or not these neighboring emitters play a role in the observable physics. The answer is a resounding yes! Because of the presence of many emitters is intrinsic to our system, it behooves us to consider the possibility of observing many-body effects in our system, going beyond the model of chapter 4. We begin with a brief overview of quantum master equations as a means to describe the effect of many particles and then introduce one of the most well-known many-body models in optical lattice physics, the Bose-Hubbard model. After this (textbook level) overview, we will demonstrate how a Markovian master equation treatment of our system is predicted to modify the superfluid to Mott-insulator transition in an array of quantum emitters coupled to a free-particle continuum. This calculation is the essential novelty of this chapter, and we round out the discussion with several proposals for experiments to investigate the many-body character of the quantum emitter array.

As a word of caution before we embark on this journey, we wish to highlight a shift in the usage of the word Markovian. Previously (chapter 4), we invoked the Markovian approximation when studying emission of matter-waves into free space in 1D, and found that the emitters should not decay for $\Delta < 0$ at this level of approximation. In order for this approximation to be valid, the typical coupling strengths must be small compared to any energetic divergences in the density of states (specifically, we described $(\Omega/\Delta)^2 \ll 1$ as being Markovian). In what follows, we revive the language of systems and baths, and we take as our definition of Markovian to be that the dynamics of the

excited state in the system \mathcal{S} are slow when compared to a typical timescale of the reservoir. In this case, we will see that a Markovian description applies even for the case of $\Delta < 0$. It is not strictly necessary to invoke this Markovian approximation to compute a master equation for a quantum system [140], but it will suffice for our purposes to work with the Markovian quantum master equation. We note that some of these ideas were already considered by I. de Vega, et al. in 2008 [112], and its extension [122]. Specifically, the original matter-wave emitter proposal [112] did not stop with considering dynamics of a single quantum emitter in 3D, but rather predicted, using a Markovian master equation, several many-body effects. In particular, for $\Delta < 0$, novel Hubbard models with beyond nearest-neighbor coupling were demonstrated to be realizable in an experiment. This chapter extends this approach for our 1D situation.

6.1 Master equations

In order to treat the physics of a system of many quantum emitters interacting through a shared bath, we shall turn our attention to the approach based on quantum master equations first mentioned in section 3.2 [92, 140]. In this section, we shall introduce the master equation formalism and some of its general properties. Then we specialize to the case of our free particle model from 4.3 and compute the Markovian master equation for a system of quantum emitters of matter waves. In the following section, we will use this Markovian master equation to demonstrate a renormalization of the effective Hubbard model parameters and discuss the superfluid to Mott-insulator transition in our emitter system.

Formally, for a time-dependent Hamiltonian, the unitary time-evolution operator for a quantum state (in the Schrödinger picture) may be written

$$\hat{\mathcal{U}}(t, 0) = \mathcal{T} \exp \left(\frac{1}{\hbar} \int_0^t \hat{H}(\tau) d\tau \right). \quad (6.1)$$

A quantum system need not start in a single, well-defined quantum state $|\psi_a\rangle$, however. The density operator (equivalently: density matrix) $\hat{\rho}$ can describe such a mixed state. The density operator satisfies the well-known von Neumann equation

$$\frac{d\hat{\rho}}{dt} = -\frac{i}{\hbar} [\hat{H}(t), \hat{\rho}(t)] \quad (6.2)$$

which resembles the Heisenberg picture equation of motion for the evolution of a time dependent operator, with a difference in sign on the right hand side.

Furthermore, the expectation value of any observable $\hat{\mathcal{O}}$ may be computed if we know the density matrix via the trace operation:

$$\langle \hat{\mathcal{O}} \rangle = \text{Tr} [\hat{\mathcal{O}} \hat{\rho}] \quad (6.3)$$

It is at this point that we return our attention to system plus reservoir models. We again assume that the total Hilbert space consists of a small set of states \mathcal{S} of interest, called the system, and a (larger) set of states \mathcal{R} , called the reservoir or bath, with which the system can interact. The Hamiltonian schematically is assumed to take the form $\hat{H}(t) = \hat{H}_S + \hat{H}_R + \hat{H}_I(t)$, with \hat{H}_S (\hat{H}_R) the Hamiltonian of the system (respectively: bath), and $\hat{H}_I(t)$ the interaction between them. Note that any time-dependence in the Hamiltonian is contained in the interaction piece. We remember that the time evolution operator in the full system plus reservoir Hilbert space is unitary, and thus in principle, there is no decoherence. However, if we focus our attention on only the system \mathcal{S} and “don’t keep track of” the reservoir \mathcal{R} , then we may appear to have decoherence and dissipation arising in the system \mathcal{S} alone.

To be more precise, we assume that the full equations of motion for the system plus bath are too complicated to solve fully. We can, however, restrict our attention to just the system by tracing over the reservoir degrees of freedom, and thus obtain the reduced density matrix

$$\hat{\rho}_S = \text{Tr}_R [\hat{\rho}] \quad (6.4)$$

where the trace in (6.4) is taken over the reservoir states only. The reduced density operator describes how the system \mathcal{S} evolves in the presence of a bath. By exchanging quantum mechanical probability with the bath, the system may appear to decay, and we arrive at a possibility of dissipative behavior. Note that by taking the trace of the von Neumann equation (6.2), we find that the reduced density operator evolves according to

$$\frac{d\hat{\rho}_S}{dt} = \frac{1}{i\hbar} \text{Tr}_R \left([\hat{H}(t), \hat{\rho}(t)] \right) \quad (6.5)$$

Though this equation is in general quite complicated, making some approximations will render it into a well-studied form referred to as the Lindblad master equation (or just master equation) [92].

The steps to get to the usual form of the quantum master equation from (6.5) are a textbook exercise and we refer the reader to [92] for the full details. Borrowing their notations temporarily (and following their convention $\hbar = 1$),

we find (c.f. [92] eq. 3.136) that

$$\frac{d\hat{\rho}_S}{dt} = \sum_{\omega} \sum_{\alpha,\beta} \Gamma_{\alpha\beta}(\omega) (A_{\beta}(\omega)\hat{\rho}_S A_{\alpha}^{\dagger}(\omega) - A_{\alpha}^{\dagger}(\omega)A_{\beta}(\omega)\hat{\rho}_S(t) + H.c.) \quad (6.6)$$

with $A_{\alpha}(\omega)$ a so-called Lindblad operator. The Lindblad operators are model dependent, and we shall discuss them when we specialize to our atomic emitter model. This equation can be simplified by breaking the coefficients $\Gamma_{\alpha\beta}$ into its real and imaginary parts

$$\Gamma_{\alpha\beta} = \frac{1}{2}\gamma_{\alpha\beta}(\omega) + iS_{\alpha\beta}(\omega) \quad (6.7)$$

which reduces (6.6) to the form

$$\frac{d\hat{\rho}_S}{dt} = -i[H_{LS}, \hat{\rho}_S] + \mathcal{D}(\hat{\rho}_S) \quad (6.8)$$

We see immediately that (6.8) consists of two parts: a unitary evolution by H_{LS} and a dissipative piece. Let us discuss everything in turn.

First, we discuss how $\Gamma_{\alpha\beta}$ is defined. The reservoir is well described by correlation functions

$$G_{\alpha\beta}(\omega) = \langle B_{\alpha}^{\dagger}(t)B_{\beta}(0) \rangle \quad (6.9)$$

The complex master equation rates are then obtained from correlations of the reservoir by

$$\Gamma_{\alpha\beta} = \int_0^{\infty} e^{i\omega t} G_{\alpha\beta}(t) \quad (6.10)$$

We have called the reservoir correlations $G_{\alpha\beta}(t)$ in analogy to our nomenclature from chapter 4, as they are the many-site extension of the bath-correlation functions introduced in chapter 4. Now, these complex rates $\Gamma_{\alpha\beta}$ consist of two parts. The imaginary part enters (6.8) in the unitary evolution piece. We define the *Lamb shift* Hamiltonian H_{LS} by

$$H_{LS} = \sum_{\omega} \sum_{\alpha,\beta} S_{\alpha\beta}(\omega) A_{\alpha}^{\dagger}(\omega) A_{\beta}(\omega) \quad (6.11)$$

This name comes from the fact that $[H_S, H_{LS}] = 0$ and thus the Lamb-shift Hamiltonian serves to renormalize the energy levels of the system. This contribution will become very important when we consider the modified superfluid to Mott-insulator transition. The real parts of $\Gamma_{\alpha\beta}$, namely, $\gamma_{\alpha\beta}$ describe the decay rates from various system states to the available bath states. They show

up in (6.8) in the dissipator

$$\mathcal{D}(\hat{\rho}_S) = \sum_{\omega} \sum_{\alpha, \beta} \gamma_{\alpha\beta}(\omega) \left(A_{\beta}(\omega) \hat{\rho}_S A_{\alpha}^{\dagger}(\omega) - \frac{1}{2} \{ A_{\alpha}^{\dagger}(\omega) A_{\beta}(\omega), \hat{\rho}_S \} \right) \quad (6.12)$$

The dissipator (6.12) describes jumps between system states mediated by the traced-out reservoir with rates coming from the reservoir correlations. We note finally that the usual Lindblad form of the master equation is obtained from (6.8) by diagonalization of $\Gamma_{\alpha\beta}(\omega)$.

6.2 Modified superfluid to Mott-insulator transition

As an application of quantum master-equations, we return our attention to the model of section 4.3, namely a single quantum emitter coupled to freely propagating momentum modes. However, with a suitable generalization, we will be able to consider an array of emitters, and the master equation treatment will provide us with a way to predict the phase diagram of the superfluid to Mott-insulator transition in this model. We review very briefly the standard mean-field treatment of the SF-MI phase transition [70, 189, 190] before discussing the modifications which arise due to the coupling to the freely propagating modes.

6.2.1 Standard superfluid Mott-insulator transition

This section summarizes standard textbook treatments of the superfluid to Mott-insulator transition [191]. We consider the Bose-Hubbard model for bosons in a lattice with nearest neighbor tunneling [192, 193]. The Hamiltonian is

$$\hat{H}_{BH} = -J \sum_{\langle i,j \rangle} \hat{a}_i^{\dagger} \hat{a}_j + \sum_i (\epsilon_i - \mu) \hat{a}_i^{\dagger} \hat{a}_i + \frac{U}{2} \sum_i \hat{a}_i^{\dagger} \hat{a}_i^{\dagger} \hat{a}_i \hat{a}_i \quad (6.13)$$

where \hat{a}_i and \hat{a}_i^{\dagger} are bosonic creation and annihilation operators on a site satisfying the usual commutation relations $[\hat{a}_i, \hat{a}_j^{\dagger}] = \delta_{ij}$, J is the tunneling matrix element and U the on-site (contact) interaction parameter obtained in a tight-binding manner, ϵ_i is a site-dependent energy offset corresponding to, e.g. an external harmonic trap or on-site disorder, and μ is the usual chemical potential. Theoretical treatments of the model using Mathieu functions or else Gaussian approximations to the on-site Wannier functions [194] give the

following useful relationships for J and U as a function of s (the depth of the optical lattice in recoils):

$$\frac{J}{E_r} = \frac{4}{\sqrt{\pi}} s^{3/4} e^{-2\sqrt{s}}; \quad \frac{U}{E_r} = \frac{4k a s^{3/4}}{\sqrt{2\pi}}. \quad (6.14)$$

which for U strictly speaking only applies in the case of uniform 3D lattice confinement. (For completeness, k is the wavevector of the optical lattice and a is the s-wave scattering length of the condensate atoms. For ^{87}Rb , $a \approx 100a_{Bohr}$.) Note that the notation $\langle i, j \rangle$ indicates a summation on nearest-neighbor sites only. Introducing the on-site number operator $\hat{n}_i = \hat{a}_i^\dagger \hat{a}_i$, and considering the case of no external potentials or disorder, the Hamiltonian in (6.13) reduces to the form we will consider for computing the Bose-Hubbard phase-diagram, namely

$$\hat{H}_{BH} = -J \sum_{\langle i, j \rangle} \hat{a}_i^\dagger \hat{a}_j - \mu \sum_i \hat{n}_i + \frac{U}{2} \sum_i \hat{n}_i (\hat{n}_i - 1) \quad (6.15)$$

as depicted pictorially in fig. 6.1 Experimentally, we may tune J , U , and μ via

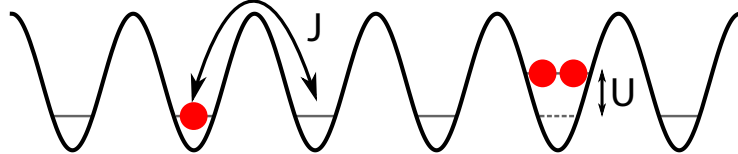


Figure 6.1: Schematic depiction of various terms in the Bose-Hubbard model. Atoms (represented as red circles) in the ground band of a 1-dimensional optical lattice (gray lines) can tunnel between neighboring sites with rate J , and interact on the same site with interaction energy U .

the lattice depth, atomic Feshbach resonances [37], and the total atom number respectively.

In order to understand the phases of this model, we consider the ground states in two limits. First, if $U = 0$, then it will be energetically favorable for the atoms in the lattice to delocalize. Therefore

$$|\psi_{U=0}\rangle = \frac{1}{\sqrt{N}} \left(\frac{1}{\sqrt{N_{latt}}} \sum_{j=1}^{N_{latt}} \hat{a}_j^\dagger \right) |0\rangle = \frac{1}{\sqrt{N}} \hat{a}_{q=0}^\dagger |0\rangle \quad (6.16)$$

We have introduced the notation \hat{a}_q^\dagger which creates a coherent state having quasimomentum q . This state is phase coherent across the whole lattice, and

as such, it represents a superfluid state or a BEC. The other limit we consider is when $J = 0$. Because interactions are so strong, the system now favors localization onto individual sites. Unlike before, however, the specific form of the ground state depends on the number of atoms present. For the case that $N = N_{latt}$ the ground state will just have one atom per site

$$|\psi_{J=0,1}\rangle = \prod_{j=1}^{N_{latt}} \hat{a}_j^\dagger |0\rangle \quad (6.17)$$

and for the case that $N/N_{latt} = \sigma \in \mathbb{Z}$, the ground state has σ atoms per site, and can be written

$$|\psi_{J=0,\sigma}\rangle = \prod_{j=1}^{N_{latt}} \frac{(\hat{a}_j^\dagger)^\sigma}{\sqrt{\sigma!}} |0\rangle \quad (6.18)$$

These states, having a fixed number of particles per site, lack the phase coherence of the superfluid state (6.16). Therefore, they represent a different phase, which is called the Mott-insulator phase. Furthermore, there is no continuous way to deform the Mott-insulator ground state to the superfluid state, so we know that as a function of U and J there must be a transition between the two phases. We note that there is no exact expression for the ground state in general, but we can gain insight into the phase diagram properties by using a mean-field treatment [189, 195, 196].

Let us define the expectation value of the creation and annihilation operators $\langle \hat{a}_j^\dagger \rangle = \langle \hat{a}_j \rangle = \phi$. This quantity, which may be chosen to be a real number value, serves as an order parameter for the Bose-Hubbard model. We now make the mean-field approximation. Specifically, we assume that we can replace the quantum-varying population on each site with a mean-field, and we will attempt to learn about the Bose-Hubbard model by assuming that the atoms can tunnel and interact with this mean field. The form of the mean-field decoupling [189] is

$$\hat{a}_i^\dagger \hat{a}_j \approx \phi \hat{a}_j + \hat{a}_i^\dagger \phi - \phi^2 \quad (6.19)$$

and thus the tunneling term takes the form

$$\hat{H}_J \approx -zJ \left[\sum_j (\hat{a}_j^\dagger + \hat{a}_j)\phi - \phi^2 \right] \quad (6.20)$$

where we have defined z , the coordination number, as the number of nearest neighbors of site j . For example, in a simple cubic lattice in 1, 2, and 3 dimensions, $z = 2, 4$, and 6 respectively.

If we now define $\bar{U} = U/zJ$ and $\bar{\mu} = \mu/zJ$ we can cast our mean-field Hamiltonian as a sum of single site Hamiltonians in the following manner:

$$\hat{H}_{mf} = zJ \sum_j (h'_j + H_j^0) \quad (6.21)$$

with

$$H_j^0 = \phi^2 + \frac{\bar{U}}{2} \hat{n}_j (\hat{n}_j - 1) - \bar{\mu} \hat{n}_j \quad (6.22)$$

and

$$h'_j = -\phi (\hat{a}_j^\dagger + \hat{a}_j) \quad (6.23)$$

We have split (6.21) into two parts: an unperturbed Hamiltonian (6.22) which is diagonalized in the basis of states $|n\rangle$ with a fixed number n of particles on every site, and (6.23) which acts as a perturbation in this basis.

By applying standard perturbation theory one finds [189, 191]

$$E_n^{(0)} = \begin{cases} 0 & \mu < 0 \\ \frac{\bar{U}}{2} n(n-1) - \bar{\mu} n & U(n-1) < \mu < Un \end{cases} \quad (6.24)$$

for the unperturbed energies [189, 191], $E_n^{(1)} = 0$, and

$$E_n^{(2)} = \sum_{n \neq n'} \frac{|\langle n | \phi(\hat{a}^\dagger + \hat{a}) | n' \rangle|^2}{E_n^{(0)} - E_{n'}^{(0)}} = \frac{\phi^2 n}{\bar{U}(n-1) - \bar{\mu}} + \frac{\phi^2 (n+1)}{\bar{\mu} - \bar{U}n} \quad (6.25)$$

The ground state energy to this order in perturbation theory is then (as a function of the mean-field order parameter ϕ)

$$E_n(\phi) = E_n^{(0)} + zJ \left(\frac{n}{\bar{U}(n-1) - \bar{\mu}} + \frac{n+1}{\bar{\mu} - \bar{U}n} + 1 \right) \phi^2 + \dots \quad (6.26)$$

Now, in the ground state, the energy will be a minimum, so we minimize (6.26) with respect to the order parameter ϕ . The first term is independent of ϕ , and therefore the minimization only depends on the term proportional to ϕ^2 . The term in parentheses determines the behavior of ϕ in the ground state. If the term in parentheses is positive, (6.26) is minimized by taking $\phi = 0$, which we interpret to be the Mott-insulating phase since there will not be phase coherence across the system in this state. If however the coefficient of ϕ^2 in (6.26) is negative, then we can minimize the ground state energy by taking $\phi^2 > 0$, which is to say the mean-field order parameter becomes non-zero and the system will develop phase coherence, so we may identify this phase with

the superfluid state. The boundary between these two phases is found when the coefficient of ϕ^2 is equal to zero, so we can solve for the phase boundary. The result is [189, 191]

$$\frac{zJ}{U} = \frac{(\mu/U - n)(\mu/U - n + 1)}{\mu/U + 1} \quad (6.27)$$

This classic result has informed much theoretical and experimental effort on the Bose-Hubbard model [41, 197]. The phase diagram, c.f. fig. 6.2(A), takes the form of lobes of Mott-insulating phase having fixed number of particles surrounded by lobes of superfluid for which n is not a good quantum number, but which has a coherent phase.

The preceding description is modified in the presence of an external trapping potential. As in an experiment, consider a roughly harmonic trapping potential $V(x) \propto x^2$. Then the term ϵ_i in (6.13) plays a role, and we replace μ by $\mu_i = \mu - \epsilon_i$ a site dependent chemical potential in (6.15). The result due to a spatially varying chemical potential is that the model now supports regions of fixed n Mott-insulating phase surrounded by rings of superfluid phase in the celebrated wedding cake structure [198, 199]. This structure was observed in a spatially resolved way starting in 2006 [199] in the group of Wolfgang Ketterle using spectroscopic methods, and later in 2009 [200]. The realization of quantum gas microscopy [61, 63] provided an even more transparent method for viewing the wedding cake structure experimentally. We note that even if we do not have spatial resolution of the wedding cake structure, we can still access the different Mott-insulating lobes by careful spectroscopic measurements following the technique of the Ketterle group [199], c.f. the thesis of L. Krinner [172].

6.2.2 The SF-MI transition with long-range tunneling

Here, we follow the same steps [112, 122] to derive a Markovian quantum master equation and effective tunneling model at negative detunings for our 1D emitter system. Then as an interesting extension, we show how the previously considered superfluid to Mott-insulator phase transition is modified in this effective model. We will find that the previously discussed mean-field treatment applies with one key modification: the effective coordination z^* will be modified by the coupling to the bath of propagating states.

Consider the model of section 4.3, in which a single red emitter in the excited state is initially coupled to a continuum of blue freely-propagating momentum modes. If we now consider multiple red emitters located on the sites

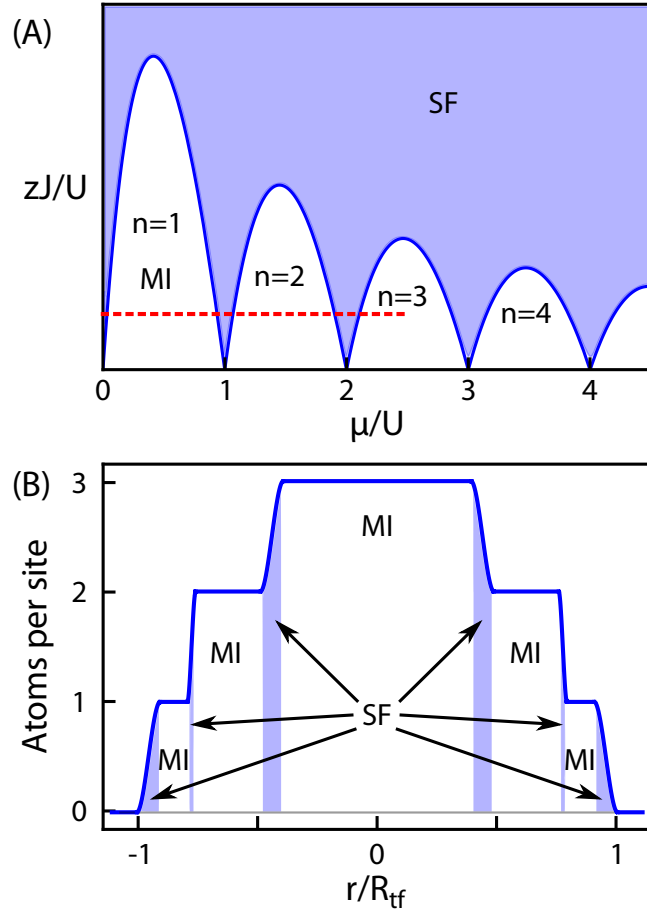


Figure 6.2: Various features of the Superfluid to Mott-Insulator phase transition. (A) Phase diagram in the mean field treatment. The shaded area represents parameter combinations that yield a superfluid (coherent) phase across the condensate in an optical lattice, while the white lobes represent Mott-insulating phases of fixed atom number per site n , with the first 4 Mott-lobes fully shown. The phase boundary is determined by (6.27). (B) Illustration of the wedding-cake structure of a harmonically trapped condensate having $N = 150,000$ atoms in a Harmonic trap of trap frequency $\omega = 2\pi \times 60$ Hz. The calculation assumes a 3D square lattice ($z = 6$) at $\lambda = 1064$ nm and a depth of $25 E_r$. The chemical potential is computed as a function of distance from the trap center in the Thomas-Fermi approximation, and it corresponds to the red dashed line in (A).

j of an optical lattice, we must modify the Hamiltonian (4.9) as follows:

$$\hat{H}_I = \sum_j \sum_k \frac{\hbar\Omega}{2} \gamma_k e^{-i\Delta_k t - ikr_j} \hat{b}_k^\dagger |0_j\rangle \langle 1_j| + H.c. \quad (6.28)$$

which now contains a sum over red sites j and where $r_j = d_0 \times j$ is the position of red emitter j in terms of the lattice spacing d_0 .

The quantities of interest in a master-equation treatment are the complex Markovian rates Γ_{jl} , defined by (6.10). For our system, we may compute these quantities as follows:

$$\begin{aligned} G_{jl}(\tau) &= \frac{1}{\hbar^2} \sum_k g_k^2 \exp(-i\Delta_k \tau - ikr_{j-l}) \langle \hat{b}_k^\dagger \hat{b}_k \rangle \\ &\approx \lim_{\varepsilon \rightarrow 0} \frac{1}{\hbar^2} \sum_k g_k^2 \exp(-(\varepsilon + i\Delta_k) \tau - ikr_{j-l}) \end{aligned} \quad (6.29)$$

where we have approximated $\langle \hat{b}_k^\dagger \hat{b}_k \rangle \approx 1$, valid only in the Born-Markov regime, and we have introduced an epsilon-regulator to ensure the convergence of the integral over τ which we must compute in order to determine Γ_{jl} . Specifically

$$\Gamma_{jl} = \int_0^\infty G_{jl}(\tau) d\tau = \lim_{\varepsilon \rightarrow 0^+} \sum_k \frac{g_k^2}{\hbar^2} \frac{e^{ikr_{j-l}}}{\varepsilon + i\Delta_k} \quad (6.30)$$

which is very reminiscent of our Markovian limit treatment of this emitter system in section 4.3.3. Taking a continuum limit for the k -summation in (6.30), and utilizing the definitions of $g_k = \hbar\Omega\gamma_k/2$ and $\Delta_k = \hbar k^2/2m - \Delta$, we find

$$\Gamma_{jl} = \lim_{\varepsilon \rightarrow 0^+} \frac{(\Omega/2)^2 a_{ho}}{\sqrt{\pi}} \int_{-\infty}^\infty \frac{e^{-k^2 a_{ho}^2} e^{-ikr_{j-l}}}{\varepsilon + i\Delta_k} dk \quad (6.31)$$

or, upon defining a change of variables $\kappa = ka_{ho}$

$$\Gamma_{jl} = \lim_{\varepsilon \rightarrow 0} \frac{(\Omega/2)^2}{\sqrt{\pi}} \int_{-\infty}^\infty \frac{e^{-\kappa^2} e^{-i\kappa d_0(j-l)/a_{ho}}}{\varepsilon + i\omega_0 \kappa^2/2 - i\Delta} d\kappa \quad (6.32)$$

This integral is intractable in general, but we note that for the limit of strong confinement, $\omega_0 \gg \Omega, \Delta$ and any other energy scale, we may approximate the gaussian term in the numerator of (6.32) as 1, $\exp(-\kappa^2) \approx 1$, whereupon

$$\Gamma_{jl} \approx \lim_{\varepsilon \rightarrow 0} \frac{(\Omega/2)^2}{\sqrt{\pi}} \int_{-\infty}^\infty \frac{e^{-i\kappa d_0(j-l)/a_{ho}}}{\varepsilon + i\omega_0 \kappa^2/2 - i\Delta} d\kappa \quad (6.33)$$

which may be integrated to yield

$$\Gamma_{jl} = -i \frac{\delta_L}{2} \sqrt{\frac{\pi \omega_0}{-2\Delta}} \exp\left(-\frac{d_0}{a_{ho}} \sqrt{\frac{-2\Delta}{\omega_0}} |j - l|\right) \quad (6.34)$$

By inspection, this result depends upon the sign of the detuning, Δ , so we define the following auxiliary functions [112, 122]:

$$\nu = \begin{cases} 1 & \Delta < 0 \\ i & \Delta > 0 \end{cases} \quad (6.35)$$

which keeps track of the complex analytic character of the rates Γ_{jl} as a function of the sign of the detuning,

$$\Gamma_0(\Delta) = \frac{\delta_L}{2} \sqrt{\frac{\pi\omega_0}{2|\Delta|}} \quad (6.36)$$

which determines the strength of the couplings ($\delta_L = \Omega^2/\omega_0$ as before), and

$$\xi(\Delta) = a_{ho} \sqrt{\frac{\omega_0}{2|\Delta|}} \quad (6.37)$$

which determines the effective range (in lattice sites) of the effective tunneling term. With these definitions, the Markov master equation rates become

$$\Gamma_{jl}(\Delta) = -\frac{i}{\nu} \Gamma_0(\Delta) \exp\left(-\nu \frac{d_0}{\xi(\Delta)} |j-l|\right) \quad (6.38)$$

We note that importantly, for $\Delta < 0$, (6.38) is a purely imaginary quantity. This means that for negative detunings, the master equation for the reduced density matrix of red emitters consists *only of the coherent, Lamb-shift term* with dissipator identically equal to zero! (Recall equations (6.7), (6.8) and (6.11).)

We are thus led to the following model: we are considering a lattice of red emitters in deeply confining wells of an optical lattice (harmonic oscillator frequency ω_0 much greater than any other energy scale) in one dimension. Due to this strong confinement, the atoms will not tunnel directly, so effectively, their Hamiltonian consists only of the on-site and chemical potential terms in the Bose-Hubbard model. After we turn on the coupling, the atoms acquire, through the traced out blue momentum states, a tunneling term of the form

$$\hat{H}_{tunnel} = - \sum_{j,l} J_{jl} \hat{a}_j^\dagger \hat{a}_l \quad (6.39)$$

with

$$J_{jl} = \hbar \Gamma_0 \exp\left(-\frac{d_0}{\xi} |j-l|\right) \quad (6.40)$$

Therefore, the new *effective* Hamiltonian for this model becomes

$$\hat{H}_{LRT} = -\hbar\Gamma_0 \sum_{i,j} \exp^{-d_0|i-j|/\xi} \hat{a}_i^\dagger \hat{a}_j - \mu \sum_i \hat{n}_i + \frac{U}{2} \sum_i \hat{n}_i(\hat{n}_i - 1) \quad (6.41)$$

We now proceed as before and make a mean-field decoupling of the tunneling term, i.e. we replace $\langle \hat{a}_j \rangle = \langle \hat{a}_j^\dagger \rangle = \phi$. For a fixed site index j , we consider the following change of notation: let $r(j) = r = j - l$, and

$$J_r = \hbar\Gamma_0 \exp(-d_0|r|/\xi) \quad (6.42)$$

The mean-field decoupling of the tunneling term now takes the form for a fixed site i

$$\hat{H}_{tunnel} \approx -\hbar\Gamma_0 \sum_r \exp(-d_0|r|/\xi) (\hat{a}_j + \hat{a}_j^\dagger) \phi \quad (6.43)$$

Thus the mean field Hamiltonian of the model again decouples as a sum upon single site Hamiltonians of the form $\hat{H}_{LRT}^{MF} = \sum_j \hat{H}_j^{MMF}$ (here MMF stands for Modified Mean Field) with

$$\hat{H}_j^{MMF} = -\mu \hat{n}_j + \frac{U}{2} \hat{n}_j(\hat{n}_j - 1) - \hbar\Gamma_0 \sum_r \exp^{-d_0|r|/\xi} (\hat{a}_j + \hat{a}_j^\dagger) \phi \quad (6.44)$$

We may simply carry out the r summation in (6.44), and if we identify $J_{eff} = \hbar\Gamma_0$, then we may identify the r dependent parts above as an effective coordination number z^* . What we find is that

$$z^* = \sum_r \exp\left(\frac{-d_0|r|}{\xi}\right) = \coth\left(\frac{d_0}{2\xi}\right) \quad (6.45)$$

such that the mean field Hamiltonian reduces to the same form as the mean field Hubbard model, provided we replace zJ by z^*J_{eff} . Then all of the preceding computations from section 6.2 carry over unchanged, so we obtain the same phase diagram (when plotted as a function of μ/U vs. z^*J_{eff}/U). We note, however, that because in 1D, $z = 2$, if $\xi \geq 1$, $z^* \geq 2.16$, so the real physical values at which the lobes occur do shift with respect to the nearest neighbor model. This can potentially have observable experimental consequences, c.f. fig. 6.3. We note also that the effective coordination number can be less than 2, i.e. when $\xi \ll d_0$, the excitations in the quantum emitters cannot hop to their neighbors, and the model is effectively *less* able to tunnel than a standard 1D lattice.

A simple experiment to check for this shift in the Mott-insulator transition

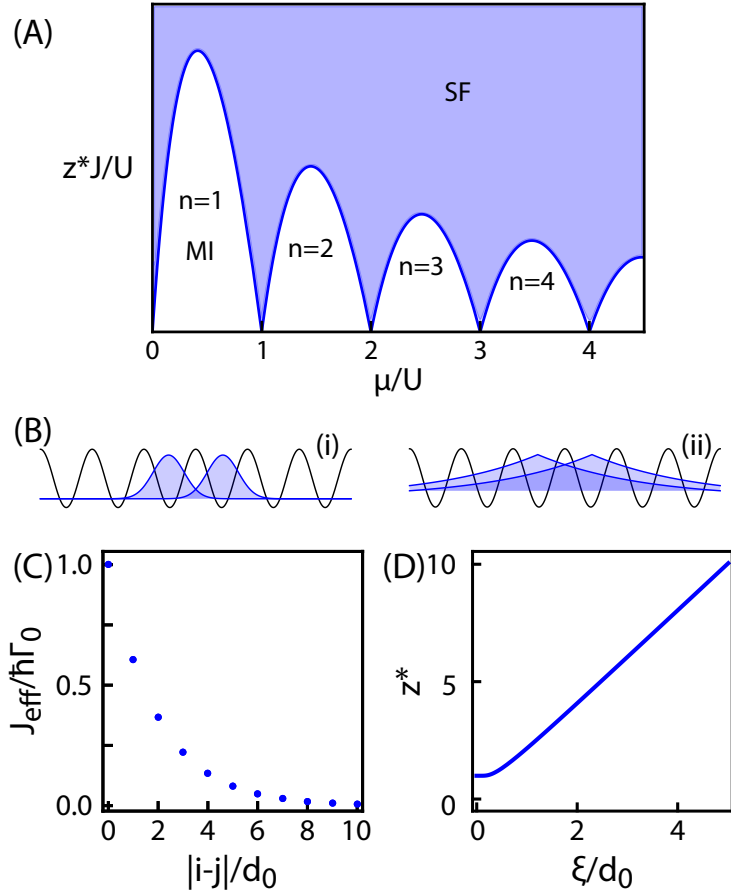


Figure 6.3: Modifications to the superfluid to Mott-insulator transition in the effective Hamiltonian model of (6.41). (A) Phase diagram in the mean field treatment. The only different from fig. 6.2(A) is that the vertical axis is scaled by z^* instead of z . (B) Illustrations of cases where (i) $z^* = 2$ for a typical optical lattice experiment and (ii) $z^* = 4.08$ for the effective model having $\xi = 2d_0$. (C) Effective tunneling rate for sites i and j separated by integer multiples of the lattice spacing d_0 , assuming $\xi = 2d_0$. (D) Effective coordination number z^* as a function of ξ/d_0 in the 1D system. The tunability of the system allows for a 1D system having $z^* \geq 1$, i.e. we can tune the effective dimensionality of the system while remaining fully 1D.

would start with a deep $n = 1$ Mott insulating state in a state selective optical potential. (For concreteness, we consider as the trapped state ^{87}Rb 's $F = 1$ hyperfine ground state $|r\rangle = |1, -1\rangle$ in an sE_{rec} lattice along z and the untrapped state $|b\rangle = |2, 0\rangle$ as in chapter 5, both subject to $40E_{\text{rec}}$ tubes in

x and y .) Applying a coupling microwave field at negative detuning creates bound states which leads to the effective tunneling Hamiltonian considered here, and whose decay length ξ is given as a function of Δ . Applying this radiation as a function of s should show the transition from superfluid to a Mott insulator at a different value than for the uncoupled case. Using a peak width measurement or contrast measurement, one would look for the point at which the transition occurs as a function of s for several values of ξ and then compare to the predictions of (6.45) (see [201] for a treatment with truly long-range tunneling.)

A further experiment of interest might be described as “purification of a Mott-Insulator via bound state formation”. The set-up we consider is now a Mott-Insulating phase in a harmonic trap having distinct lobes of differing atom number. The goal is to create a uniform $n = 1$ Mott-Insulator across the whole sample. Because the interaction shift on each site is number-dependent as $E(n) = Un(n - 1)/2$, the resonance condition will be shifted for sites of different atom number. If we denote the splitting between the $n = 1$ red emitter and the zero energy blue propagating state by $\Delta = \Delta_1$, then for a fixed microwave detuning of Δ_1 , the other sites will have detuning $\Delta_n = \Delta_1 + E(n) > \Delta_1$, c.f. fig. 6.4. We now propose the following method to bring the Mott-Insulator to a uniform filling of $n = 1$.

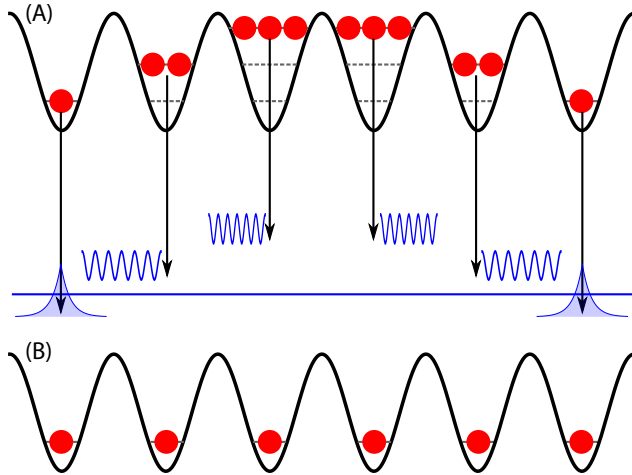


Figure 6.4: Purification scheme for a Mott-insulator having shell structure. (A) Purification scheme based on on-site energy shifts for sites having more than one atom. For a properly chosen detuning ramp, highly occupied sites can be sequentially emptied until they reach unity occupation, (B) resulting in a Mott-insulator with $\langle n_i \rangle \leq 1$. See text for details.

First, we will create a Mott-Insulator with a large number of atoms, and

thus, a large maximal site occupancy of, e.g. $n_{max} = 7$. Two-photon spectroscopy of this Mott-Insulator will reveal the relative populations at each filling fraction [199]. Then, we will choose a detuning such that the maximal site-occupation is nearly resonant with the propagating states, i.e. $\Delta_{initial} \approx \Delta_{n_{max}} = 0$. The sites with $n = n_{max}$ will lose one atom into a propagating state which can escape the system. Next, the microwave detuning will be decreased so that approximately $\Delta_{n_{max}-1} = 0$, removing another atom from all sites having $n = n_{max} - 1$. This process, which is akin to evaporative cooling, is then repeated until we are left with $n = 1$ everywhere. Specifically, for all detunings chosen to remove atoms from highly occupied states, $\Delta_1 < 0$, and thus the singly occupied sites form bound states only. These atoms will not escape the system, and by an adiabatic turn off of the coupling pulse, will be returned to their initial emitter states. A 2-photon spectroscopic measurement after the detuning-ramp procedure should reveal a lower average occupation number n in the lattice, which serves to cool or remove entropy from the system.

We note two practical experimental concerns with regard to this proposed experiment. First: the emitted blue atoms need to be able to escape the system. The current experimental set-up utilizing vertical lattice tubes with harmonic confinement along the tubes does not truly allow the blue atoms to escape. However, by utilizing horizontal tubes formed from blue-detuned light at, e.g. 532 nm, we could create “anti-confining” tubes in the sense that the trapped atoms would tend to seek low intensity regions, and thus, could roll out of the tubes and be lost from the system. We do not yet have the capacity to produce such horizontal tubes, though we note experimental efforts are underway to construct such a lattice using an accordion lattice geometry [202, 203]. Second: the state-selective light scatters many photons from the trapped atoms, with rate $\Gamma \approx 4 \text{ s}^{-1}$ (for $|r\rangle = |1, -1\rangle$ atoms at $\lambda = 790.0 \text{ nm}$), which leads to heating and an overall loss of signal. For our previously discussed experiments, this is not a problem, as the timescales involved are all shorter than the scattering time from the state selective light. However, the proposed 2-photon spectroscopy is slow, requiring times on the order of 100 ms for 1 Hz resolution, which now runs the risk of being on a similar time scale to $1/\Gamma_{SDOL}$. This problem in principle is harder to solve, though we note that in-situ microscopy of the trapped cloud could lead to direct imaging of the Mott-Insulator shells (up to parity) [61, 63]. Overcoming these challenges is an area of active effort in our lab, and the rich physics of our emitter-reservoir systems in a many-body context remains an exciting area of study.

Chapter 7

Conclusion

Having reached the nominal end to this work, we hope to have convinced the reader of both the theoretical richness in and the experimental excitement enabled by the emission of matter waves from quantum emitters into engineered reservoirs. First, we showed how to understand the spontaneous emission of photons from an excited atom in free space as a toy open quantum system, and then we considered extensions of the model in two ways: replacing photons with matter waves and changing the properties of the emitted matter-wave states. A full theoretical characterization of the emission of freely propagating matter waves in one-dimension showed a strong Markovian to non-Markovian evolution of the emitter population, and we also characterized the momentum space profiles of the emitted radiation, with an eye towards an ultracold atomic realization in the laboratory. Excitingly, the system was also shown to exhibit the long predicted “atom-photon bound state”, whose spatial profile and decay length we compute. Then we considered the case of quantum emitters coupled to a band structure, in which the modifications to the dynamics are predicted to be stronger than for a single energetic edge. The dynamics were shown to be tunable between exponential decay and Rabi-oscillations, allowing us to study the novel intermediate regime. A second bound state was predicted, living above the band, whose spatial shape is strongly modified by the lattice.

We then described in detail how to implement a system of matter-wave emitters in the lab using state-dependent optical potentials. We reported on experiments on emission into 1D free-space, obtaining good agreement with the theoretical models previously considered, and accounted for discrepancies between the observed data and the models by appealing to a breakdown of the isolated emitter assumption. Furthermore, we observed directly the shape of the emitter and matter-wave bound state for the first time. We then modified the emission platform to add a lattice for the emitted radiation and demon-

strated how the relative strength of coupling to the bath of modes allowed us to tune between fully Markovian (open) decays and fully coherent (closed) Rabi oscillations, all while also being able to access the intermediate regime. We furthermore demonstrated the existence of two bound states and showed that their momentum composition is strongly dependent upon which band-edge they couple to. Furthermore, the observed oscillations are shown to be consistent with a beating between the bound states in the system!

Going forward, we have shown how our emitter platform may be used to study many-body effects. In particular, via the machinery of quantum master equations [112], we showed how to derive an effective Hamiltonian with beyond nearest neighbor tunneling, and we showed how this can modify, for example, the superfluid to Mott-insulator transition in our system. We then gave an example of how this novel system might allow for experiments on cooling of a Mott-insulating phase. We also can use the quantum emitter system to study the formation dynamics of bound states, as well as attempt to study their transport properties through tilted optical lattices. Though we did not consider it in this thesis, the emitter platform is also predicted to exhibit superradiance [112, 204], which we seek to study in future work. Finally, we can study higher dimensional analogues of our platform [115–118], in which exotic behaviors beyond the scope of our current work are predicted.

Given the exciting directions in quantum simulation that the Schnable lab can explore, I am excited to see the future directions of this work.

Bibliography

- [1] L.D. Landau and E.M. Lifshitz. *Statistical Physics: Part 1*. Butterworth-Heinemann, Oxford, 1951.
- [2] S. N. Bose. Plancks Gesetz und Lichtquantenhypothese. *Z. Phys.*, 26: 178–181, 1924.
- [3] A. Einstein. Quantentheorie des einatomigen idealen Gases. *Sitzungsber. Preuss. Akad.*, pages 261–267, 1924.
- [4] F. Dalfovo, S. Giorgini, L. P. Pitaevskii, and S. Stringari. Theory of Bose–Einstein condensation in trapped gases. *Rev. Mod. Phys.*, 71:463–512, 1999.
- [5] M. H. Anderson, J. R. Ensher, M. R. Matthews, C. E. Wieman, and E. A. Cornell. Observation of Bose–Einstein condensation in a dilute atomic vapor. *Science*, 269:198–201, 1995.
- [6] C. C. Bradley, C. A. Sackett, J. J. Tollett, and R. G. Hulet. Evidence of Bose–Einstein condensation in an atomic gas with attractive interactions. *Phys. Rev. Lett.*, 75:1687–1690, 1995.
- [7] C. C. Bradley, C. A. Sackett, and R. G. Hulet. Bose–Einstein condensation of lithium: Observation of limited condensate number. *Phys. Rev. Lett.*, 78:985–989, 1997.
- [8] K. B. Davis, M. O. Mewes, M. R. Andrews, N. J. van Druten, D. S. Durfee, D. M. Kurn, and W. Ketterle. Bose–Einstein condensation in a gas of sodium atoms. *Phys. Rev. Lett.*, 75:3969–3973, 1995.
- [9] Enrico Fermi. Zur Quantelung des idealen einatomigen Gases. *Zeitschrift für Physik*, 36(11-12):902–912, 1926.
- [10] Paul Adrien Maurice Dirac. On the theory of quantum mechanics. *Proceedings of the Royal Society of London A*, 112(762):661–677, 1926.

- [11] S. Giorgini, L. P. Pitaevskii, and S. Stringari. Theory of ultracold atomic Fermi gases. *Rev. Mod. Phys.*, 80:1215–1274, 2008.
- [12] B. DeMarco and D. S. Jin. Onset of Fermi degeneracy in a trapped atomic gas. *Science*, 285:1703–1706, 1999.
- [13] MR Andrews, CG Townsend, H-J Miesner, DS Durfee, DM Kurn, and W Ketterle. Observation of interference between two Bose condensates. *Science*, 275(5300):637–641, 1997.
- [14] M-O Mewes, MR Andrews, DM Kurn, DS Durfee, CG Townsend, and W Ketterle. Output coupler for Bose-Einstein condensed atoms. *Physical Review Letters*, 78(4):582, 1997.
- [15] Immanuel Bloch, Theodor W Hänsch, and Tilman Esslinger. Atom laser with a cw output coupler. *Physical Review Letters*, 82(15):3008, 1999.
- [16] Edward W Hagley, Lu Deng, M Kozuma, J Wen, Kristian Helmerson, SL Rolston, , and William D Phillips. A well-collimated quasi-continuous atom laser. *Science*, 283(5408):1706–1709, 1999.
- [17] S. Inouye, A. P. Chikkatur, D. M. Stamper-Kurn, J. Stenger, D. E. Pritchard, and W. Ketterle. Superradiant Rayleigh scattering from a Bose-Einstein condensate. *Science*, 285:571, 1999.
- [18] D. Schneble, Y. Torii, M. Boyd, E. W. Streed, D. E. Pritchard, and W. Ketterle. The onset of matter-wave amplification in a superradiant Bose-Einstein condensate. *Science*, 300:457, 2003.
- [19] M-O Mewes, MR Andrews, NJ Van Druten, DM Kurn, DS Durfee, CG Townsend, and W Ketterle. Collective excitations of a Bose-Einstein condensate in a magnetic trap. *Physical Review Letters*, 77(6):988, 1996.
- [20] MR Andrews, DM Kurn, H-J Miesner, DS Durfee, CG Townsend, S Inouye, and W Ketterle. Propagation of sound in a Bose-Einstein condensate. *Physical Review Letters*, 79(4):553, 1997.
- [21] S Burger, K Bongs, S Dettmer, W Ertmer, K Sengstock, A Sanpera, GV Shlyapnikov, and M Lewenstein. Dark solitons in Bose-Einstein condensates. *Physical Review Letters*, 83(25):5198, 1999.
- [22] Kevin E Strecker, Guthrie B Partridge, Andrew G Truscott, and Randall G Hulet. Formation and propagation of matter-wave soliton trains. *Nature*, 417(6885):150, 2002.

- [23] C Raman, M Köhl, R Onofrio, DS Durfee, CE Kuklewicz, Z Hadzibabic, and W Ketterle. Evidence for a critical velocity in a Bose-Einstein condensed gas. *Physical Review Letters*, 83(13):2502, 1999.
- [24] R Onofrio, C Raman, JM Vogels, JR Abo-Shaeer, AP Chikkatur, and W Ketterle. Observation of superfluid flow in a Bose-Einstein condensed gas. *Physical Review Letters*, 85(11):2228, 2000.
- [25] Dale G Fried, Thomas C Killian, Lorenz Willmann, David Landhuis, Stephen C Moss, Daniel Kleppner, and Thomas J Greystak. Bose-Einstein condensation of atomic hydrogen. *Physical Review Letters*, 81(18):3811, 1998.
- [26] Alice Robert, Olivier Sirjean, Antoine Browaeys, Julie Poupard, Stephan Nowak, Denis Boiron, Christoph I Westbrook, and Alain Aspect. A Bose-Einstein condensate of metastable atoms. *Science*, 292(5516):461–464, 2001.
- [27] Giovanni Modugno, Gabriele Ferrari, Giacomo Roati, Robert J Brecha, A Simoni, and Massimo Inguscio. Bose-Einstein condensation of potassium atoms by sympathetic cooling. *Science*, 294(5545):1320–1322, 2001.
- [28] Tino Weber, Jens Herbig, Michael Mark, Hanns-Christoph Nägerl, and Rudolf Grimm. Bose-Einstein condensation of cesium. *Science*, 299(5604):232–235, 2003.
- [29] Axel Griesmaier, Jörg Werner, Sven Hensler, Jürgen Stuhler, and Tilman Pfau. Bose-Einstein condensation of chromium. *Physical Review Letters*, 94(16):160401, 2005.
- [30] Sebastian Kraft, Felix Vogt, Oliver Appel, Fritz Riehle, and Uwe Sterr. Bose-Einstein condensation of alkaline earth atoms: Ca 40. *Physical Review Letters*, 103(13):130401, 2009.
- [31] Simon Stellmer, Meng Khoon Tey, Bo Huang, Rudolf Grimm, and Florian Schreck. Bose-Einstein condensation of strontium. *Physical Review Letters*, 103(20):200401, 2009.
- [32] YN Martinez De Escobar, Pascal Gerry Mickelson, M Yan, BJ DeSalvo, Sarah B Nagel, and TC Killian. Bose-Einstein Condensation of Sr 84. *Physical Review Letters*, 103(20):200402, 2009.
- [33] Yosuke Takasu, Kenichi Maki, Kaduki Komori, Tetsushi Takano, Kazuhito Honda, Mitsutaka Kumakura, Tsutomu Yabuzaki, and Yoshiro

- Takahashi. Spin-singlet Bose-Einstein condensation of two-electron atoms. *Physical Review Letters*, 91(4):040404, 2003.
- [34] K Aikawa, A Frisch, M Mark, S Baier, A Rietzler, R Grimm, and F Ferlaino. Bose-Einstein condensation of erbium. *Physical Review Letters*, 108(21):210401, 2012.
 - [35] Mingwu Lu, Nathaniel Q Burdick, Seo Ho Youn, and Benjamin L Lev. Strongly dipolar Bose-Einstein condensate of dysprosium. *Physical Review Letters*, 107(19):190401, 2011.
 - [36] S Inouye, MR Andrews, J Stenger, H-J Miesner, DM Stamper-Kurn, and W Ketterle. Observation of Feshbach resonances in a Bose-Einstein condensate. *Nature*, 392(6672):151, 1998.
 - [37] C. Chin, R. Grimm, P. Julienne, and E. Tiesinga. Feshbach resonances in ultracold gases. *Rev. Mod. Phys.*, 82:1225–1286, 2010.
 - [38] Yu. B. Ovchinnikov, J. H. Müller, M. R. Doery, E. J. D. Vredenbregt, K. Helmerson, S. L. Rolston, and W. D. Phillips. Diffraction of a released Bose-Einstein condensate by a pulsed standing light wave. *Phys. Rev. Lett.*, 83:284–287, 1999.
 - [39] O. Morsch and M. Oberthaler. Dynamics of Bose-Einstein condensates in optical lattices. *Rev. Mod. Phys.*, 78:179–215, 2006.
 - [40] J. Hubbard and Brian Hilton Flowers. Electron correlations in narrow energy bands. *Proceedings of the Royal Society of London. Series A. Mathematical and Physical Sciences*, 276(1365):238–257, 1963. doi: 10.1098/rspa.1963.0204.
 - [41] M. Greiner, O. Mandel, T. Esslinger, T. W. Hänsch, and I. Bloch. Quantum phase transition from a superfluid to a Mott insulator in a gas of ultracold atoms. *Nature*, 415:39, 2002.
 - [42] Patrick Windpassinger and Klaus Sengstock. Engineering novel optical lattices. *Reports on Progress in Physics*, 76(8):086401, jul 2013. doi: 10.1088/0034-4885/76/8/086401.
 - [43] Omjyoti Dutta, Mariusz Gajda, Philipp Hauke, Maciej Lewenstein, Dirk-Sören Lühmann, Boris A Malomed, Tomasz Sowiński, and Jakub Zakrzewski. Non-standard hubbard models in optical lattices: a review. *Reports on Progress in Physics*, 78(6):066001, may 2015. doi: 10.1088/0034-4885/78/6/066001.

- [44] Thomas Uehlinger, Gregor Jotzu, Michael Messer, Daniel Greif, Walter Hofstetter, Ulf Bissbort, and Tilman Esslinger. Artificial graphene with tunable interactions. *Phys. Rev. Lett.*, 111:185307, Oct 2013. doi: 10.1103/PhysRevLett.111.185307. URL <https://link.aps.org/doi/10.1103/PhysRevLett.111.185307>.
- [45] Gregor Jotzu, Michael Messer, Rémi Desbuquois, Martin Lebrat, Thomas Uehlinger, Daniel Greif, and Tilman Esslinger. Experimental realization of the topological Haldane model with ultracold fermions. *Nature*, 515(7526):237, 2014.
- [46] L. Duca, T. Li, M. Reitter, I. Bloch, M. Schleier-Smith, and U. Schneider. An aharonov-bohm interferometer for determining bloch band topology. *Science*, 347(6219):288–292, 2015. ISSN 0036-8075. doi: 10.1126/science.1259052. URL <https://science.sciencemag.org/content/347/6219/288>.
- [47] K. Singh, K. Saha, S. A. Parameswaran, and D. M. Weld. Fibonacci optical lattices for tunable quantum quasicrystals. *Phys. Rev. A*, 92: 063426, Dec 2015. doi: 10.1103/PhysRevA.92.063426. URL <https://link.aps.org/doi/10.1103/PhysRevA.92.063426>.
- [48] Konrad Viebahn, Matteo Sbroscia, Edward Carter, Jr-Chiun Yu, and Ulrich Schneider. Matter-wave diffraction from a quasicrystalline optical lattice. *Phys. Rev. Lett.*, 122:110404, Mar 2019. doi: 10.1103/PhysRevLett.122.110404. URL <https://link.aps.org/doi/10.1103/PhysRevLett.122.110404>.
- [49] Daniel Greif, Thomas Uehlinger, Gregor Jotzu, Leticia Tarruell, and Tilman Esslinger. Short-range quantum magnetism of ultracold fermions in an optical lattice. *Science*, 340(6138):1307–1310, 2013.
- [50] Russell A Hart, Pedro M Duarte, Tsung-Lin Yang, Xinxing Liu, Thereza Paiva, Ehsan Khatami, Richard T Scalettar, Nandini Trivedi, David A Huse, and Randall G Hulet. Observation of antiferromagnetic correlations in the Hubbard model with ultracold atoms. *Nature*, 519(7542):211, 2015.
- [51] Anton Mazurenko, Christie S Chiu, Geoffrey Ji, Maxwell F Parsons, Márton Kanász-Nagy, Richard Schmidt, Fabian Grusdt, Eugene Demler, Daniel Greif, and Markus Greiner. A cold-atom Fermi-Hubbard antiferromagnet. *Nature*, 545(7655):462, 2017.

- [52] Timon A Hilker, Guillaume Salomon, Fabian Grusdt, Ahmed Omran, Martin Boll, Eugene Demler, Immanuel Bloch, and Christian Gross. Revealing hidden antiferromagnetic correlations in doped Hubbard chains via string correlators. *Science*, 357(6350):484–487, 2017.
- [53] Peter T Brown, Debayan Mitra, Elmer Guardado-Sanchez, Peter Schauß, Stanimir S Kondov, Ehsan Khatami, Thereza Paiva, Nandini Trivedi, David A Huse, and Waseem S Bakr. Spin-imbalance in a 2D Fermi-Hubbard system. *Science*, 357(6358):1385–1388, 2017.
- [54] Y.-J. Lin, K. Jiménez-Garcia, and I. B. Spielman. Spin-orbit-coupled Bose-Einstein condensates. *Nature*, 471:83–86, 2011.
- [55] Victor Galitski and Ian B Spielman. Spin-orbit coupling in quantum gases. *Nature*, 494(7435):49, 2013.
- [56] Lianghui Huang, Zengming Meng, Pengjun Wang, Peng Peng, Shao-Liang Zhang, Liangchao Chen, Donghao Li, Qi Zhou, and Jing Zhang. Experimental realization of two-dimensional synthetic spin-orbit coupling in ultracold Fermi gases. *Nature Physics*, 12(6):540, 2016.
- [57] Monika Aidelsburger, Marcos Atala, Michael Lohse, Julio T Barreiro, B Paredes, and Immanuel Bloch. Realization of the Hofstadter Hamiltonian with ultracold atoms in optical lattices. *Physical Review Letters*, 111(18):185301, 2013.
- [58] Hirokazu Miyake, Georgios A Siviloglou, Colin J Kennedy, William Cody Burton, and Wolfgang Ketterle. Realizing the Harper Hamiltonian with laser-assisted tunneling in optical lattices. *Physical Review Letters*, 111(18):185302, 2013.
- [59] Kurt M Fujiwara, Zachary A Geiger, Kevin Singh, Ruwan Senaratne, Shankari V Rajagopal, Mikhail Lipatov, Toshihiko Shimasaki, and David M Weld. Experimental realization of a relativistic harmonic oscillator. *New Journal of Physics*, 20(6):063027, jun 2018. doi: 10.1088/1367-2630/aacb5a.
- [60] C. J. Fujiwara, Kevin Singh, Zachary A. Geiger, Ruwan Senaratne, Shankari V. Rajagopal, Mikhail Lipatov, and David M. Weld. Transport in floquet-bloch bands. *Phys. Rev. Lett.*, 122:010402, Jan 2019. doi: 10.1103/PhysRevLett.122.010402. URL <https://link.aps.org/doi/10.1103/PhysRevLett.122.010402>.

- [61] W. S. Bakr, A. Peng, M. E. Tai, R. Ma, J. Simon, J. I. Gillen, S. Fölling, L. Pollet, and M. Greiner. Probing the superfluid-to-Mott insulator transition at the single-atom level. *Science*, 329:547–550, 2010.
- [62] W. S. Bakr, A. Peng, M. E. Tai, R. Ma, J. Simon, J. I. Gillen, S. Fölling, L. Pollet, and M. Greiner. Probing the superfluid-to-mott insulator transition at the single-atom level. *Science*, 329(5991):547–550, 2010. ISSN 0036-8075. doi: 10.1126/science.1192368. URL <https://science.sciencemag.org/content/329/5991/547>.
- [63] J. F. Sherson, C. Weitenberg, M. Endres, M. Cheneau, I. Bloch, and S. Kuhr. Single-atom-resolved fluorescence imaging of an atomic Mott insulator. *Nature*, 467:68–72, 2010.
- [64] Lawrence W Cheuk, Matthew A Nichols, Melih Okan, Thomas Gersdorf, Vinay V Ramasesh, Waseem S Bakr, Thomas Lompe, and Martin W Zwierlein. Quantum-gas microscope for fermionic atoms. *Physical Review Letters*, 114(19):193001, 2015.
- [65] Maxwell F Parsons, Florian Huber, Anton Mazurenko, Christie S Chiu, Widagdo Setiawan, Katherine Wooley-Brown, Sebastian Blatt, and Markus Greiner. Site-resolved imaging of fermionic Li 6 in an optical lattice. *Physical Review Letters*, 114(21):213002, 2015.
- [66] Ahmed Omran, Martin Boll, Timon A Hilker, Katharina Kleinlein, Guillaume Salomon, Immanuel Bloch, and Christian Gross. Microscopic observation of Pauli blocking in degenerate fermionic lattice gases. *Physical Review Letters*, 115(26):263001, 2015.
- [67] Elmar Haller, James Hudson, Andrew Kelly, Dylan A Cotta, Bruno Peaudecerf, Graham D Bruce, and Stefan Kuhr. Single-atom imaging of fermions in a quantum-gas microscope. *Nature Physics*, 11(9):738, 2015.
- [68] J. Billy, V. Josse, Z. Zuo, A. Bernard, B. Hambrecht, P. Lugan, D. Clément, L. Sanchez-Palencia, P. Bouyer, and A. Aspect. Direct observation of Anderson localization of matter waves in a controlled disorder. *Nature*, 453:891, 2008.
- [69] Bryce Gadway, Daniel Pertot, Jeremy Reeves, Matthias Vogt, and Dominik Schneble. Glassy behavior in a binary atomic mixture. *Physical Review Letters*, 107:145306, Sep 2011.
- [70] I. Bloch, J. Dalibard, and W. Zwerger. Many-body physics with ultracold gases. *Rev. Mod. Phys.*, 80:885–964, 2008.

- [71] Y. I. Manin. *Vychislomoe i Nevychislomoe (Computable and Noncomputable)*. Sovetskoye Radio, 1980.
- [72] Richard P Feynman. Simulating physics with computers. *International Journal of Theoretical Physics*, 21(6-7):467–488, 1982.
- [73] Maciej Lewenstein, Anna Sanpera, and Verònica Ahufinger. *Ultracold Atoms in Optical Lattices: Simulating quantum many-body systems*. Oxford University Press, 2012.
- [74] Fangzhao Alex An, Eric J. Meier, Jackson Ang’ong’a, and Bryce Gadway. Correlated dynamics in a synthetic lattice of momentum states. *Phys. Rev. Lett.*, 120:040407, Jan 2018. doi: 10.1103/PhysRevLett.120.040407. URL <https://link.aps.org/doi/10.1103/PhysRevLett.120.040407>.
- [75] Eric J. Meier, Fangzhao Alex An, Alexandre Dauphin, Maria Maffei, Pietro Massignan, Taylor L. Hughes, and Bryce Gadway. Observation of the topological anderson insulator in disordered atomic wires. *Science*, 362(6417):929–933, 2018. ISSN 0036-8075. doi: 10.1126/science.aat3406. URL <https://science.scienmag.org/content/362/6417/929>.
- [76] Markus Greiner, Cindy A Regal, and Deborah S Jin. Emergence of a molecular Bose-Einstein condensate from a Fermi gas. *Nature*, 426(6966):537, 2003.
- [77] Martin W Zwierlein, Claudiu A Stan, Christian H Schunck, Sebastian MF Raupach, Subhadeep Gupta, Zoran Hadzibabic, and Wolfgang Ketterle. Observation of Bose-Einstein condensation of molecules. *Physical Review Letters*, 91(25):250401, 2003.
- [78] K-K Ni, S Ospelkaus, D Wang, G Quéméner, B Neyenhuis, MHG De Miranda, JL Bohn, J Ye, and DS Jin. Dipolar collisions of polar molecules in the quantum regime. *Nature*, 464(7293):1324, 2010.
- [79] S Ospelkaus, K-K Ni, D Wang, MHG De Miranda, B Neyenhuis, G Quéméner, PS Julienne, JL Bohn, DS Jin, and J Ye. Quantum-state controlled chemical reactions of ultracold potassium-rubidium molecules. *Science*, 327(5967):853–857, 2010.
- [80] Bo Yan, Steven A Moses, Bryce Gadway, Jacob P Covey, Kaden RA Hazzard, Ana Maria Rey, Deborah S Jin, and Jun Ye. Observation of dipolar spin-exchange interactions with lattice-confined polar molecules. *Nature*, 501(7468):521, 2013.

- [81] Max Riedel, Matyas Kovacs, Peter Zoller, Jürgen Mlynek, and Tommaso Calarco. Europe’s quantum flagship initiative. *Quantum Science and Technology*, 4(2):020501, feb 2019. doi: 10.1088/2058-9565/ab042d.
- [82] Daniel Pertot, Bryce Gadway, and Dominik Schneble. Collinear four-wave mixing of two-component matter waves. *Physical Review Letters*, 104:200402, May 2010.
- [83] Bryce Gadway, Daniel Pertot, René Reimann, and Dominik Schneble. Superfluidity of interacting bosonic mixtures in optical lattices. *Physical Review Letters*, 105:045303, Jul 2010.
- [84] J B Reeves, B Gadway, T Bergeman, I Danshita, and D Schneble. Superfluid bloch dynamics in an incommensurate optical lattice. *New Journal of Physics*, 16(6):065011, jun 2014. doi: 10.1088/1367-2630/16/6/065011.
- [85] B. Gadway, D. Pertot, J. Reeves, and D. Schneble. Probing an ultracold-atom crystal with matter waves. *Nature Phys.*, advance online publication, May 2012. doi: 10.1038/nphys2320.
- [86] J. Reeves, L. Krinner, M. Stewart, A. Pazmiño, and D. Schneble. Nondiabatic diffraction of matter waves. *Physical Review A*, 92:023628, Aug 2015. doi: 10.1103/PhysRevA.92.023628.
- [87] Bryce Gadway, Jeremy Reeves, Ludwig Krinner, and Dominik Schneble. Evidence for a quantum-to-classical transition in a pair of coupled quantum rotors. *Physical Review Letters*, 110:190401, May 2013.
- [88] A. Recati, P. O. Fedichev, W. Zwerger, J. von Delft, and P. Zoller. Atomic quantum dots coupled to a reservoir of a superfluid bose-einstein condensate. *Phys. Rev. Lett.*, 94:040404, Feb 2005.
- [89] A. J. Leggett, S. Chakravarty, A. T. Dorsey, M. P. A. Fisher, A. Garg, and W. Zwerger. Dynamics of the dissipative two-state system. *Rev. Mod. Phys.*, 59:1–85, 1987.
- [90] P. P. Orth, I. Stanic, and K. Le Hur. Dissipative quantum Ising model in a cold-atom spin-boson mixture. *Phys. Rev. A*, 77:051601, 2008.
- [91] L. Krinner, M. Stewart, A. Pazmiño, J. Kwon, and D. Schneble. Spontaneous emission of matter waves from a tunable open quantum system. *Nature*, 559:589–592, Jul 2018. doi: 10.1038/s41586-018-0348-z. URL <https://www.nature.com/articles/s41586-018-0348-z>.

- [92] H.P. Breuer and F. Petruccione. *The Theory of Open Quantum Systems*. Oxford University Press, Great Clarendon Street, Oxford OX2 6DP, 2002.
- [93] Ulrich Weiss. *Quantum dissipative systems*, volume 13. World Scientific, 2012.
- [94] V. Weisskopf and E. Wigner. Berechnung der natürlichen linienbreite auf grund der diracschen lichttheorie. *Zeitschrift für Physik*, 63(1):54–73, 1930.
- [95] E. M. Purcell. Spontaneous emission probabilities at radio frequencies. *Physical Review*, 69:681, 1946.
- [96] Daniel Kleppner. Inhibited spontaneous emission. *Physical Review Letters*, 47:233–236, Jul 1981.
- [97] Vladimir P Bykov. Spontaneous emission from a medium with a band spectrum. *Soviet Journal of Quantum Electronics*, 4(7):861, 1975.
- [98] Sajeev John. Strong localization of photons in certain disordered dielectric superlattices. *Physical Review Letters*, 58:2486–2489, Jun 1987.
- [99] Eli Yablonovitch. Inhibited spontaneous emission in solid-state physics and electronics. *Phys. Rev. Lett.*, 58:2059–2062, May 1987. doi: 10.1103/PhysRevLett.58.2059.
- [100] Shawn-yu Lin, JG Fleming, DL Hetherington, BK Smith, R Biswas, KM Ho, MM Sigalas, W Zubrzycki, SR Kurtz, and Jim Bur. A three-dimensional photonic crystal operating at infrared wavelengths. *Nature*, 394(6690):251, 1998.
- [101] Michael D. Tocci, Michael Scalora, Mark J. Bloemer, Jonathan P. Dowling, and Charles M. Bowden. Measurement of spontaneous-emission enhancement near the one-dimensional photonic band edge of semiconductor heterostructures. *Physical Review A*, 53(4):2799–2803, 1996. PRA.
- [102] EP Petrov, VN Bogomolov, II Kalosha, and SV Gaponenko. Spontaneous emission of organic molecules embedded in a photonic crystal. *Physical Review Letters*, 81(1):77, 1998.
- [103] SG Romanov, AV Fokin, and RM De La Rue. Eu 3+ emission in an anisotropic photonic band gap environment. *Applied Physics Letters*, 76(13):1656–1658, 2000.

- [104] Shinpei Ogawa, Masahiro Imada, Susumu Yoshimoto, Makoto Okano, and Susumu Noda. Control of light emission by 3d photonic crystals. *Science*, 305(5681):227–229, 2004. doi: 10.1126/science.1097968.
- [105] Peter Lodahl, A. Floris van Driel, Ivan S. Nikolaev, Arie Irman, Karin Overgaag, Daniel Vanmaekelbergh, and Willem L. Vos. Controlling the dynamics of spontaneous emission from quantum dots by photonic crystals. *Nature*, 430(7000):654–657, 2004. 10.1038/nature02772.
- [106] S-P Yu, JD Hood, JA Muniz, MJ Martin, Richard Norte, C-L Hung, Seán M Meenehan, Justin D Cohen, Oskar Painter, and HJ Kimble. Nanowire photonic crystal waveguides for single-atom trapping and strong light-matter interactions. *Applied Physics Letters*, 104(11):111103, 2014.
- [107] A Goban, C-L Hung, S-P Yu, JD Hood, JA Muniz, JH Lee, MJ Martin, AC McClung, KS Choi, Darrick E Chang, et al. Atom-light interactions in photonic crystals. *Nature Communications*, 5:3808, 2014.
- [108] A. Goban, C. L. Hung, J. D Hood, S. P. Yu, J. A Muniz, O. Painter, and H. J Kimble. Superradiance for atoms trapped along a photonic crystal waveguide. *Physical Review Letters*, 115(6):063601, 2015.
- [109] Jonathan D. Hood, Akihisa Goban, Ana Asenjo-Garcia, Mingwu Lu, Su-Peng Yu, Darrick E. Chang, and H. J. Kimble. Atom–atom interactions around the band edge of a photonic crystal waveguide. *Proceedings of the National Academy of Sciences*, 113(38):10507–10512, 2016.
- [110] Yanbing Liu and Andrew A. Houck. Quantum electrodynamics near a photonic bandgap. *Nat Phys*, 13(1):48–52, 2017.
- [111] Neereja M. Sundaresan, Rex Lundgren, Guanyu Zhu, Alexey V. Gorshkov, and Andrew A. Houck. Interacting qubit-photon bound states with superconducting circuits. *Phys. Rev. X*, 9:011021, Feb 2019. doi: 10.1103/PhysRevX.9.011021. URL <https://link.aps.org/doi/10.1103/PhysRevX.9.011021>.
- [112] Inés de Vega, Diego Porras, and J. Ignacio Cirac. Matter-wave emission in optical lattices: Single particle and collective effects. *Physical Review Letters*, 101:260404, Dec 2008.
- [113] Carlos Navarrete-Benlloch, Inés de Vega, Diego Porras, and J Ignacio Cirac. Simulating quantum-optical phenomena with cold atoms in optical lattices. *New Journal of Physics*, 13(2):023024, 2011.

- [114] Michael Stewart, Ludwig Krinner, Arturo Pazmiño, and Dominik Schneble. Analysis of non-markovian coupling of a lattice-trapped atom to free space. *Physical Review A*, 95:013626, Jan 2017.
- [115] A. González-Tudela and J. I. Cirac. Quantum emitters in two-dimensional structured reservoirs in the nonperturbative regime. *Phys. Rev. Lett.*, 119:143602, Oct 2017. doi: 10.1103/PhysRevLett.119.143602.
- [116] A. González-Tudela and J. I. Cirac. Markovian and non-markovian dynamics of quantum emitters coupled to two-dimensional structured reservoirs. *Phys. Rev. A*, 96:043811, Oct 2017. doi: 10.1103/PhysRevA.96.043811. URL <https://link.aps.org/doi/10.1103/PhysRevA.96.043811>.
- [117] A. González-Tudela and J. I. Cirac. Exotic quantum dynamics and purely long-range coherent interactions in dirac conelike baths. *Phys. Rev. A*, 97:043831, Apr 2018. doi: 10.1103/PhysRevA.97.043831. URL <https://link.aps.org/doi/10.1103/PhysRevA.97.043831>.
- [118] A. González-Tudela and J. I. Cirac. Non-markovian quantum optics with three-dimensional state-dependent optical lattices. *Quantum*, 2:97, Oct 2018. ISSN 2521-327X. doi: 10.22331/q-2018-10-01-97.
- [119] A. González-Tudela and J. Ignacio Cirac. Quantum optics without photons. *Nature*, 559:481–482, 2018.
- [120] Daniel Pertot, Daniel Greif, Stephan Albert, Bryce Gadway, and Dominik Schneble. Versatile transporter apparatus for experiments with optically trapped bose-einstein condensates. *Journal of Physics B: Atomic, Molecular and Optical Physics*, 42(21):215305, 2009.
- [121] D. A. Steck. Rubidium 87 D line data. available online at <http://steck.us/alkalidata>. (revision 2.1.4, 23 December 2010).
- [122] Carlos Navarrete-Benlloch, Inés de Vega, Diego Porras, and J Ignacio Cirac. Simulating quantum-optical phenomena with cold atoms in optical lattices. *New Journal of Physics*, 13(2):023024, 2011.
- [123] Jun John Sakurai and Jim Napolitano. *Modern quantum mechanics*. Cambridge University Press, 2017.
- [124] Inés de Vega and Daniel Alonso. Dynamics of non-markovian open quantum systems. *Rev. Mod. Phys.*, 89:015001, Jan 2017. doi: 10.1103/

- RevModPhys.89.015001. URL <https://link.aps.org/doi/10.1103/RevModPhys.89.015001>.
- [125] D. Jaksch and P. Zoller. The cold atom hubbard toolbox. *Annals of Physics*, 315, 2005.
 - [126] J. Reichel, W. Hänsel, P. Hommelhoff, and T.W. Hänsch. Applications of integrated magnetic microtraps. *Applied Physics B*, 72:81–89, Jan 2001.
 - [127] Philipp Treutlein, David Hunger, Stephan Camerer, Theodor W. Hänsch, and Jakob Reichel. Bose-einstein condensate coupled to a nanomechanical resonator on an atom chip. *Phys. Rev. Lett.*, 99: 140403, Oct 2007. doi: 10.1103/PhysRevLett.99.140403. URL <https://link.aps.org/doi/10.1103/PhysRevLett.99.140403>.
 - [128] David Hunger, Stephan Camerer, Theodor W. Hänsch, Daniel König, Jörg P. Kotthaus, Jakob Reichel, and Philipp Treutlein. Resonant coupling of a bose-einstein condensate to a micromechanical oscillator. *Phys. Rev. Lett.*, 104:143002, Apr 2010. doi: 10.1103/PhysRevLett.104.143002. URL <https://link.aps.org/doi/10.1103/PhysRevLett.104.143002>.
 - [129] P. W. Anderson. Localized magnetic states in metals. *Phys. Rev.*, 124: 41–53, Oct 1961. doi: 10.1103/PhysRev.124.41. URL <https://link.aps.org/doi/10.1103/PhysRev.124.41>.
 - [130] Gerd Schön and A.D. Zaikin. Quantum coherent effects, phase transitions, and the dissipative dynamics of ultra small tunnel junctions. *Physics Reports*, 198(5):237 – 412, 1990. ISSN 0370-1573. doi: [https://doi.org/10.1016/0370-1573\(90\)90156-V](https://doi.org/10.1016/0370-1573(90)90156-V). URL <http://www.sciencedirect.com/science/article/pii/037015739090156V>.
 - [131] N V Prokofev and P C E Stamp. Giant spins and topological decoherence: a hamiltonian approach. *Journal of Physics: Condensed Matter*, 5(50):L663–L670, dec 1993. doi: 10.1088/0953-8984/5/50/002.
 - [132] N V Prokofev and P C E Stamp. Theory of the spin bath. *Reports on Progress in Physics*, 63(4):669–726, mar 2000. doi: 10.1088/0034-4885/63/4/204.
 - [133] Filippo Caruso, Vittorio Giovannetti, Cosmo Lupo, and Stefano Mancini. Quantum channels and memory effects. *Rev. Mod. Phys.*,

- 86:1203–1259, Dec 2014. doi: 10.1103/RevModPhys.86.1203. URL <https://link.aps.org/doi/10.1103/RevModPhys.86.1203>.
- [134] M B Plenio and S F Huelga. Dephasing-assisted transport: quantum networks and biomolecules. *New Journal of Physics*, 10(11):113019, nov 2008. doi: 10.1088/1367-2630/10/11/113019.
 - [135] F. Caruso, A. W. Chin, A. Datta, S. F. Huelga, and M. B. Plenio. Highly efficient energy excitation transfer in light-harvesting complexes: The fundamental role of noise-assisted transport. *The Journal of Chemical Physics*, 131(10):105106, 2009. doi: 10.1063/1.3223548. URL <https://aip.scitation.org/doi/abs/10.1063/1.3223548>.
 - [136] Patrick Rebentrost, Masoud Mohseni, Ivan Kassal, Seth Lloyd, and Alán Aspuru-Guzik. Environment-assisted quantum transport. *New Journal of Physics*, 11(3):033003, mar 2009. doi: 10.1088/1367-2630/11/3/033003.
 - [137] M. Mohseni, A. Shabani, S. Lloyd, Y. Omar, and H. Rabitz. Geometrical effects on energy transfer in disordered open quantum systems. *The Journal of Chemical Physics*, 138(20):204309, 2013. doi: 10.1063/1.4807084. URL <https://doi.org/10.1063/1.4807084>.
 - [138] N. Lambert, Y.H. Chen, Y.C. Cheng, C.M. Li, G.Y. Chen, and F. Nori. Quantum biology. *Nat. Phys.*, 9:10–18, Dec 2012. doi: 10.1038/nphys2474. URL <https://www.nature.com/articles/nphys2474>.
 - [139] A.O. Caldeira and A.J. Leggett. Path integral approach to quantum brownian motion. *Physica A (Amsterdam)*, 121:586–616, Sep 1983.
 - [140] Inés de Vega and Daniel Alonso. Dynamics of non-markovian open quantum systems. *Reviews of Modern Physics*, 89:015001, Jan 2017.
 - [141] Pierre Meystre and Murray Sargent III. *Elements of Quantum Optics*. Springer Verlag Berlin Heidelberg, 2007.
 - [142] P. W. Milonni. *The Quantum Vacuum: An Introduction to Quantum Electrodynamics*. Academic Press, Inc., 1994.
 - [143] M.O. Scully and M.S. Zubairy. *Quantum Optics*. Cambridge University Press, University Printing House, CB2 8BS, United Kingdom, 1997.
 - [144] Y. Yamamoto and A. Imamoglu. *Mesoscopic Quantum Optics*. John Wiley & Sons, Inc., New York, 1999.

- [145] P. Blanchard and E. Brüning. *Mathematical Methods in Physics: Distributions, Hilbert Space Operators, and Variational Methods*. Birkhäuser, Boston, MA, 2003.
- [146] H. Metcalf and P. van der Straten. *Atoms and Molecules Interacting with Light*. Cambridge University Press, University Printing House, CB2 8BS, United Kingdom, 2016.
- [147] Willis E. Lamb and Robert C. Rutherford. Fine structure of the hydrogen atom by a microwave method. *Phys. Rev.*, 72:241–243, Aug 1947. doi: 10.1103/PhysRev.72.241. URL <https://link.aps.org/doi/10.1103/PhysRev.72.241>.
- [148] H. A. Bethe. The electromagnetic shift of energy levels. *Phys. Rev.*, 72: 339–341, Aug 1947. doi: 10.1103/PhysRev.72.339. URL <https://link.aps.org/doi/10.1103/PhysRev.72.339>.
- [149] M. Stewart, J. Kwon, A. Lanuza, and D. Schnable. Fractional decay of matter-wave quantum emitters in a synthetic bandgap material. *arXiv*, pages 2003.02816 [cond-mat.quant-gas], 2020.
- [150] Herbert Walther, Benjamin TH Varcoe, Berthold-Georg Englert, and Thomas Becker. Cavity quantum electrodynamics. *Reports on Progress in Physics*, 69(5):1325, 2006.
- [151] Serge Haroche and Jean-Michel Raimond. *Exploring the quantum: atoms, cavities, and photons*. Oxford University Press, 2006.
- [152] Maciej Lewenstein, Jakub Zakrzewski, and Thomas W. Mossberg. Spontaneous emission of atoms coupled to frequency-dependent reservoirs. *Phys. Rev. A*, 38:808–819, Jul 1988. doi: 10.1103/PhysRevA.38.808.
- [153] A.G. Kofman, G. Kurizki, and B. Sherman. Spontaneous and induced atomic decay in photonic band structures. *Journal of Modern Optics*, 41(2):353–384, 1994. doi: 10.1080/09500349414550381.
- [154] Søren Bay, P. Lambropoulos, and Klaus Mølmer. Atom-atom interaction in strongly modified reservoirs. *Phys. Rev. A*, 55:1485–1496, Feb 1997. doi: 10.1103/PhysRevA.55.1485.
- [155] P.R. Berman and G.W. Ford. Spontaneous decay, unitarity, and the weisskopf-wigner approximation. In E. Arimondo, P.R. Berman, and C.C. Lin, editors, *Advances in Atomic, Molecular, and Optical Physics*, volume 59, pages 176–233. Elsevier, Amsterdam, 2010.

- [156] Ivan H. Deutsch and Poul S. Jessen. Quantum-state control in optical lattices. *Phys. Rev. A*, 57:1972–1986, Mar 1998. doi: 10.1103/PhysRevA.57.1972. URL <http://link.aps.org/doi/10.1103/PhysRevA.57.1972>.
- [157] D. Jaksch, H.-J. Briegel, J. I. Cirac, C. W. Gardiner, and P. Zoller. Entanglement of atoms via cold controlled collisions. *Phys. Rev. Lett.*, 82:1975–1978, Mar 1999. doi: 10.1103/PhysRevLett.82.1975. URL <http://link.aps.org/doi/10.1103/PhysRevLett.82.1975>.
- [158] P Lambropoulos, Georgios M Nikolopoulos, Torben R Nielsen, and Søren Bay. Fundamental quantum optics in structured reservoirs. *Reports on Progress in Physics*, 63(4):455, 2000.
- [159] Sajeev John. Electromagnetic absorption in a disordered medium near a photon mobility edge. *Phys. Rev. Lett.*, 53:2169–2172, Nov 1984. doi: 10.1103/PhysRevLett.53.2169.
- [160] Sajeev John and Jian Wang. Quantum electrodynamics near a photonic band gap: Photon bound states and dressed atoms. *Physical Review Letters*, 64:2418–2421, May 1990.
- [161] Sajeev John and Jian Wang. Quantum optics of localized light in a photonic band gap. *Phys. Rev. B*, 43:12772–12789, Jun 1991.
- [162] P. Coleman. *Introduction to Many-Body Physics*. Cambridge University Press, 2015. ISBN 9780521864886. URL <https://books.google.com/books?id=PDg1HQAACAAJ>.
- [163] F. Lombardo, F. Ciccarello, and G. M. Palma. Photon localization versus population trapping in a coupled-cavity array. *Phys. Rev. A*, 89:053826, May 2014. doi: 10.1103/PhysRevA.89.053826. URL <https://link.aps.org/doi/10.1103/PhysRevA.89.053826>.
- [164] Giuseppe Calajó, Francesco Ciccarello, Darrick Chang, and Peter Rabl. Atom-field dressed states in slow-light waveguide qed. *Phys. Rev. A*, 93:033833, Mar 2016. doi: 10.1103/PhysRevA.93.033833.
- [165] S. G. Albert. Cooling, trapping, and transport of atom clouds in a new BEC apparatus. Master’s thesis, Stony Brook University, 2007.
- [166] D. E. Sproles. Laser spectroscopy and magneto-optical trapping of rubidium atoms. Master’s thesis, Stony Brook University, 2008.

- [167] D. G. Greif. Evaporative cooling and Bose–Einstein condensation of Rb-87 in a moving-coil TOP trap geometry. Master’s thesis, Stony Brook University, 2007.
- [168] R. H. Reimann. Quantum gases in state-dependent optical potentials. Master’s thesis, Stony Brook University, 2009.
- [169] D. A. Pertot. *Two-Component Bosons in State-Dependent Optical Lattices*. PhD thesis, Stony Brook University, 2011.
- [170] B. R. Gadway. *Bose Gases in Tailored Optical and Atomic Lattices*. PhD thesis, Stony Brook University, 2012.
- [171] J. B. Reeves. *Dynamics of Atomic Matter Waves in Optical Lattices*. PhD thesis, Stony Brook University, 2015.
- [172] L. Krinner. *Exploring Spontaneous Emission Phenomena using Ultracold Atomic Matter Waves*. PhD thesis, Stony Brook University, 2018.
- [173] H. J. Metcalf and P. van der Straten. *Laser Cooling and Trapping*. Springer-Verlag, New York, 1999.
- [174] W. Petrich, M. H. Anderson, J. R. Ensher, and E. A. Cornell. Stable, tightly confining magnetic trap for evaporative cooling of neutral atoms. *Phys. Rev. Lett.*, 74:3352–3355, 1995.
- [175] Ludwig Krinner, Michael Stewart, Arturo Pazmiño, and Dominik Schneble. In-situ magnetometry for experiments with atomic quantum gases. *Review of Scientific Instruments*, 89:013108, 2018.
- [176] M. Greiner, I. Bloch, O. Mandel, T. W. Hänsch, and T. Esslinger. Exploring phase coherence in a 2D lattice of Bose–Einstein condensates. *Phys. Rev. Lett.*, 87:160405, 2001.
- [177] W. Ketterle, D. S. Durfee, and D. M. Stamper-Kurn. Making, probing, and understanding bose-einstein condensates. *arXiv*, pages 9904034v2 [cond-mat], 1999.
- [178] R. Grimm, M. Weidemüller, and Y. B. Ovchinnikov. Optical dipole traps for neutral atoms. *Adv. At. Mol. Opt. Phys.*, 42:95, 2000.
- [179] G. Breit and I. I. Rabi. Measurement of nuclear spin. *Phys. Rev.*, 38: 2082–2083, 1931.

- [180] P. L. Kapitza and P. A. M. Dirac. The reflection of electrons from standing light waves. *Proc. Cambridge Phil. Soc.*, 29:297, 1933.
- [181] W. R. Klein and B. D. Cook. Unified approach to ultrasonic light diffraction. *IEEE Trans. Sonics and Ultrasonics*, 14:123, 1967.
- [182] P. L. Gould, G. A. Ruff, and D. E. Pritchard. Diffraction of atoms by light: The near-resonant Kapitza-Dirac effect. *Phys. Rev. Lett.*, 56: 827–830, 1986.
- [183] H. Batelaan. *Colloquium*: Illuminating the Kapitza-Dirac effect with electron matter optics. *Rev. Mod. Phys.*, 79:929–941, 2007.
- [184] Bryce Gadway, Daniel Pertot, René Reimann, Martin G Cohen, and Dominik Schneble. Analysis of kapitza-dirac diffraction patterns beyond the raman-nath regime. *Optics express*, 17(21):19173–19180, 2009.
- [185] Qiong Liu, Hongwei Song, Wei Wang, Xue Bai, Yu Wang, Biao Dong, Lin Xu, and Wei Han. Observation of lamb shift and modified spontaneous emission dynamics in the ybo 3: Eu 3+ inverse opal. *Optics letters*, 35 (17):2898–2900, 2010.
- [186] Ulrich Hoepppe, Christian Wolff, Jens Küchenmeister, Jens Niegemann, Malte Drescher, Hartmut Benner, and Kurt Busch. Direct observation of non-markovian radiation dynamics in 3d bulk photonic crystals. *Physical Review Letters*, 108(4):043603, 2012. PRL.
- [187] Asher Peres. Zeno paradox in quantum theory. *American Journal of Physics*, 48(11):931–932, 1980. doi: doi:<http://dx.doi.org/10.1119/1.12204>. URL <http://scitation.aip.org/content/aapt/journal/ajp/48/11/10.1119/1.12204>.
- [188] Wayne Itano, D. Heinzen, J. Bollinger, and D. Wineland. Quantum zeno effect. *Physical Review A*, 41(5):2295–2300, 1990. doi: 10.1103/PhysRevA.41.2295.
- [189] D. van Oosten, P. van der Straten, and H. T. C. Stoof. Quantum phases in an optical lattice. *Phys. Rev. A*, 63:053601, 2001.
- [190] M. Lewenstein, A. Sanpera, V. Ahufinger, B. Damski, Sen(De) A., and U. Sen. Ultracold atomic gases in optical lattices: mimicking condensed matter physics and beyond. *Adv. Phys.*, 56:243–379, 2007.
- [191] C. J. Pethick and H. Smith. *Bose-Einstein Condensation in Dilute Gases*. Cambridge University Press, New York, 2008.

- [192] M. P. A. Fisher, P. B. Weichman, G. Grinstein, and D. S. Fisher. Boson localization and the superfluid-insulator transition. *Phys. Rev. B*, 40: 546–570, 1989.
- [193] D. Jaksch, C. Bruder, J. I. Cirac, C. W. Gardiner, and P. Zoller. Cold bosonic atoms in optical lattices. *Phys. Rev. Lett.*, 81:3108–3111, 1998.
- [194] W. Zwerger. Mott–Hubbard transition of cold atoms in optical lattices. *J. Opt. B: Quantum Semiclass. Opt.*, 5:S9–S16, 2003.
- [195] W. Krauth, M. Caffarel, and J.-P. Bouchaud. Gutzwiller wave function for a model of strongly interacting bosons. *Phys. Rev. B*, 45:3137–3140, 1992.
- [196] K. Sheshadri, H. R. Krishnamurthy, R. Pandit, and T. V. Ramakrishnan. Superfluid and insulating phases in an interacting-boson model: Mean-field theory and the RPA. *Europhys. Lett.*, 22:257, 1993.
- [197] C. Orzel, A. K. Tuchman, M. L. Fenselau, M. Yasuda, and M. A. Kasevich. Squeezed states in a Bose–Einstein condensate. *Science*, 291:2386, 2001.
- [198] S. Fölling, A. Widera, T. Müller, F. Gerbier, and I. Bloch. Formation of spatial shell structure in the superfluid to Mott insulator transition. *Phys. Rev. Lett.*, 97:060403, 2006.
- [199] G. K. Campbell, J. Mun, M. Boyd, P. Medley, A. E. Leanhardt, L. G. Marcassa, D. E. Pritchard, and W. Ketterle. Imaging the Mott insulator shells by using atomic clock shifts. *Science*, 313(5787):649–652, 2005.
- [200] N. Gemelke, X. Zhang, C.-L. Hung, and C. Chin. *In-situ* observation of incompressible Mott-insulating domains in ultracold atomic gases. *Nature*, 460:995–998, 2009.
- [201] M. Ferrareto and L. Salasnich. Effects of long-range hopping in the bose-hubbard model. *Phys. Rev. A*, 99:013618, Jan 2019. doi: 10.1103/PhysRevA.99.013618. URL <https://link.aps.org/doi/10.1103/PhysRevA.99.013618>.
- [202] L. Fallani, C. Fort, J.E. Lye, and M. Inguscio. Bose-einstein condensate in an optical lattice with tunable spacing: transport and static properties. *Opt. Express*, 13(11):4303–4313, May 2005. doi: 10.1364/OPEX.13.004303. URL <http://www.opticsexpress.org/abstract.cfm?URI=oe-13-11-4303>.

- [203] T.C. Li, D. Medellin, and M.G. Raizen. Real-time control of the periodicity of a standing wave: an optical accordion. *Optics Express*, 16:5465, Apr 2008.
- [204] R. H. Dicke. Coherence in spontaneous radiation processes. *Physical Review*, 93(1):99–110, 1954.